DOE/ER/40147--11

DE93 007302

NUCLEAR INTERACTIONS OF HIGH ENERGY HEAVY IONS AND APPLICATIONS IN ASTROPHYSICS

Technical Progress Report

1 April 1992 - 31 March 1993

John P. Wefel and T. Gregory Guzik
Department of Physics and Astronomy
Louisiana State University
Baton Rouge, LA 70803-4001

11 January 1993

MASTER

DISTRIBUTION OF THIS DOCUMENT IS UNLIMITED

Prepared for the U. S. Department of Energy under
Grant Number DE-FG05-84ER40147

TABLE OF CONTENTS

DISCLAIMER

TECHNICAL PROGRESS REPORT

Grant DE-FG05-84ER40147

John P. Wefel, Principal Investigator
T. Gregory Guzik, Co-Investigator

I. SUMMARY

This past year has focused mainly on the analysis of data taken during previous years and significant progress has been made. Much of the analysis and checking has been completed for the low energy ^{16}O and ^{28}Si dataset and we are in the final stages of preparing these results for publication. In addition, the charge-changing cross sections from our HISS experiment, E938H, have been finalized and we are beginning a "production" mode of analysis for the mass-changing, isotopic cross sections.

Finalizing the HISS charging changing cross sections has required that we complete a detailed calibration of essentially all detectors upstream of the HISS dipole magnet, including the trajectory detectors and the upstream charge sensing detectors. Next the beam vector was used to project the beam profile onto the target to determine the effective LH_2 interaction thickness for each beam and onto detectors downstream of the target to evaluate the apperatus acceptance as a function of change and mass. In parallel to this effort, work continued on determining the mass changing, isotopic cross sections from ^{32}S at 400, 600 and 800 MeV/nucleon. This has involved detailed calibrations of the drift chamber particle trajectory detector and the time-of-flight (TOF) particle velocity detector, both located downstream of the HISS magnet, as well as studies involving data selection criteria, beam normalization and apperatus acceptance. Currently, isotopic cross sections are available for the 400 MeV/nucleon ^{32}S and a study of the sulfur excitation function involving all three beams is expected to be submitted for publication during Spring 93.

The analysis of these HISS data over the past year has enabled us to identify and solve critical problems in obtaining final results. These lessons can now be applied to the remaining datasets and, in particular, we have developed a set of production programs that will automate the process of converting the raw dataset to "physics" units. Over the next year we will process the complete E938H data volume so that cross sections can be obtained without a detailed knowledge of the detector calibration and should significantly increase the efficiency of the analysis.

The low energy ^{28}Si analysis has been completed, including background corrections for Al, and isotopic cross sections are now available for fragments from C to Al. This effort is currently in the stage of preparing the results for final publication. Work also continues on the low energy ^{16}O dataset and, following the ^{28}Si paper, we will complete the preparation of these results.

During the past year the following paper was submitted, reviewed and accepted for publication:

> "A Program to Measure New Energetic Particle Nuclear Interaction Cross Sections", T. G. Guzik, S. Albergo, C-X. Chen, S. Costa, H. J. Crawford, J. Engelage, P. Ferrando, I. Flores, L. Greiner, F. C. Jones, C. N. Knott, S. Ko, P. J. Lindstrom, J. Mazotta, J. W. Mitchell, J. Ramanski, R. Poterya, A. Soutoul, O. Testard, C. E. Tull, C. Tuve, C. J. Waddington, W. R. Webber, J. P. Wefel and X. Zhang, Advances in Space Research, in press, (1993).

and there are several papers currently in the process of being prepared for publication.

"Low Energy (E=245 MeV/nucleon) Fragmentation Cross Sections of ^{28}Si and their use in Astrophysical Calculations" H. J. Crawford, T. G. Guzik, M. Hof., M. Hollier, J. Isbert, P. J. Lindstrom, K. D. Mathis, J. W. Mitchell, J. Neuhaus, W. Schimmerling, M. Simon, J. P. Wefel, and D. Williams, in preparation, (1993).

"Production Cross Sections of Fragments from Relativistic Neon to Nickel Projectiles Part 1: Change Changing Cross Sections", C.-X. Chen, S. Albergo, T. G. Guzik, S. Costa, H. J. Crawford, J. Engelage, P. Ferrando, I. Flores, L. Greiner, F. C. Jones, C. N. Knott, S. Ko, P. J. Lindstrom, J. Mazotta, J. W. Mitchell, J. Romanski, R. Potenza, A. Soutoul, O. Testard, C. E. Tull, C. Tuve, C. J. Waddington, W. R. Webber, J. P. Wefel, X. Zhang, in preparation, (1993).

"Production Cross Sections of Fragments from Relativistic Neon to Nickel Projectiles Part 2: The Heavy Ion Spectrometer System Experimental Apparatus", J. Engelage, S. Albergo, C.-X. Chen, S. Costa, H. J. Crawford, P. Ferrando, I. Flores, L. Greiner, T. G. Guzik, F. C. Jones, C. N. Knott, S. Ko, P. J. Lindstrom, J. Mazotta, J. W. Mitchell, J. Romanski, R. Potenza, A. Soutoul, O. Testard, C. E. Tull, C. Tuve, C. J. Waddington, W. R. Webber, J. P. Wefel, X. Zhang, in preparation, (1993).

"Production Cross Section of Fragments from Relativistic Neon to Nickel Projectiles Part 3: Isotopic Cross Sections for a ^{32}S beam and their Excitation Functions", C. E. Tull, S. Albergo, C.-X. Chen, S. Costa, H. J. Crawford, J. Engelage, P. Ferrando, I. Flores, L. Greiner, T. G. Guzik, F. C. Jones, C. N. Knott, S. Ko, P. J. Lindstrom, J. Mazotta, J. W. Mitchell, J. Romanski, R. Potenza, A. Soutoul, O. Testard, C. Tuve, C. J. Waddington, W. R. Webber, J. P. Wefel, X. Zhang, in preparation, (1993).

Work on the ^{28}Si data has also contributed to the recent Ph.D. award to Joachim Isbert and the publication of his thesis:

"Experimentelle Bestimmung der Wirkungsquerschmitte von Silizium an Wasserstoff bei einer Energie von 245 MeV/nukleon", University of Seigen, Seigen, Germany, Nov. 1991.

Finally we presented several talks at various meetings this past year,

"Elemental Production Cross Sections from Neon to Nickel: The Transport Collaboration," C. N. Knott et al., Spring, 92 APS.

"Charge Changing Total Cross Sections of Heavy Ions on Liquid Hydrogen Target," C.-X. Chen et al., Spring, 92, APS.

"Isotopic Production Cross Sections from Projectile Fragmentation of ^{32}S in a Liquid Hydrogen Target," C. E. Tull et al., Spring 92, APS.

"A Program to Measure New Energtetic Particle Nuclear Interaction Cross Sections," T. Gregory Guzik et al., August 92, COSPAR.

and expect to present further results at the Spring, 93 APS and July, 93 ICRC meetings.

II. PROJECT OVERVIEW

The interaction of energetic complex nuclei with matter is a fundamental area of investigation[15-19] whose results are important to diverse fields, yet the underlying nuclear processes involved are only moderately well understood. The overall scientific objective of this project is to investigate the mechanisms and the energy dependence of heavy ion fragmentation by studying the interactions of accelerated heavy ion projectiles (e.g. ^{4}He, ^{16}O, ^{20}Ne, ^{28}Si, ^{56}Fe) in a variety of targets (H, He, C, Si, Cu, Pb) and at a number of beam energies, both in the intermediate energy region (~0.1 - 0.8 GeV/nucleon) where there has been little previous work[1] and at higher energies. The overall dataset will connect results in the high energy (>1 GeV/nucleon)[20-23] and low energy (≤100 MeV/nucleon) regimes and permit an investigation of the energy dependence of the fragmentation process.

Our results also have a direct application to outstanding questions in high energy Nuclear Astrophysics. In traveling through the galaxy, the high energy cosmic ray nuclei (encompassing all of the elements from H-U) interact with the interstellar medium forming fragmentation products. These secondary nuclei contain information on the confinement and propagation process as well as distorting the observed isotopic composition. Obtaining information on the "sources", and the processes of nucleosynthesis undergone by cosmic ray matter, requires unfolding the fragmentation effects from the measured distributions. The key ingredient in making progress here is accurately measured cross sections at a variety of energies.

A. NUCLEAR PHYSICS

1. Limiting Fragmentation

Theory predicts that at some energy the cross sections become independent of energy, i.e. the region of Limiting Fragmentation. For light beams such as ^{16}O or ^{12}C limiting fragmentation has been suggested to begin at various energies, from several GeV/nucleon to as low as 100 MeV/nucleon.[25] The location of limiting fragmentation is important since it determines the "dividing line" between fragmentation modes characterized by collective effects[3] and fragmentation dominated by single nucleon interactions.[4]

Figure 1 shows the status of the measurement of the nuclear excitation function for $^{16}\mathrm{O} + p \rightarrow {}^{12,13}\mathrm{C}$ and ^{14,15}N. The curves show model predictions based upon the semi-empirical equatons[26] (solid line) and the systematic fits[27] (dashed line). Note that the available data are consistent with little or no energy dependence above ~0.2 GeV/nucleon (with the possible exception of ^{15}N) while the predictions show an energy dependence up to high energy. The systematic fits [27]are based upon the idea of limiting fragmentation, but the level of the dashed lines is not in the best agreement with the data. Our lowest energy points (160 MeV/nucleon) are consistently above the higher energy data and are consistent with a rising cross section at low energy such as is observed for $^{16}\mathrm{O} + p \rightarrow {}^{15}\mathrm{O}$ shown in Figure 2.

Our results for total charge changing cross sections are shown in Figure 3. The B40 work with ^{28}Si at a variety of energies interacting in different targets is shown on the left while preliminary data from the HISS runs, all with the liquid hydrogen target, for ^{22}Ne, ^{26}Mg, ^{32}S and ^{40}Ca beams are shown at the right. The dashed curve shows the result of an empirical formula for

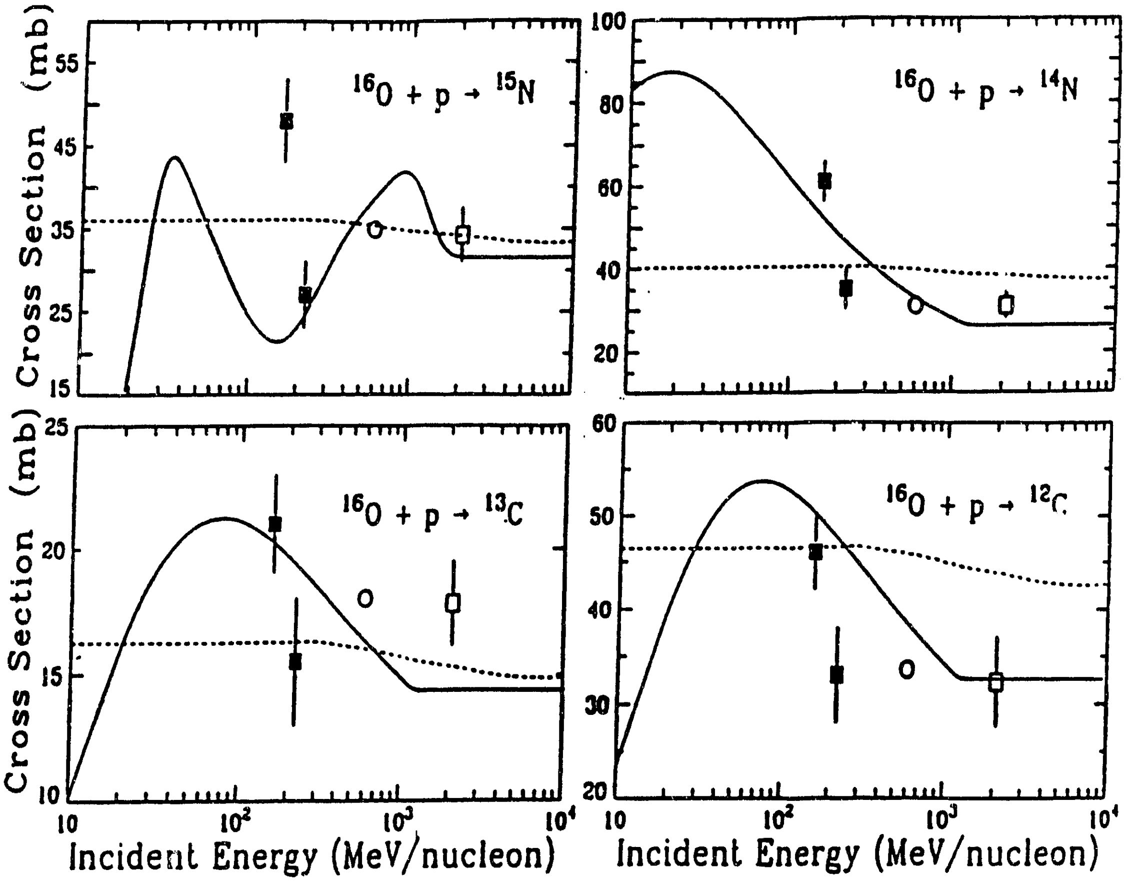

Figure 1. Comparison of ^{16}O data at 160 and 225 MeV/nucleon for $^{14,15}N$ and $^{12,13}C$ with other measurements and with model predictions.

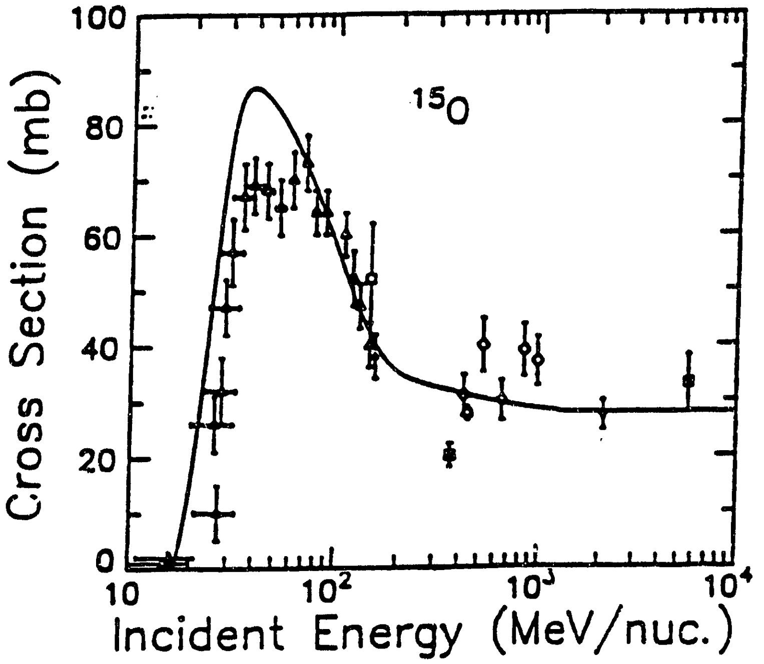

Figure 2. The $^{16}O + p \rightarrow {}^{15}O$ excitation function.

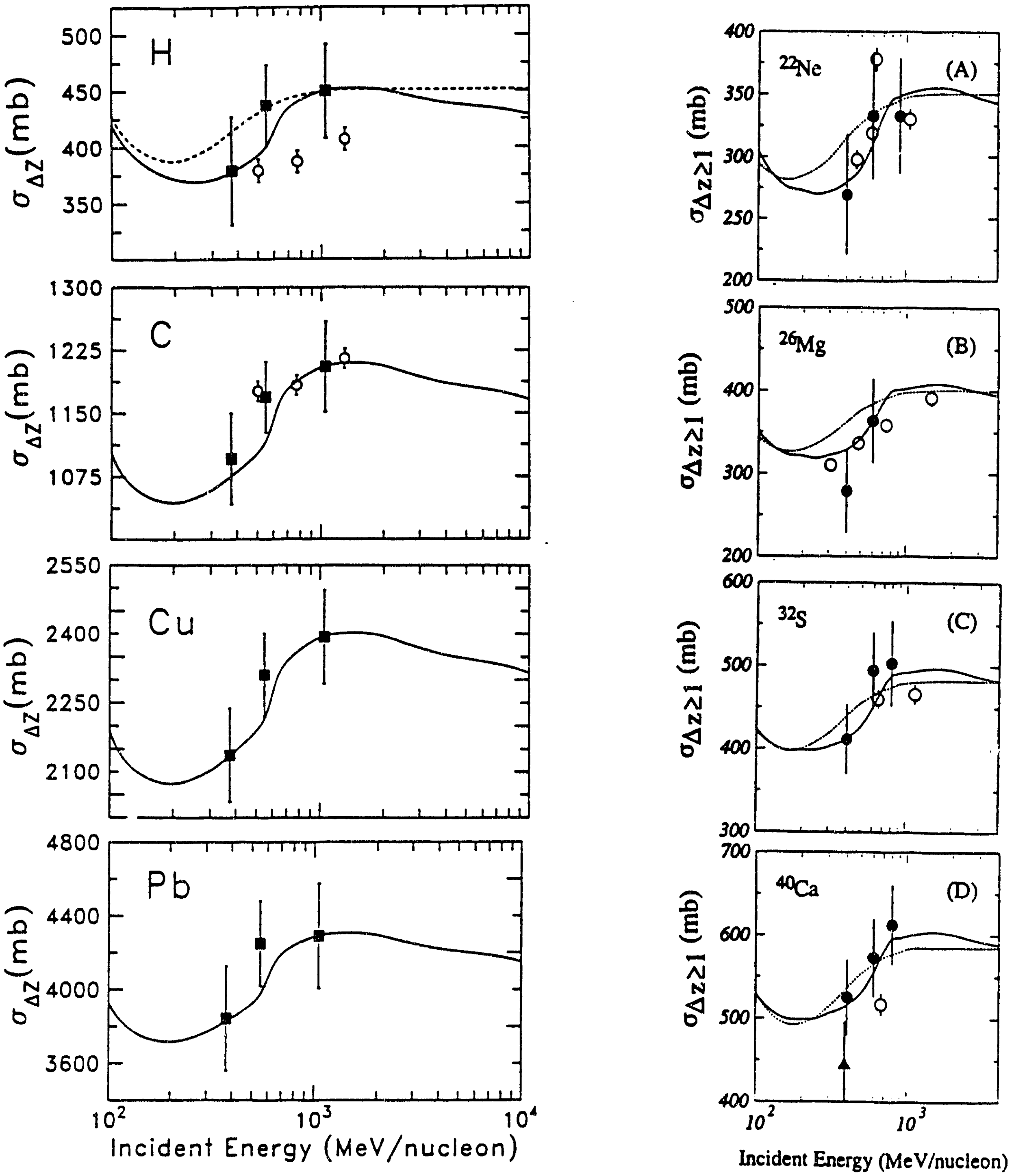

Figure 3. Total charge changing cross sections for ^{28}Si in a variety of targets (left) and for a variety of beams in the liquid hydrogen target (right).

predicting proton total reaction cross sections,[28] while the solid curve shows the result of using the Karol[29] scaling formula to predict total reaction cross sections based upon measured values[30,31] and utilizing the known energy dependence of (p,p) and (p,n) total cross sections. This latter formula reproduces our compilation of proton total reaction cross sections,[11] as shown at the top of Figure 4. In all of the data, the energy dependence does not obtain a "limiting value" until beyond a few GeV/nucleon.

A similar result seems to hold for nucleus-nucleus cross sections shown on the left of Figure 3. This is consistent with the anticipated energy dependence for $^{12}C + {}^{12}C$ total reaction cross sections for which compiled data[32-34] is shown at the bottom of Figure 4. However, there are no $^{12}C + {}^{12}C$ measurements in the intermediate energy region to verify the predicted curve.

The data in Figures 1-4, however, show that the experimental situation is not as simple as the limiting fragmentation picture predicts. For higher energies, using the new beams at CERN and BNL, the cross sections on hydrogen have been reported to vary from their values at 2 GeV/nucleon.[35] Thus, even beyond several GeV/nucleon it may not be possible to invoke limiting fragmentation to predict the cross sections and the physics.

2. Factorization

Early work at 1-2 GeV/nucleon[20] has shown that the partial cross sections are factorizable into two functions, one depending upon the projectile and the fragment and the other depending upon the target (T).

$$\sigma(P,F,T) = \gamma_P^F \gamma_T \tag{1}$$

This condition, originally derived from multi-particle reaction studies,[36] is called "strong factorization"[37] and should hold in the region of limiting fragmentation. A less restrictive condition, known as "weak factorization" is expressed as:

$$\sigma(P,F,T) = \gamma_P^F \gamma_T^P \tag{2}$$

where the target factor is a weak function of the projectile as well.[37]

Investigation of the deviations of data from these two conditions shows that while strong factorization does, indeed, appear to be violated, it is not violated to the extent predicted by the theory.[21] In addition, there is no systematic deviation from weak factorization (except in the case of hydrogen targets). These results serve to constrain the various fragmentation models in two ways: 1) the extent to which the data conforms to strong factorization suggest that fragmentation occurs at relatively large impact parameters and 2) the lack of deviation from weak factorization is inconsistent with the abrasion phase of the abrasion-ablation model[38-39] and lends support to the excitation-decay picture.[9]

However, hydrogen targets do not fit this picture and detailed analyses have only been performed at high energy (1-2 GeV/nucleon). A more complete test requires evaluation at lower energies as proposed here. The study of factorization at low energy can also be important in establishing the region of transition from fragmentation to deep inelastic behavior and to understanding the hydrogen target anomaly.

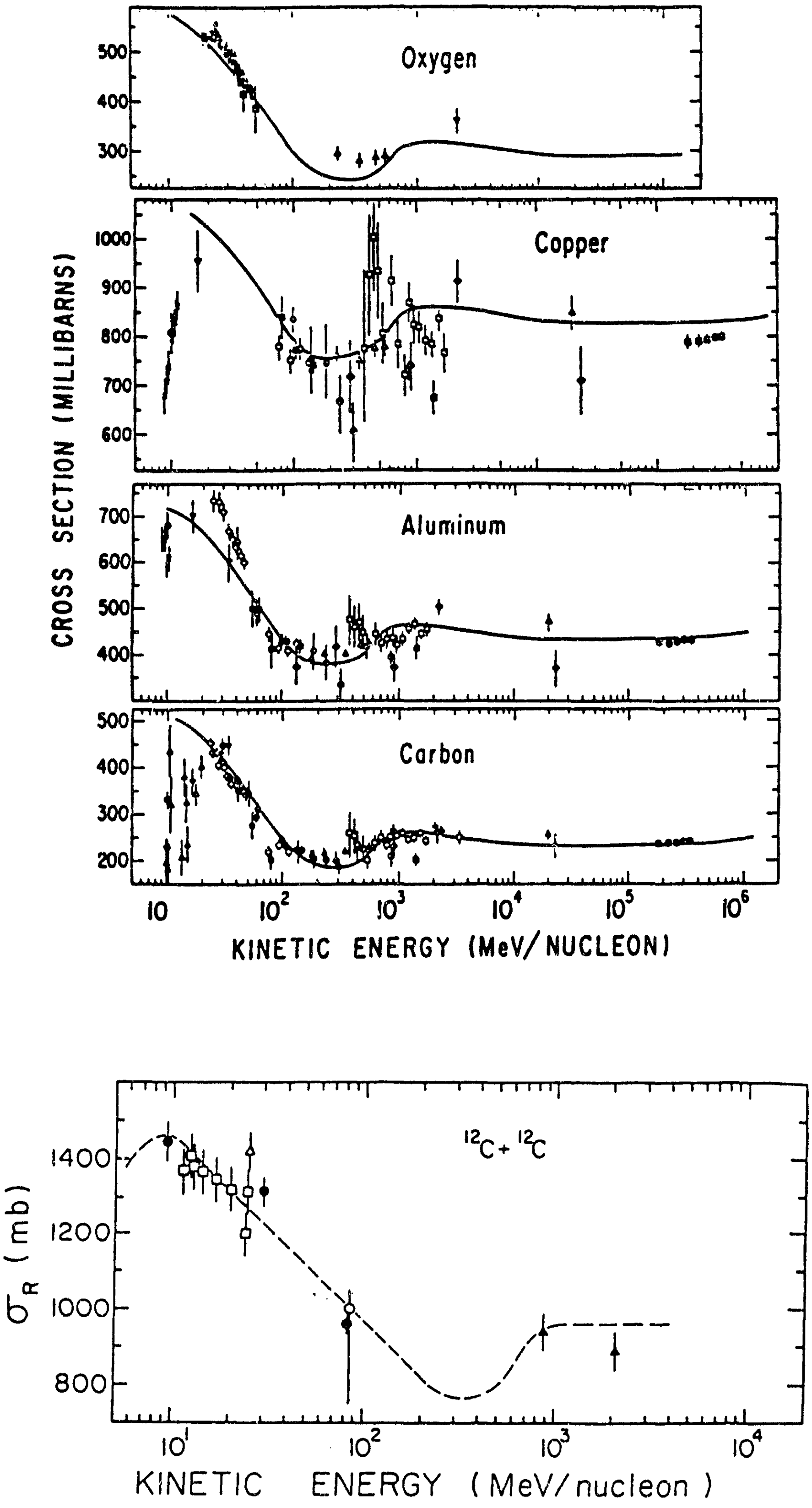

Figure 4. Compiled proton-nucleus total reaction cross sections (top) and $^{12}C + ^{12}C$ total reaction cross section (bottom) compared to model predictions.

3. Excitation Energies

While inclusive reaction experiments are important for determining overall properties of the fragmentation process, detailed evaluation of the mechanisms often requires experiments that isolate the reaction channels. Determining the excitation energy spectrum for a specific channel allows both testing of models and the search for structures that indicate particular mechanisms.[40] For example, models of the fragmentation process such as abrasion-ablation[38] and excitation-decay[9] produce similar results when viewed within the framework of an inclusive measurement. In the simple abrasion-ablation picture, very little energy is transferred into the projectile spectator, while in the excitation-decay model, large energy transfers are possible. The spectrum of excitation energies, then, would be expected to show a long tail to high energy transfers for an excitation-decay process compared to the abrasion-ablation picture.[41] One such test has been made. An analysis of the 3 α dissociation channel in ^{12}C fragmentation on a carbon target showed that none of the current models were in complete agreement with the experimental results.[10]

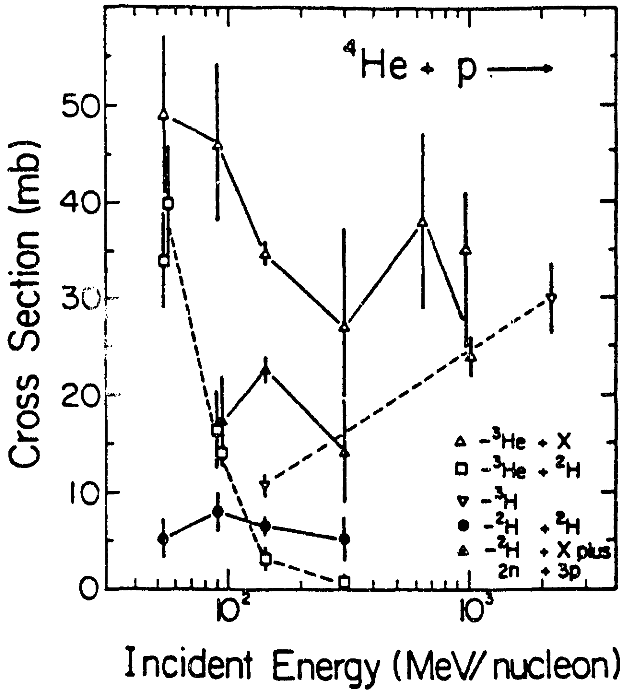

Figure 5. ^{4}He fragmentation cross sections for different reaction channels.

Figure 5 shows a compilation[42] of cross sections for ^{4}He + p into individual reaction channels as well as the inclusive reaction to a ^{3}He final state. At high energies the dominant modes are ^{3}He+n and ^{3}H+p. At low energies proton pick-up to ^{3}He + ^{2}H dominates ^{3}He+n. (Note that the energy dependence of ^{3}He+X is composed of a complicated mix of the different reaction channels.) Further measurements are needed to extend the energies, to refine the measurements, and to investigate the energy dependence of the ^{3}H channel.

Previous studies of ^{4}He fragmentation at 0.4, 1.05 and 2.1 GeV/nucleon[43] found that the transverse momentum distributions contained significant exponential tails and the momentum distributions showed a pronounced forward-transverse asymmetry which was most pronounced for the lighter fragments. For ^{3}He fragments $\sigma_0 = 83$ MeV/c found for high energy ^{12}C and ^{16}O fragmentation.[23]

Thus, the simple high energy fragmentation picture, while useful, does not appear to be in complete agreement with current data. The processes are more complex than previously believed and require careful, high precision experiments.

4. Momentum Distributions

The two components, longitudinal and transverse, of the momentum distribution of individual fragments provide information on the nucleons in the projectile nucleus (Fermi momentum, n-p correlations, substructure, Pauli correlations, collective effects),[21,44,45] on the final state interactions between the fragment and the residual target nucleus,[46] and on the de-excitation of the fragment after formation.[9] Many of these processes are expected to be dependent upon the energy of the projectile.

At high energy the momentum distributions are Gaussian in the projectile rest frame, centered at a velocity only slightly less than the beam velocity with widths that show a parabolic dependence on the fragment mass. The width of the longitudinal and transverse distributions appear to be equal at the 10% level.[23] These observations led to the development of the Statistical Model[7,47] which assumes that the nucleons in the nucleus are independent and their momenta are uncorrelated. This leads to the simple prediction that the widths, σ_l of the longitudinal momentum distributions are given by

$$\sigma_l^2 = \sigma_0^2 \; F(P-F)/P-1 \tag{3}$$

for projectile mass P and fragment mass F where σ_0 is related, in a simple Fermi gas approximation, to the nucleon Fermi momentum. Deviations from the expected parabolic mass dependence and variations of experimentally determined values of σ_0 from the theoretical predictions have been interpreted in terms of nucleon correlations, Pauli exclusion, excited state momentum distributions and substructure within the nucleus.[23,44,48]

An alternative explanation is the Peripheral Model[6] which relates the momentum width to the cluster separation energy and the absorptive cutoff radius of the fragment, noting that due to the peripheral nature of the fragmentation reaction, the Fermi momentum is not completely sampled. Employing a WKB approximation to the projectile wave function and taking an absorptive cutoff radius X_0 and separation energy E_s, this approach yields longitudinal momentum widths:

$$\sigma_l^2 = \frac{\mu}{2X_o}\left[\frac{1+\frac{1}{2}y}{\sqrt{1+y}} + \frac{1}{\mu X_o}\right] \tag{4}$$

where $\mu = \sqrt{2m_nE_s}$ and $y = Z_1Z_2e^2/X_0E_s$. It should be noted that the fragment will survive and be observed for any value of E_s between the fragment ground state and the highest energy particle-stable excited state. Further, the cutoff radius X_0 can be parameterized as $X_0 = r_0F^{1/3}$, and although the fragment mass does not enter explicitly, the parabolic dependence on fragment mass is roughly reproduced since E_s is approximately proportional to the mass number of the removed portion of the projectile times the separation energy of a single nucleon. Coulomb distortions must also be considered, and these can further reduce the width of the longitudinal momentum distribution (Coulomb "drag") especially at low energies. Tests for the models are provided by the energy dependence of the momentum widths and by the excitation spectrum for the final states.

Figure 6 shows our results on the reduced width (σ_0) of the longitudinal momentum distribution for ^{12}C and ^{10}B fragments from ^{16}O interactions compared to a compilation of σ_0 values from the literature.[49] Only the experiments shown as vertical bars in the compilation actually reported momentum widths for a variety of isotopes with the remaining points being single fragment measurements. The dashed curve shows model calculations, normalized at high energy, which would imply the onset of limiting behavior at energies as low as 50 MeV/nucleon.

Our results for ^{12}C (representative of all the A≥12 isotopes measured) show a different energy dependence with a peak in σ_0 around 100 MeV/nucleon. The increase in width over the high energy value is difficult to reconcile with the standard model. However, our results for ^{10}B (representative of all of the isotopes with A<12 measured) show an energy independent behavior, consistent with the dashed curves. The clear implication is that for isotopes with an intact alpha-particle core (^{12}C), the reduced widths show an energy variation, while for isotopes for which the core is destroyed the limiting values apply. This would favor the peripheral model over the simple statistical model for the fragmentation process. However, increased experimental data is needed,

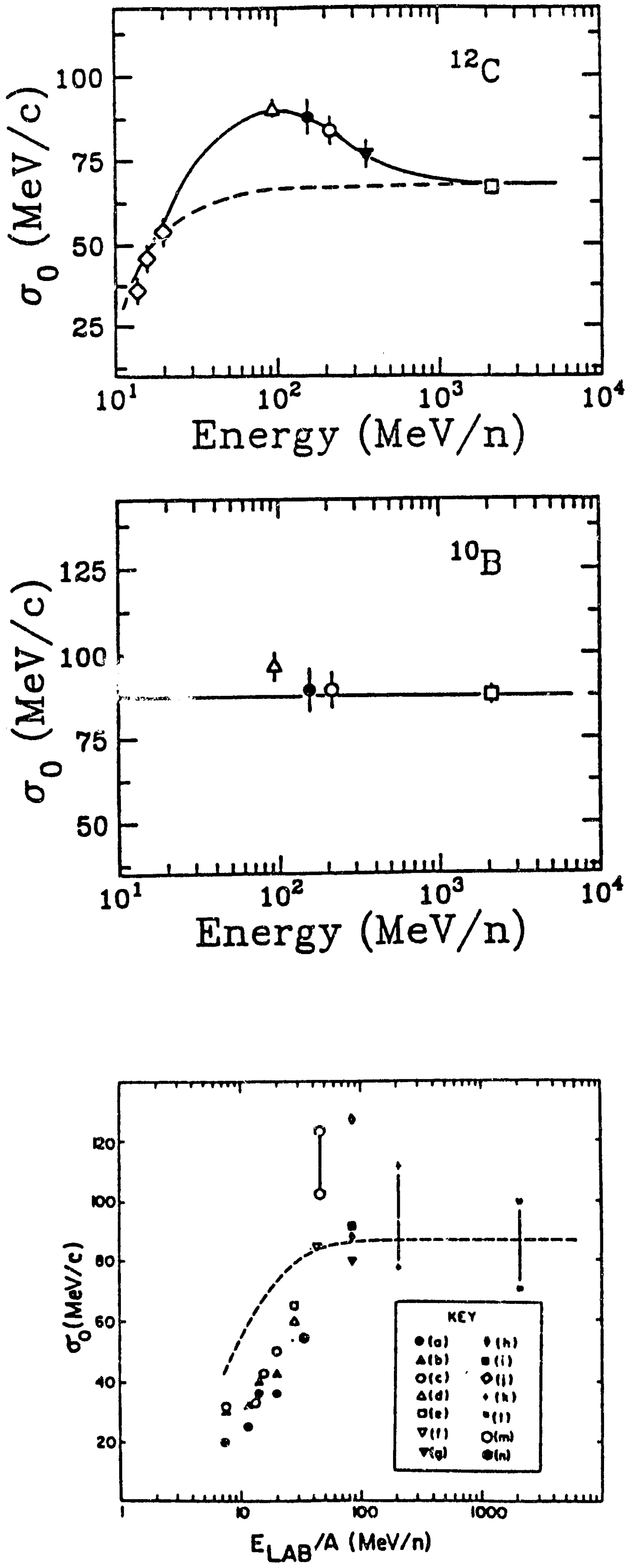

Figure 6. The energy dependence of σ_0 measured for $^{16}O \rightarrow {}^{12}C$ (top) and ^{10}B (center) and predicted from a compilation of data.[49]

especially in the largely unmeasured region above 100 MeV/nucleon and for heavier projectiles, to determine the energy dependence accurately enough to provide constraints on the theoretical models.

For the transverse momentum distribution, experiments have shown that there is an additional component explained as Coulomb interactions of the final states, i.e. orbital deflection.[46] In this case the width of the transverse distribution can be parameterized as:

$$\sigma_t^2 = \sigma_o^2 \frac{F(P-F)}{P-1} + \sigma_2^2 \frac{F(F-1)}{P(P-1)} \tag{5}$$

with σ_0 determined from the longitudinal distribution and σ_2 giving the effect of the orbital deflection. The parameter σ_2 is projectile energy dependent, varying from a value just under 200 MeV/c at ~100 MeV/nucleon to essentially zero at 2.1 GeV/nucleon (where $\sigma_1 \approx \sigma_0$) for ^{16}O interactions. The difficulty in studying the energy dependence of σ_2 derives from the need to unfold the effects of multiple-Coulomb-scattering (MCS) in the target to derive the transverse distribution. However, such analyses are the means to obtain information on the final state interactions.[50] In particular, the degree of orbital deflection provides a measure of the range of impact parameters resulting in a particular fragment.

B. ASTROPHYSICS

Nuclear astrophysics relies heavily on nuclear physics parameters, and significant advances in astrophysical interpretation result from new or higher precision measurements of nuclear quantities. In particle astrophysics, the goal is to interpret measurements of the charge and isotope spectra of cosmic rays made at Earth in terms of the particle's history from nucleosynthesis through acceleration and propagation to arrival at Earth. Nuclear physics plays a vital role in understanding both the nucleosynthesis and, most important for this work, the nuclear interactions that take place in the interstellar medium. The cosmic radiation represents the only sample of matter from beyond our solar system available for direct study, and, as such, provides the key to understanding the processes of element formation, the mechanisms for acceleration of matter to high energies, and the confinement of particles in the galaxy.[51]

One of the "keys" to answering the question of the origin of cosmic rays is the composition of the matter at the "sources". This composition, both elemental and isotopic, reflects the processes of nucleosynthesis and/or selection that contribute to the cosmic rays. Since the source composition can be significantly altered by nuclear fragmentation during cosmic ray transport through the interstellar medium, a good understanding of this propagation is necessary before these effects can be unfolded from the measurements. Moreover, these propagation effects are interesting in their own right, providing information on confinement and the astrophysical role cosmic rays play in overall galactic dynamics.

1. The Source of the Cosmic Rays

GCR composition measurements must be corrected for the changes that occur during propagation through the interstellar medium and within the Heliosphere. The most important is nuclear fragmentation in which primary nuclei emitted from the galactic cosmic ray sources (GCRS) interact with the interstellar medium and are either broken up into individual nucleons, or more probably, fragment into lighter secondary nuclei, thus altering the abundances of the observed particles. Given reliable values for the cross sections of such nuclear processes, it is possible to determine the extent of the propagation effects by examining ratios of pure secondary species (those with little or no GCRS component) to primary species. The "model" or empirical fit

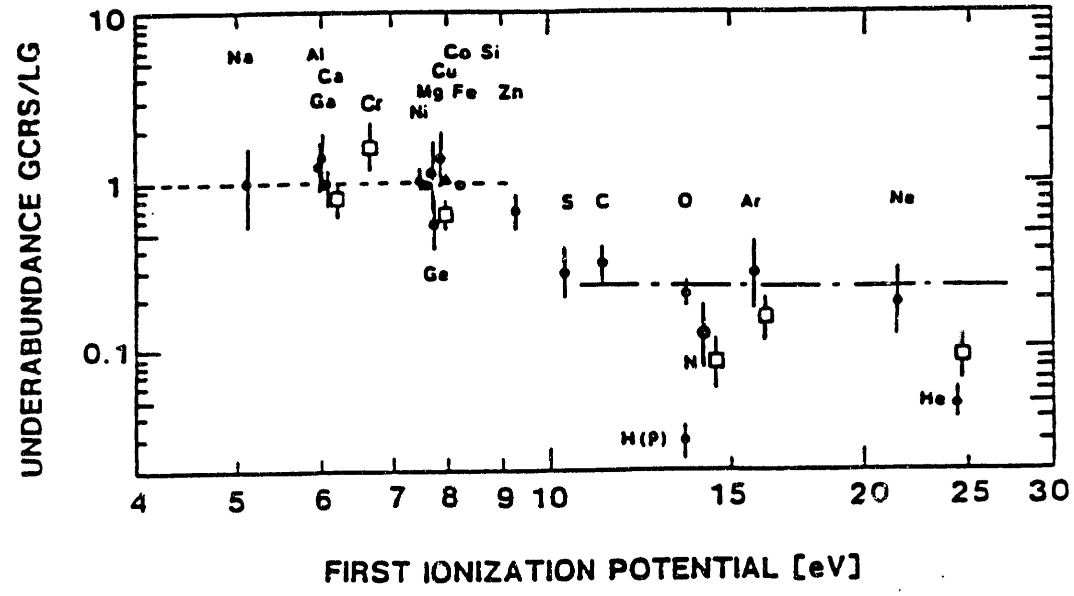

Figure 7. Underabundance ratio for cosmic ray elements as a function of First Ionization Potential.

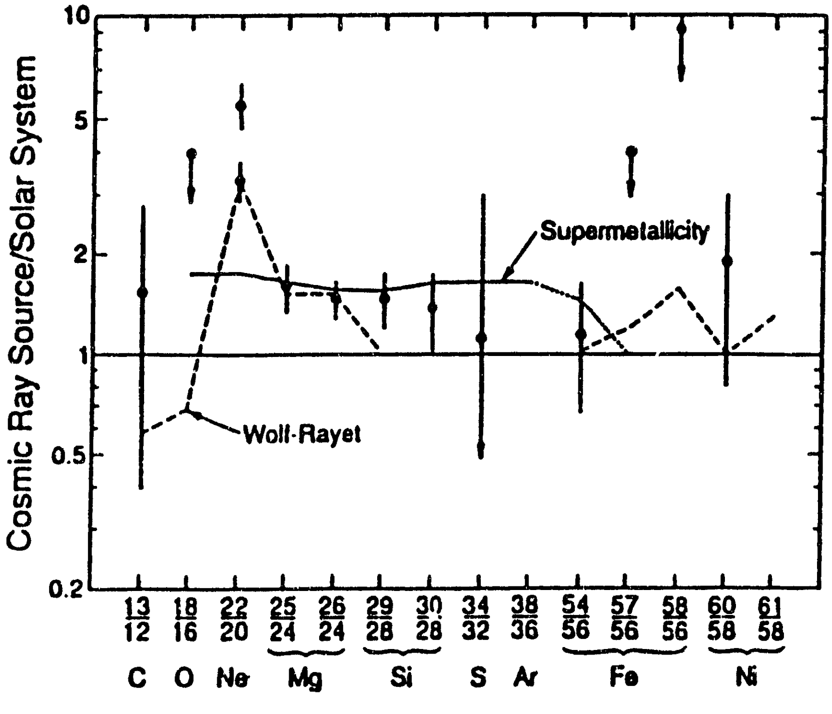

Figure 8. GCRS isotopic ratios normalized to solar system composition.

so determined can then be used to unfold the propagation effects from other cosmic ray species, revealing a number of features of the "source," as:

- **FIP Selection:** Comparison of GCRS abundances to local galactic[52] or solar system[53] abundances reveals that the injection or acceleration mechanism imposes a selection on the nuclei that depends on the atomic properties of each element, such as the first ionization potential (FIP), as illustrated in Figure 7 from ref. 54. Not all elements, however, fit the simple step function ordering. H, He and N fall below the line while Cr and, possibly, C fall above it. Deviations from FIP ordering are interesting, since they indicate a source property. However, deviations may also be due to inaccurate (or unavailable) fragmentation cross sections which are critical for determining abundances for some elements.

- **R-process enhancement:** The UH ($Z>30$) nuclei are dominated by neutron capture nucleosynthesis due to a slow (s) and a rapid (r) capture process. Up to $Z \sim 60$ the fit to a solar system composition source is fairly good, but for higher Z the mainly r-process osmium-platinum ($74 < Z < 78$) group is significantly more abundant than predicted, even for a FIP adjusted solar system composition, indicating excess r-process material[55].

- **Isotopic Anomalies:** Since isotopic abundances are unaffected by atomic parameters such as FIP, observations of isotopic anomalies that are not due to propagation effects must reflect on the source composition. Such anomalies have, indeed, been observed for some elements with $Z < 26$ where current cosmic ray instrumentation can resolve individual isotopes, and a summary of these observations is shown in Figure 8 from ref. 24. The most striking of these is ^{22}Ne/^{20}Ne which was observed to be enhanced above "normal" composition by a factor of 3 - 4.[56] Subsequent measurements showed that the abundance of ^{25,26}Mg and ^{29,30}Si is also high, although the enhancement is not as large.[24,51,54]

A number of models have been put forward to explain this excess of neutron-rich isotopes in the cosmic rays, and predictions are shown in Figure 8. The "supermetallicity" model notes that the amount of neutron-rich material produced during the evolution of massive stars is proportional to the abundance of "metals" ($Z>2$) in the matter from which the star is formed. If cosmic rays originate in regions of the galaxy that are metal-rich, then the neutron-rich enhancements might be explained.[57] The model predicts roughly the same enhancement for Ne, Mg, Si, S and Ar, so an additional source of ^{22}Ne would be required to explain the observations. Another possible model states that part of the GCRS material is from matter expelled from the surface of Wolf-Rayet stars by high-velocity stellar winds.[58] This matter would be rich in helium-burning products such as ^{22}Ne as the hydrogen envelopes of such stars have been previously blown away by the winds. Thus, this model can correctly predict the Ne and Mg enhancements, but unlike the "supermetalicity" model would not show enhancements for heavier elements such as Si, S or Ar.

Further progress on source composition involves improving the precision of the source abundances for both elements and isotopes, including the UH regime. While additional cosmic ray measurements are needed (and are planned), a parallel effort is required for cross section measurements. Not only are cross sections needed to unfold propagation effects, but nucleus-nucleus cross sections are required to correct for interactions within the instrument or residual atmosphere. Such corrections are especially crucial for elements with high total interaction cross sections, such as the UH species. With the cross section measurements performed here, it should be possible to reduce the propagation uncertainty in many of the derived GCRS abundances by about a factor of two.

For the isotopic anomalies, Figure 8 indicates that the isotopes of S and Ar may be the key, provided that the secondary components can be extracted. The secondary component of neutron-rich isotopes of elements in the O - Ar region has a very complicated pedigree due to the relatively similar abundances of cosmic ray species from S to Mn and the dominating presence of ^{56}Fe. For example, two recent experiments[59,60] have each measured the important ratio $^{18}O/^{16}O$. The experimental determinations agree well within the uncertainties. However, one group interprets the data as revealing an excess of ^{18}O at the cosmic ray source while the other group interprets the results as supporting a solar like source composition. The difference is in the fragmentation cross sections employed to calculate the secondary production of ^{18}O from primary Ne-Ca nuclei, and particularly the neutron-rich progenitors, such as ^{22}Ne, ^{26}Mg or ^{30}Si. Since $^{18}O/^{16}O$ provides a key test for the Wolf-Rayet model in Figure 8, answering this ambiguity in interpretation is extremely important. Here our data on neutron-rich beams (^{22}Ne, ^{26}Mg, ^{40}Ar) as well as the ^{28}Si and ^{32}S results can make an immediate, important contribution.

2. The Astrophysics of Cosmic Ray Propagation

Cosmic ray transport is assumed to be a diffusive process which also involves ionization energy loss, nuclear decay (e-capture, β^+, β^-, α and fission), nuclear fragmentation, and escape from the confinement region. Two steady state approximations, the "leaky box" model[61,62] and the "weighted slab" technique[63,64] have emerged as the dominant methods to solve this problem. Figure 9 shows measurements of the B/C ratio compared to a calculation which includes ionization, decay, energy dependent cross sections and an exponential path length distribution (PLD) with an energy dependent mean (X_0), as illustrated in Figure 10. The shaded area is the uncertainty in X_0 derived from the errors in the fragmentation cross sections plus the cosmic ray measurements. The decrease in X_0 with increasing energy above ~2 GeV/nucleon may reflect the power spectrum of interstellar hydromagnetic waves, which control particle escape from the galaxy[65]. The decrease of X_0 below ~1 GeV/nucleon is more of a mystery. The power spectrum of wave turbulence is expected to rise with decreasing energy, implying a continued increase rather than a turn down. An alternate "escape" mechanism at low energy may come from a dynamic halo involving a galactic wind[66]. Other explanations include "magnetic bubbles" which are inflated by the cosmic rays and allow escape into a halo[67] or the reacceleration of secondary species by weak remnant interstellar shock waves[68]. These interpretations are, however, predicted upon the assumption that the propagation model being used and the cross sections employed are both correct, and there is considerable controversy on both points.

Secondary to primary ratios such as $^{3}He/^{4}He$ can provide information on the PLD. Figure 11 shows a comparison of the $^{3}He/^{4}He$ measurements to the predicted ratio (solid curve) using the PLD of Figure 10 and the cross sections from Figure 5. The $^{3}He/^{4}He$ data fall consistently above the predicted curve, a result which can be interpreted as implying a longer confinement for the H-He component. Fitting the majority of this data would require a pathlength inconsistent with the propagation of the CNO elements, leading to the suggestion that the H-He component may have a different "history" than the CNO nuclei.

Alternatively, the cosmic ray measurements could be wrong, or the nuclear cross sections could be in error. The importance of the $^{3}He/^{4}He$ has prompted several new experiments to re-measure this ratio. Results from one of them, SMILI,[69] is shown in Figure 11, after correction for solar modulation, as the boxed region near the peak of the curve. This measurement is in agreement with the predictions, but only sampled the high energy region. The second uncertainty, the cross sections from Figure 5, will be addressed by the analysis of our helium runs listed in Table 1. This should allow the question of a different "history" for the H-He component to be laid-to-rest.

C. APPLICATIONS

The isotope $^{26}Al(T_{1/2} = 0.73$ million years) has a history of various applications as a tracer isotope. In measuring exposure ages of extraterrestrial materials, meteorites and lunar samples, ^{26}Al is employed as a monitor of the proton fluence to which the sample has been exposed.[70] This ^{26}Al is produced principally by proton induced fragmentation of Si, one of the main constituents

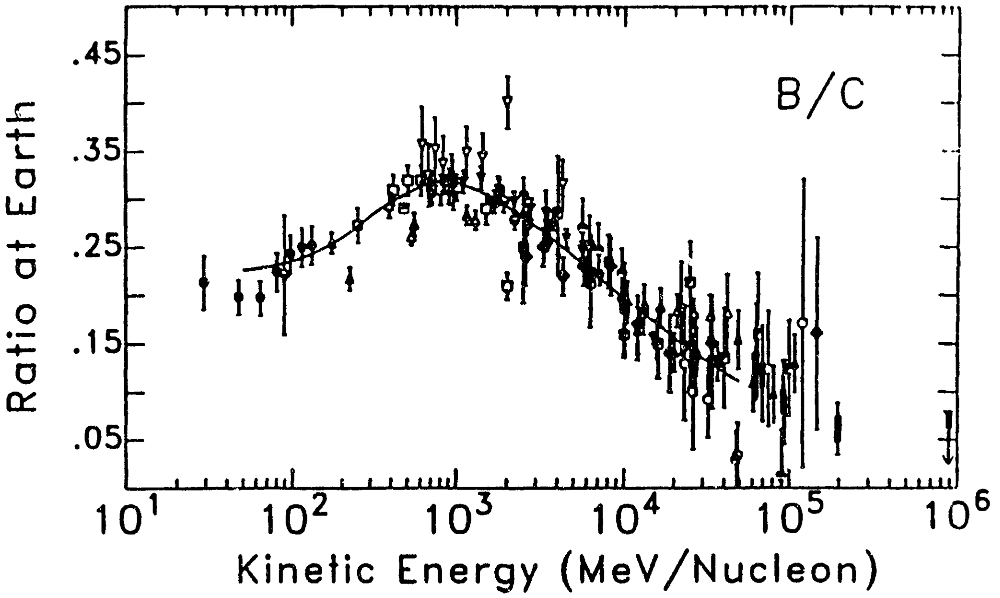

Figure 9. B/C ratio as a function of energy, adapted from ref. 11.

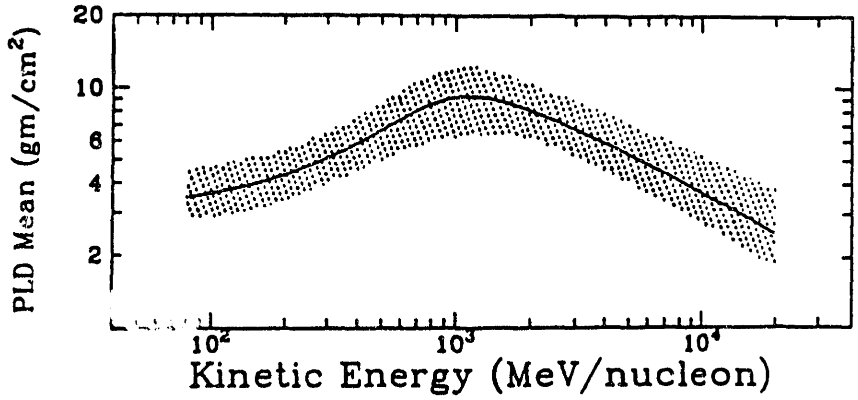

Figure 10. The energy dependence (curve) and uncertainty (shaded area) of the exponential PLD mean derived from B/C observations.

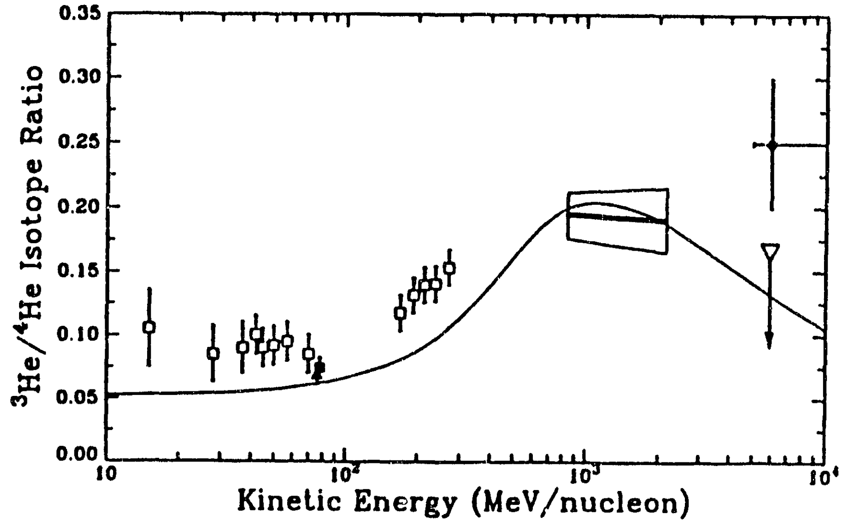

Figure 11. Measurements of ^{3}He/^{4}He compared to a propagation calculation which is consistent with the observed B/C ratio.

of these materials. In the terrestrial environment, ^{26}Al has been investigated as a tracer similar to ^{14}C, but the production via ^{40}Ar + p → ^{26}Al in the atmosphere is relatively small.[71] In astrophysics, ^{26}Al is a product of explosive nucleosynthesis, and the gamma ray line from its decay has been detected in several regions of the galaxy.[72] In this application, ^{26}Al becomes a tracer of recent nucleosynthetic activity in the galaxy. The ^{26}Al can also act as a tracer of the confinement lifetime of cosmic rays. The principal sources here are ^{27}Al, ^{28}Si, ^{32}S, ^{36}Ar and ^{56}Fe.

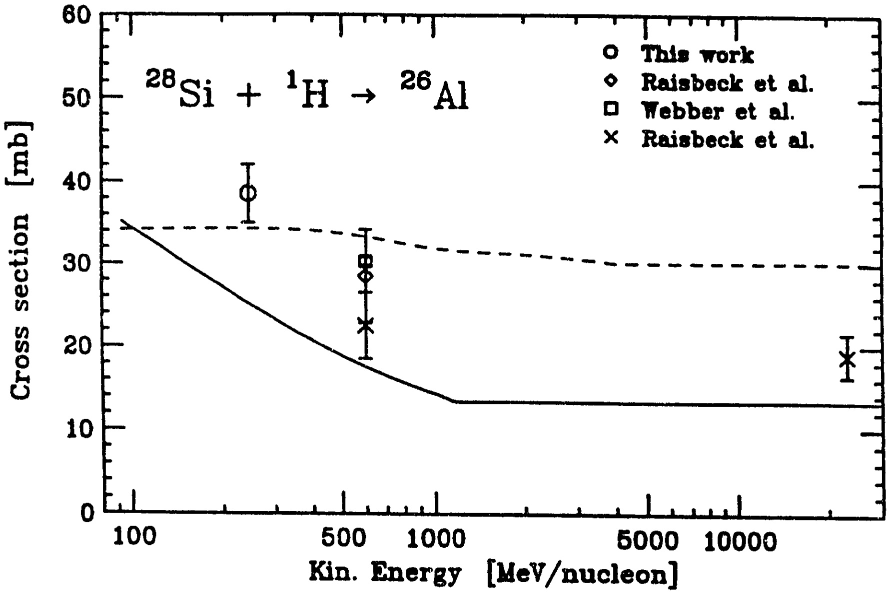

Figure 12. ^{26}Al production from ^{28}Si compared to semiempirical predictions.

Figure 12 shows the results to date for ^{26}Al production from ^{28}Si by protons. There are several measurements at 600 MeV/nucleon, which cover about 30% in cross section, a single measurement at very high energy and our result at 245 MeV/nucleon. The semiempirical predictions[26,27] from the two different formulae are shown as the solid and the dashed lines. Note that neither prediction agrees very well with the data, although the solid line appears to have the "best" energy dependence but an absolute normalization that is too small. The increase at low energies indicated by our results is not reproduced by either prediction. Modifying the excitation function that has been used previously will have important implications for the use of ^{26}Al as a tracer. Further, our data on Argon fragmentation will be particularly applicable to the use of ^{26}Al in the terrestrial environment.

On a completely different subject, the announcement by President Bush of a concerted national effort to establish a permanent base on the moon and then a crewed trip to Mars -- the Space Exploration Initiative -- has brought the question of space radiation exposure into prominence again, after almost two decades. No longer will humans be confined to low Earth orbit for which the Earth's magnetic field provides the needed shielding from galactic cosmic rays and solar flare particles. Even though no appreciable funding has yet been provided for SEI by Congress, the DOE has been tasked to develop radiation exposure standards and shielding models for the space vehicles.

It has already been realized that our knowledge of the modes of nuclear fragmentation of heavy nuclei is insufficient to calculate the secondary particle spectra behind a given amount of spacecraft material or habitat shielding. This limits the ability of mission planners to design a realistic scenario for either a lunar base or for the type of spacecraft needed for a Mars mission. What is needed are new measurements, particularly the biologically important neutron production channels, from the fragmentation of the (astrophysically) most abundant beam species in a variety of target materials at several energies below ~1 GeV/nucleon. The data will need to be fit to predictive models, including target scaling and energy dependence, to be employed for resolving the shielding issue. The type of data that we have obtained is necessary to develop the predictive models needed for both exposure limits and shielding designs. We have already been receiving requests for our cross section data, as soon as the final results are available.

D. EXPERIMENTAL CONFIGURATIONS

1. Beam 40 Experiments

For the inclusive studies at B40 in the intermediate energy region, the experimental configuration shown in Figure 13 was developed. The beam enters from the right, passes through the hole in anti-coincidence scintillator S2 and is focused onto the solid targets located in the B40 vacuum tank just downstream of bending magnets M2M3. The fragments emitted from interactions in the target spread spatially, depending upon the fragment emission angle, over the ~7 meter path to the window, and the angular distribution can be studied by moving the detector (SCOPE) along the B40 rail. At the target, the incident beam is counted by a scintillator S1 (not shown) and is further constrained to the center of the target by an UDEW consisting of four remotely controlled, moveable scintillators that open and close to produce a rectangular "hole" through which a valid beam particle must pass. This arrangement ensures minimum mass (S1 + target) in the beamline up to the vacuum tank window. Bending magnets M2M3 are used only to put the beam on the center of the target and to hold the beam position steady.

The goal of this configuration is to measure the two components of the momentum for each of the isotopes produced in the fragmentation process. Identifying isotopes requires an apparatus with good mass and energy resolution. Our collaboration designed and built a solid state detector telescope (SCOPE) shown schematically in Figure 14 (top), which mounts on a moveable cart attached to the rail in the B40 zero-degree spectrometer. At the rail the telescope covers an angular range of 0.35°, but this can be reduced, at the cost of statistics, by restricting the aperature. The telescope consists of fast scintillators (G1, G2, HA, HB) for triggering, a position sensitive front

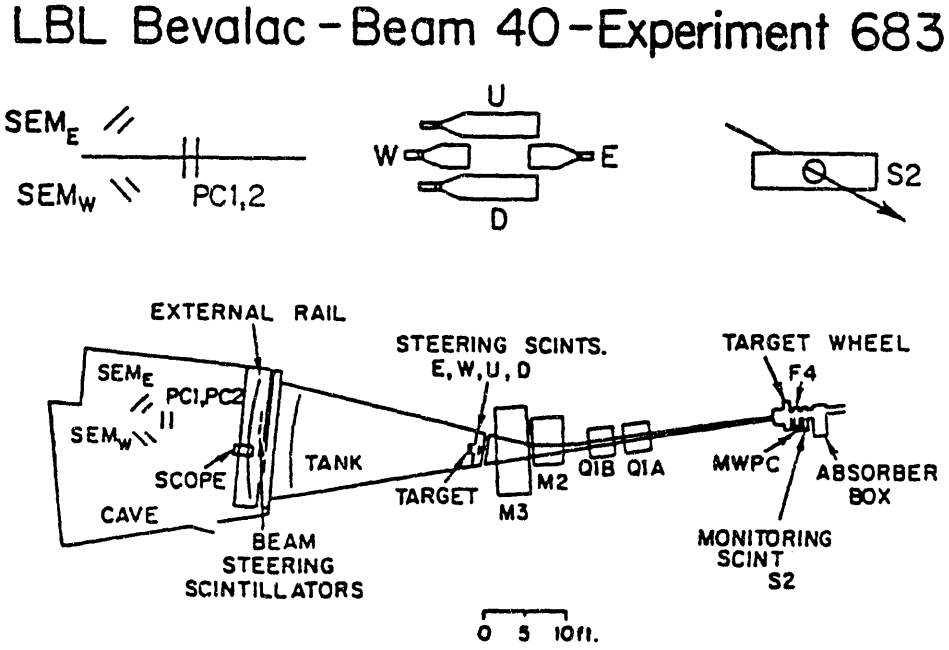

Figure 13. Experimental Arrangement for the B40 runs at the Bevalac.

section to measure the trajectory of each event, and a stack of solid state detectors in which the particles come to rest, providing the total energy of the particle and isotope identification by the ΔE-E technique.[12] A series of measurements (both target in and target out) are taken at various locations along the rail to trace out the angular distribution of the fragments, to study the transverse momentum and obtain the integrated cross section. Targets are typically ~1 g/cm^2 thick.

For runs near zero degrees (in the direct beam) normalization is obtained directly by counting the incident particles in S1. For larger angles (>0.5°) the beam intensity is increased to maintain the data acquisition rate at a high level. Scintillator S1 saturates, and normalization is obtained from scintillators PC1, PC2 viewed by several Secondary Emission Monitors (SEM's) located in the back portion of the cave.

Over the course of this program, a number of improvements have been made to this basic configuration. In the first run, scintillator S1 was located upstream at F4 just behind S2. This resulted in fragments from S1 being focused by Q1A&B and M2M3 in the cave, making background subtraction very difficult. This was remedied by moving S1 into the vacuum tank. Two types of trajectory systems have been employed. Figure 14 (top) shows a CPSD which are strip cathode solid state position sensing detectors (PSD), fabricated at the University of Chicago, and read out through a resistive divider network.[13] Each detector is 500 µm thick, and they are arranged in 2 X-Y layers to give the particle trajectory. These CPSD's replaced the LBL resistive layer PSD's used in our first run because the CPSD's have less non-linearity than the LBL PSD's and, therefore, require less beam time for calibration. The CPSD's, however, are ~15 years old and do have some dead or broken strips which complicates the analysis. For our most recent run, the PSD's were replaced with a new, low mass, drift chamber (DC) system which provided 8 measurements of the X and 5 measurements of the Y coordinate over a linear distance of ~50 cm. The telescope hardware and the DC are shown schematically in Figure 2 (bottom). Inherently, the DC can provide much better trajectory definition than the solid state PSD's.

Crucial to the success of this configuration is the long term stability of the magnets (especially M2M3 and the quads) along the B40 line. (This was demonstrated experimentally during our first run in which the magnet power supplies did not regulate properly at the low rigidities employed in this experiment with the result that the beam moved spill by spill. This problem was solved for our second run, and only small drifts in the magnets were observed. The most recent run had variations in upstream magnets X1M6 and M1 which caused beam instability.) Each "event" is required to pass through S2 and UDEW (and, therefore the central portion of the target) to be considered "in-geometry". Any large beam movement removes particles via S2 or UDEW thereby reducing the event rate. In the cave, beam motion can affect the normalization through changes in the relative solid angle of the SEM's. For the last two runs, a second UDEW was placed in front of PC1, 2 to monitor beam motion. In addition, the latest configuration employed two sets of SEM's, one pair above and one below the beam line with different solid angles, to try to increase the overlap of the linear intensity region between S1 and the SEM's. This was done to improve the scaling from ~10^5/spill, where S1 begins to roll off to the 10^7/spill needed for the very large angle runs.

2. HISS Experiments

For the higher energy HISS runs, a completely different beamline and experimental configuration was used. Figure 15 shows the HISS arrangement for the E938 experiment. The HISS superconducting dipole magnet provides separation of the fragments by their rigidity. Downstream positions are measured by the Drift Chamber and particle velocity is measured by the Time-of-Flight (TOF) wall and the VMD (Velocity Measuring Device). The Italian neutron detector, MUFFINS, was aligned with the upstream beam path to study undeflected particles.

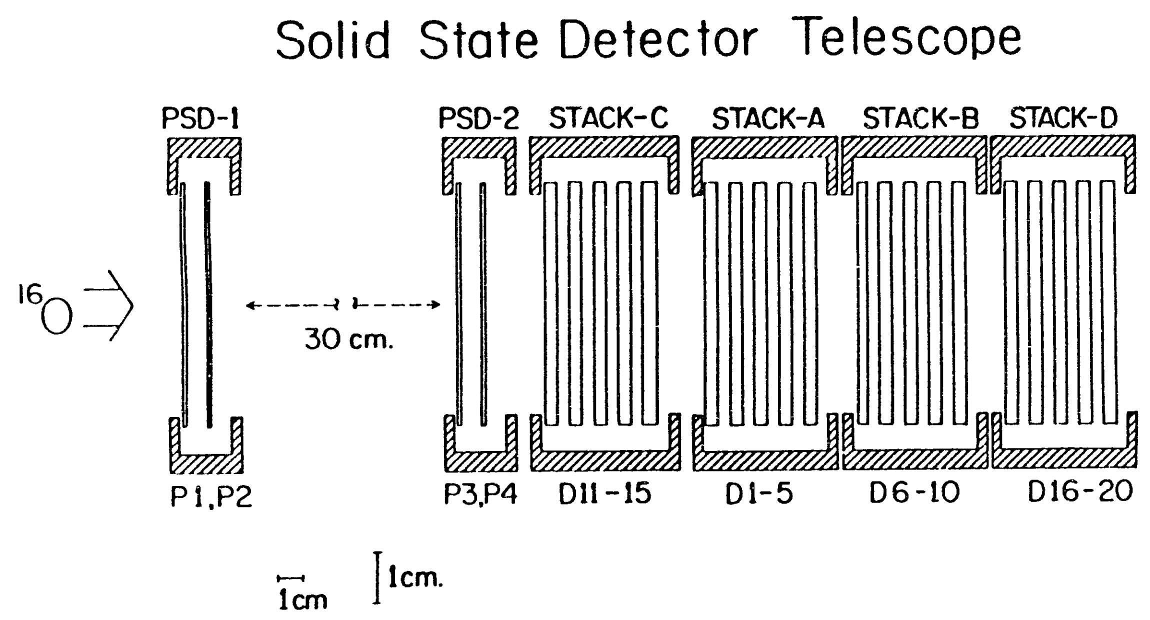

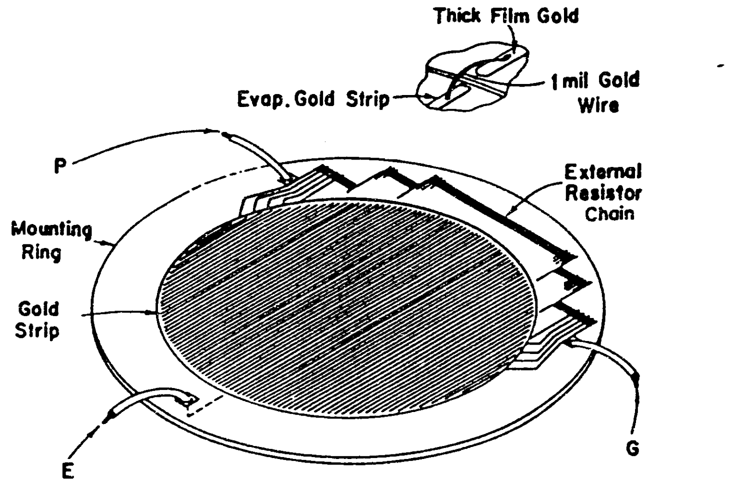

The University of Chicago
ONE-DIMENSIONAL POSITION SENSITIVE
SILICON DETECTOR

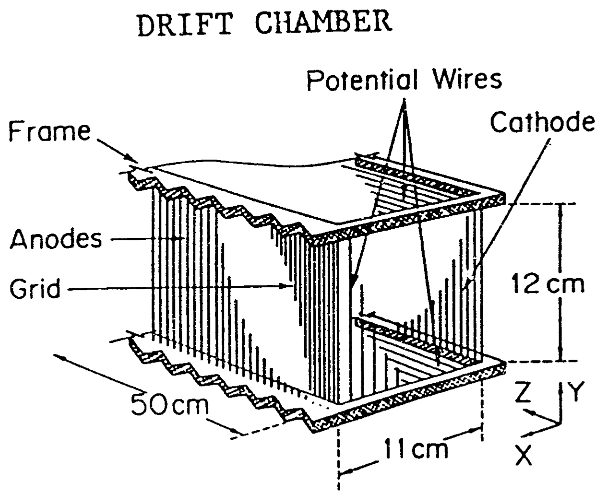

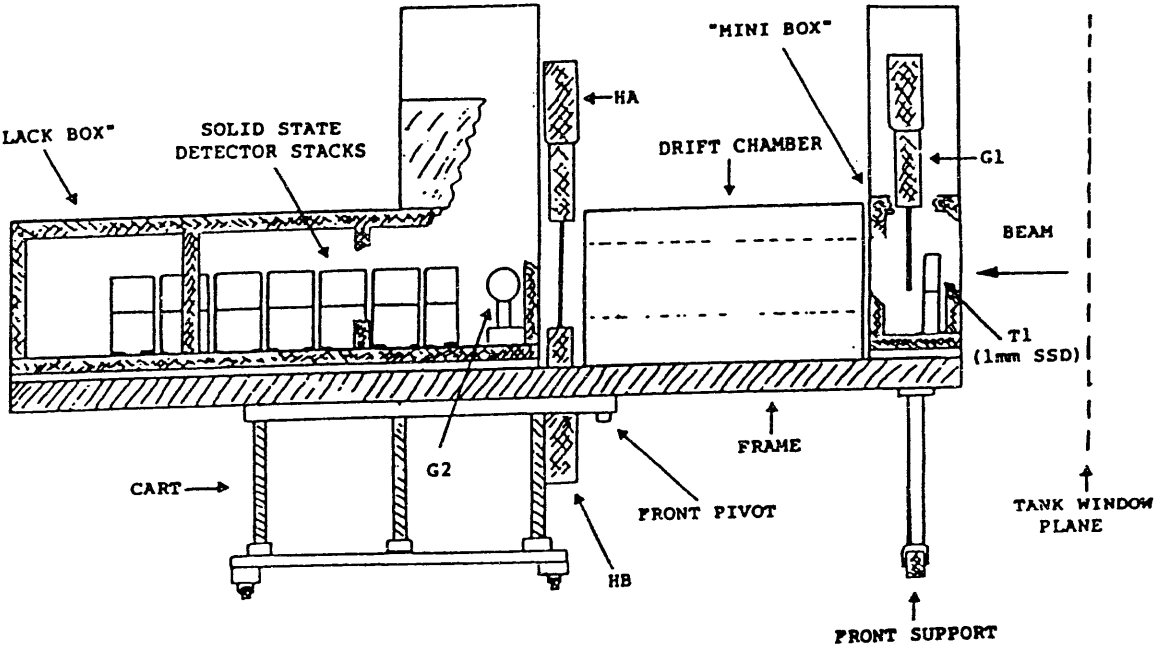

Hardware Configuration

Figure 14 The SCOPE System

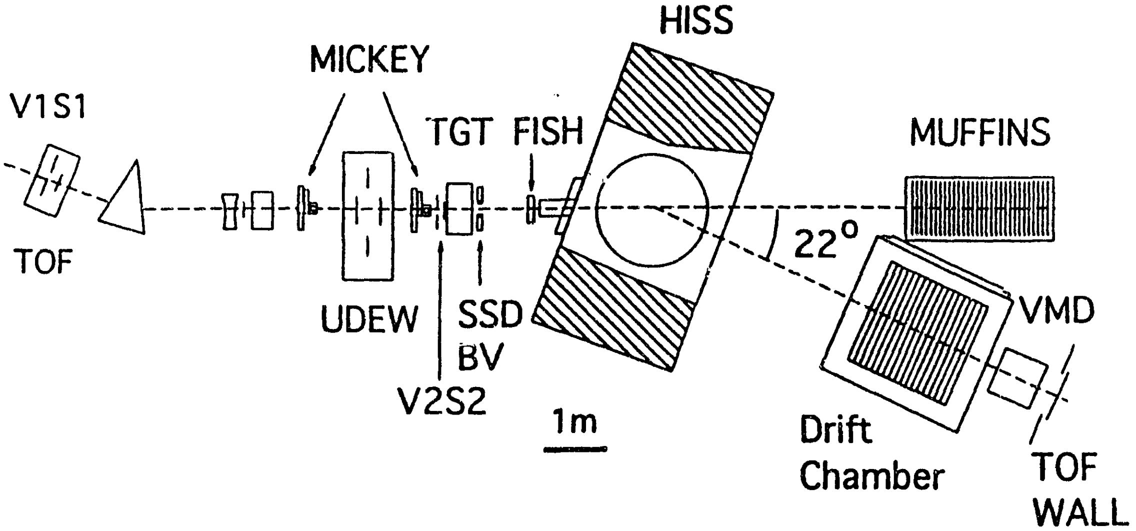

Figure 15. Experimental arrangement of the HISS facility.

There are five primary subsystems included in the experiment. The Beam Detection System (BDS) constitutes the first subsystem and is used to restrict the phase space of the incoming beam. The BDS is constructed to determine the incident beam particle's position on the liquid hydrogen target and to return a post-target/pre-magnet position and direction for each fragment. The second and third subsystems are the liquid hydrogen target and the HISS dipole, respectively. The fourth subsystem, a large multiplane drift chamber has been used to determine the trajectory of the projectile fragments. This trajectory information when coupled with the magnetic field measurements allows us to determine the precise momentum of the projectile fragments. The fifth and final system, a highly granulated time-of-flight wall composed of scintillation plastic, is used to return the charge and velocity of the individual projectile fragments. For higher energy (e.g. 1.6 GeV/nucleon) the TOF is supplemented by a total internal reflection Cherenkov counter (VMD) which can be "tuned" for a given energy range.

Beam Detection System (BDS): The primary function of the BDS is to monitor beam quality and provide a reliable beam count. The system consists of two position sensitive detectors (MICKEY), two small scintillator paddles (S1 and S2), three large paddles having holes at their centers (1 cm diameter for V1, 2.54 cm diameter for V2, and 4.5 cm diameter for V4), a 7.5 cm diameter 0.1 cm thick Si(Li) detector (SSD), a third small scintillator paddle (BV) and a Fiber Scintillator Hodoscope (FISH). Scintillators S1 and V1 are placed at the beam focus 10 m upstream of the target where S1 functions as the start detector for the TOF system and V1 is incorporated to flag any particles outside the acceptable phase space for the system. UDEW(Up-Down-East-West) is an individually adjustable four scintillator anti-coincidence device similar to that shown in Figure 13. It can be adjusted up-down and east-west to narrow in and select only the center of the beam. Together with the S2, V2, UDEW, and the post target hole veto V4, S1 and V1 constitute the main trigger for the experiment.

The Mickey detectors, composed of a single sheet (1 mm) of scintillator mounted diagonal to the beam and viewed by two phototubes, are placed 3 m and 4 m upstream of the liquid target to vector the incoming beam particles. The Si(Li) detector and BV scintillator after the target are used to determine if the incoming beam particle underwent a target interaction. The discriminator threshold on BV was finely tuned at a level between Z_b and Z_b-1 and the signal was used in a second experimental trigger to tag those events in which a nuclear collision occurred.

The FISH detector consists of two 12 cm ribbons of 0.1 cm scintillating fibers oriented at 90° with respect to one another and placed transverse to the beam direction 1 m downstream of the target. The ribbons, both viewed by a single 256 channel photomultiplier tube, supply a post-target/pre-magnetic field position for the fragments which combine with the upstream beam vector to define the trajectory of the fragments into the HISS magnetic field.

Liquid Hydrogen Target (LH_2): The target system contains approximately 1 liter of liquid hydrogen that is condensed directly into a target vessel. The necessary cooling is provided by a reservoir of liquid helium in a dewar mounted beneath the target assemblies. The liquid hydrogen, contained in a multi-walled stainless steel cylinder with 0.01 cm titanium windows, is held at a working pressure of 2.07 atm and a temperature of 18.98°K by a temperature/pressure controlled feedback system. The monitoring equipment held the H_2 liquid density of 0.0728 g/cc to ±0.12% during data taking. In addition, there is an exact mass equivalent dummy target that can be rotated into the beamline for "target out" measurements.

Drift Chamber (DC): The Drift Chamber, used to track the projectile fragments, consists of fifteen 200 cm tall by 300 cm wide by 20 cm thick wire modules. Each wire module consists of a sense plane which is sandwiched between two high voltage planes each of three planes of wire, staggered by 2 mm and held at different negative potentials to achieve the optimum field shape for the 1 cm by 2 cm cells. The wires are oriented at 0°, -30°, and +30° to form S, T, and U planes respectively. The current chamber arrangement is T-S-U-S-T-S-U-S-T-S-U-S-T-S-U The fifteen planes compose a single gas volume which is filled with P10 (90% Ar:10%CH_4) gas and sealed on either side by a double 0.5 mm mylar window. Particle positions returned by the drift chamber, when combined with the upstream position measurements and the magnetic field map, yield a rigidity measurement, R, for each particle. The drift chamber resolution has been on the order of 0.25 mm, which corresponds to a rigidity resolution of $d(R)/R=2\cdot10^{-3}$ for Ar at 1600 MeV/nucleon. A more complete description of this detector is given by Kobayashi.[14]

Time-of-Flight (TOF) Wall: The TOF wall was used to measure the charge and velocity of the fragments. At the heart of the TOF wall is a double layer of 2 cm wide by 120 cm long, 0.7 cm thick plastic scintillation slats. The two layers of slats are mounted vertically and shifted by 1 cm with respect to one another in the lateral direction to increase the position resolution and to ensure the coverage of the detector. This 100 cm by 100 cm inner wall is framed on all sides by 48 cm of 8 cm wide slats to increase the detector's effective aperture. All slats are viewed by two photomultiplier tubes, placed at either end, which allows a vertical position resolution of approximately 10 cm. In the low charge and low energy regime, the TOF wall served the dual purpose of determining the charge and the velocity of the projectile fragments. In data runs with ^{40}Ar at 400 MeV/nucleon, charge resolutions of 0.25 e FWHM and time of flight resolution of $\sigma \approx 150$ ps were obtained. The TOF wall also provided a rough position measurement to complement the trajectory information obtained from the DC.

Multiple Function Neutron Spectrometer (MUFFINS): While not integral to the primary goals of this experiment, neutron detection provides a valuable addition to the dataset and may prove invaluable in the refinement of a fragmentation model for nuclear collisions. The MUFFINS detector consists of thirty 3 cm thick 100 cm diameter disks of scintillation plastic. Each disk is viewed by six 3 cm photomultiplier tubes spaced at 60° intervals about the circumference of the disk. The MUFFINS detector has achieved a timing resolution of 130 ps FWHM which corresponds to a position resolution of 3 cm in both X and Y directions for neutrons emitted from ^{32}S at 600 MeV/nucleon.

E. THE OVERALL DATABANK

Combining the B40 work with the HISS runs that have been completed yields a rather large dataset for the study of the projectile fragmentation process. This dataset is summarized in Table 1

TABLE 1: DATASETS ACQUIRED

	Beam	Energy MeV/n	Facility	Angles	Comments
1)	^{16}O	225	B40	6	limited statistics
2)	^{16}O	170	B40	11	good run
3)	^{16}O	360	B40	6	low statistics
4)	^{56}Fe	270	B40	10	no mass resolution
5)	^{28}Si ($\Delta Z=1$)	1050,550 375,260	B40	1	limited statistics 0° only, 5 targets
6)	^{20}Ne	225	B40	2	unstable beam/low statistics
7)	^{28}Si	245	B40	10	spill structure/beam problems
8)	^{4}He	2100	HISS	--	low statistics
9)	^{20}Ne	2100	HISS	--	good run/DC problems
10)	^{36}Ar	400	HISS	--	"shakedown" run
11)	^{32}S	400,600	HISS	--	LH_2 target
12)	^{36}Ar	400	HISS	--	LH_2 target
13)	^{40}Ca	400,600	HISS	--	LH_2 target
14)	^{56}Fe	400	HISS	--	LH_2 target
15)	^{4}He	400,800	HISS	--	LH_2 target
16)	^{22}Ne	400,600,910	HISS	--	LH_2 target
17)	^{26}Mg	400,600	HISS	--	LH_2 target
18)	^{32}S	800	HISS	--	LH_2 target, low statistics
19)	^{36}Ar	600,800	HISS	--	LH_2 target
20)	^{40}Ar	393	HISS	--	LH_2 target
21)	^{40}Ca	800	HISS	--	LH_2 target
22)	^{52}Cr	400	HISS	--	LH_2 target
23)	^{56}Fe	1600	HISS	--	MG failure/low statistics
24)	^{58}Ni	400	HISS	--	low statistics
25)	^{56}Fe, ^{58}Ni	600	Separate Detector System	--	Thick Targets

-- For (1)-(5) and (7)-(9), CH_2-C subtraction gives H cross sections.

-- (6), (10) and probably (23) yield no scientific data.

-- (9) requires extensive software development for the drift chamber.

which shows the different runs, the angles studied (for B40 -- at HISS all angles are recorded), and comments on each of the runs. For each of the B40 runs, targets of C, CH_2 and blanks were employed as a minimum, with heavier targets studied as time permitted. Run 6 yielded essentially no useful data since the Bevalac magnet controls were malfunctioning and could not produce a stable beam for the experiment. Run 4 was taken to determine if isotopic resolution for elements as heavy as iron was possible with the apparatus. The answer was negative, and our iron fragmentation study relies on run 14 taken as part of the HISS runs. The two major HISS runs include beams investigated during April, 1990 (10-14) and April, 1991 (15-24). From the B40 work we have obtained (a) a relatively good inclusive dataset for ^{16}O covering part of the intermediate energy region, (b) a dataset to study the energy dependence of the total cross sections for ^{28}Si in a variety of targets over the range in which energy variations are expected, and (c) a single energy point for studying the isotopic composition of ^{28}Si fragments.

Our first HISS run with ^{4}He at full energy, run 8, yielded only a small dataset, so ^{4}He was re-run at two lower energies with the liquid hydrogen target. Overall this should provide the needed information on ^{4}He break-up, and one of our graduate students will concentrate on this data as his thesis project.

For the hydrogen target data we now have 2-3 energy points for the A/Z = 2 beams ^{32}S, ^{40}Ca, ^{36}Ar, and we have several energy points for neutron rich beams of ^{22}Ne, ^{26}Mg and ^{40}Ar. This will allow direct comparison of the fragmentation of the two beam types and will answer the questions about neutron rich species producing neutron-rich fragments with large cross section. Finally, the runs with ^{52}Cr, ^{56}Fe and ^{58}Ni will permit the fragmentation of the iron peak elements to be investigated in detail.

III. ANALYSIS STATUS

Here we describe the status of the HISS (E938H) and low energy ^{16}O, ^{28}Si data analysis. This description includes a discussion of the analysis procedures and techniques, detector calibrations, data selections and normalizations. Finally current cross section results available from this analysis are also presented.

A. STATUS SUMMARY

Figure 16 graphically summarizes the current analysis status of the dataset described in Table 1. This figure includes all beams currently being analyzed, but excludes those that are likely to yield little to no scientific results (270 MeV/nucleon ^{56}Fe, 225 MeV/nucleon ^{20}Ne and 1600 MeV/nucleon ^{56}Fe) and those where the primary analysis is taking place at a separate institution (2100 MeV/nucleon ^{4}He, 2100 MeV/nucleon ^{20}Ne, 600 MeV/nucleon ^{56}Fe and ^{58}Ni). In Figure 16 each beam species/energy is listed along with the major analysis milestones, including initial archiving, detector calibrations, processing and data selection/normalizations, leading up to the final results. A solid bar indicates that the milestone has been completed to final status, while a shaded bar indicates that the task is in a preliminary state. Milestones not applicable to the analysis of a particular dataset are indicated by a "n/a". In general the figure indicates that the majority of the analysis effort for the low energy B40 data has been completed or is nearing completion, and that charge changing cross sections are available for essentially all the HISS beams but considerable more work is needed before the isotopic cross sections can be obtained.

The detector calibrations for, in essence, all of the B40 runs appear to be in a final state. The exception is the 225 MeV/nucleon ^{16}O data which is from our earliest run and may still require some calibration refinements. Also note (from Table 1) that only the 245 MeV/nucleon ^{28}Si used a full detector complement with measurements at multiple angles and, thus, is the only silicon run where isotopic cross section results can be obtained. The remaining Si data used a detector subset to investigate the energy-dependence of nucleus-nucleus total interaction cross sections and therefore full calibrations are unnecessary. Still remaining in the B40 analysis is to finalize the data selection, isotope yields, run normalization, background corrections and angular distributions for the ^{16}O data and to obtain final momentum distributions for all the B40 measurements.

The HISS analysis can be split into two parts involving only the detectors upstream (UPS) of the HISS dipole magnet and the detectors downstream (DWS) of the magnet. With the upstream detectors, charge changing cross sections can be obtained independent of determining the fragment rigidity, and over the last year we have devoted a majority of our HISS analysis effort to finalizing the UPS calibrations. This has included: (1) calibrating the beam particle position sensing detectors and determining the incoming beam vector, (2) examining the beam characteristics and diagnostics and determining parameters for each run that are used to define "good" beam data, (3) determining the target liquid hydrogen density from the measured temperature/pressure and convolving the projected two-dimensional beam profile onto the target aperature to obtain the effective target thickness for each run, (4) Calibrating the charge-sensing detectors located just downstream of the target (BV, SSD) and studying the fragment angular acceptance of these detectors. These calibrations, and thereby the final total and partial elemental cross section results, have been completed for all beams Ne and heavier. The exceptions are the two helium beam energies which are currently the subject of a graduate student (X. Zhang) thesis. Mr. Zhang is also participating in the "heavy" beam analysis to become familiar with the methods and techniques that can then be applied to his thesis analysis.

The HISS isotopic cross sections require, in addition to the information obtained during the UPS analysis, full calibrations of the downstream drift chamber (DC) fragment trajectory detector, light attenuation, charge and timing calibrations of the TOF detector, three levels of processing (1, 2a, and 2b), pseudo-mass calibrations and data selection. All these steps have been completed

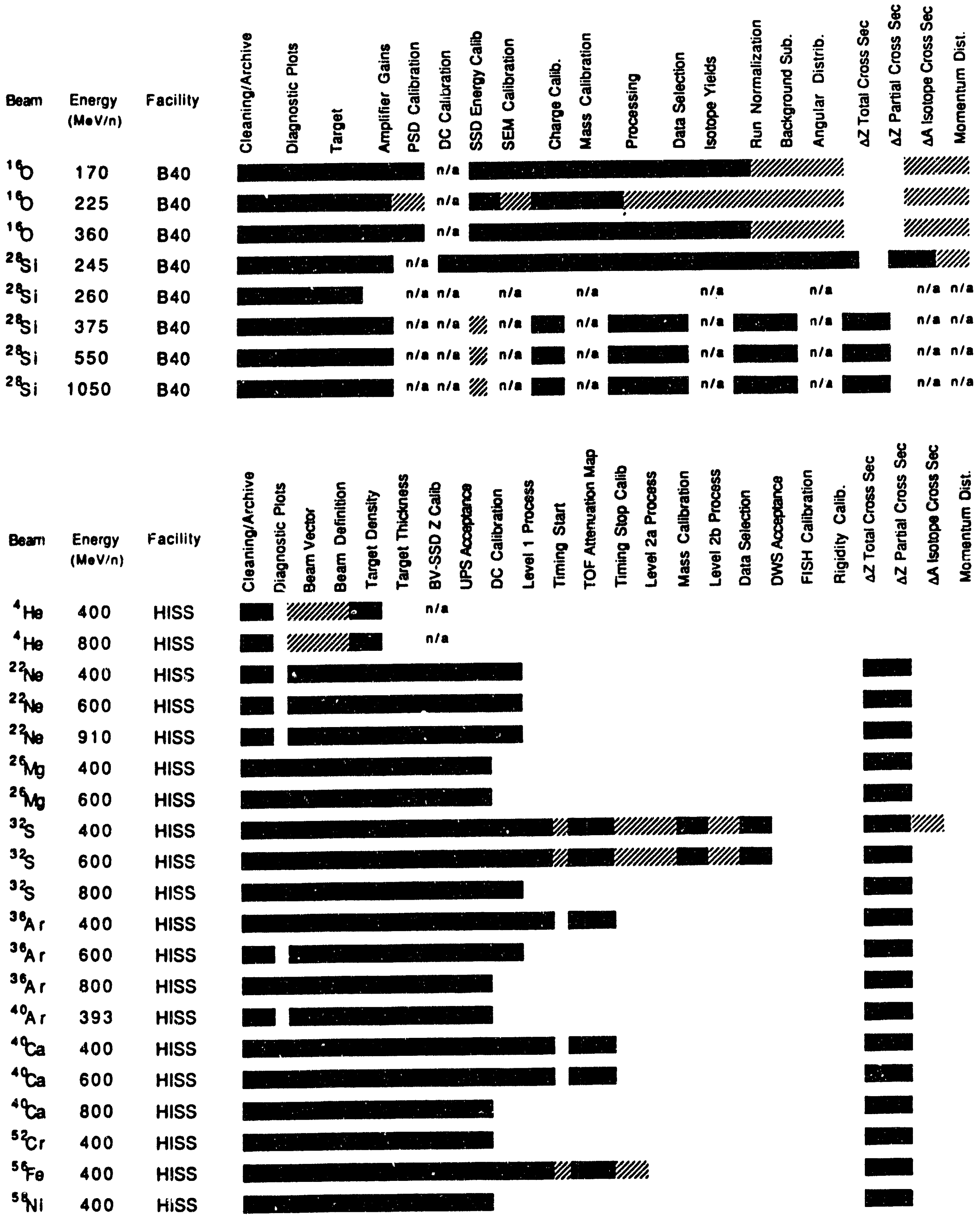

Figure 16. Summary of the low energy (B40) and high energy (HISS) analysis status.

only for the 400 MeV/nucleon ^{32}S beam which has been used to develop and refine the analysis techniques and processing programs that can then be applied to the remaining beams. These procedures have recently been finalized, and we are beginning to shift the HISS analysis from a purely "interactive" mode to a "production" mode.

Currently, the HISS isotopic analysis uses a constant field approximation for the HISS dipole magnet and a relative rigidity parameter. While this is sufficient to resolve isotopes to ~0.2 amu over much of the charge range, this technique may be insufficient to resolve the Fe and Ni fragment isotopes and to obtain the absolute momentum distributions for the fragments. Therefore, with the HISS production analysis underway, we will need to begin developing the calibrations and processes necessary to determine an absolute rigidity for each fragment. This will involve completing the calibration of the "FISH" fragment position sensing detector and developing a procedure for tracing the fragment trajectory through the real HISS field and iterating the assigned rigidity until a best fit is obtained.

As a final refinement to this analysis a study of the downstream detector acceptance will need to be completed. The detectors of the HISS facility were designed with a large aperature, and we expect that only for Helium and the lightest fragments of the lowest energy beams will significant aperature corrections be needed.

B. HISS ANALYSIS

The analysis of the HISS data not only involves developing detector calibrations but also the methodology and techniques for extracting relevant scientific information as efficiently as possible. This methology and the up-to-date calibrations are described here along with a summary of the current results.

1. Analysis Methodology and Technique

The HISS E938H experiment (Figure 15) is designed to identify fragment isotopes using the rigidity-velocity-charge technique and the isotope mass (A) can be determined from

$$A = \frac{R \cdot Z}{\beta \cdot \gamma \cdot m_0 c^2} \tag{6}$$

where R is the particle rigidity, Z is the charge, the measured velocity determines $\beta\gamma$ and m_0c^2 is the energy equivalent of an atomic mass unit (amu). In this experiment there are three measures of the particle charge. Two of these are immediately downstream of the target using a high energy resolution solid state detector (SSD) and a fast scintillator (BV). The final charge measurement is downstream of all of the apparatus mass and uses the scintillator slats in the TOF wall. Velocity is determined for the lower energy measurement (less than ~1 GeV/nucleon depending upon projectile mass) by the time-of-flight between the upstream trigger scintillators, S1 and S2, and the TOF wall. For higher energy (~1.6 GeV/nucleon) a total internal reflection cherenkov detector (VMD) was used.

The particle rigidity is determined by measuring the fragment trajectory as it curves through the HISS dipole field. This requires multiple position measurements along the trajectory with at least one vector on either side of the magnet. The upstream MICKEY position sensing detectors are used to obtain the incoming beam vector that when projected to the target (TGT) provides the initial point of the fragment trajectory. Downstream of the dipole the 15 plane drift chamber (DC) provides the outgoing fragment trajectory. Finally the Fiber Scintillator Hodoscope (FISH), provides a redundant point upstream of the HISS dipole to increase resolution.

The particle rigidity is determined from the trajectory measurements by an iterative procedure that begins with an initial guess of the particle rigidity and incoming vector. A full trajectory is then computed by a stepwise integration of the equations of motion of the particle through the measured HISS field map. This trajectory is compared to the measured one, the initial vector and rigidity is adjusted and the process is iterated until the difference between the calculated and measured trajectory is minimized.

This procedure for obtaining the absolute particle rigidity is complex, requires all position sensing detectors to be fully calibrated, a detailed field map and is computationally intense. While previous HISS experiments developed codes for determining rigidity, the expertise for modifying and operating these codes was not available to our effort. Therefore, a significant amount of man-effort is needed for either adapting old codes to the E938H experiment or re-coding such programs from scratch. With our limited resources over the last few years focusing on determining the absolute rigidity would have significantly delayed obtaining any scientific results from the experiment. Thus, it was decided to delay developing the full rigidity calculation and instead to adopt an alternative approach to the data analysis where the necessary detector calibrations would be completed, but intermediate scientific results would also be obtained.

The first step in this alternative approach was to concentrate on the detector systems upstream of the HISS magnet. These detectors are shown for the April, 1991 configuration in Figure 17 and are sufficient for determining the charge-changing total and partial cross sections. Shown in the figure are the wire chambers (WC5, WC6, WC7) and the final B42 beamline quadropole focusing magnet (Q3C) which are used for tuning the beam. The detectors upstream of the liquid hydrogen target (TGT) are used to characterize the incoming beam and form the event trigger. These consist of two counting scintillators paddles, S1 and S2, two veto scintillator paddles, V1 and V2, with holes at their centers (1 cm diameter for V1 and 2.54 cm diameter for V2), and an adjustable aperture veto (AV) composed of four scintillator paddles (U, D, E, W) which are independently counted in the datastream and which are positioned to form a 1.5" to 2" square hole centered on the beam. By examining ratios of the rates in these four paddles (i.e. U/D or E/W) beam movement can be continuously monitored during data taking. The counting and veto scintillators (S1, S2, V1 and V2) are viewed by photomultiplier tubes on each end, to provide redundant measurements and improve detector uniformity. Scintillators S1 and V1 are placed at a beam focus 10 m upstream of the target where S1 functions as the start detector for the TOF system and V1 is incorporated to flag any beam particles or fragments outside the acceptable phase space for the system. The entrance aperture to the target is defined by V2 and two discriminator levels are adjusted on S2 to be below (S2L) and above (S2H) the beam signal. The trigger also incorporates an Up Dating One Shot (UDOS) fired by the coincidence of S1 * V1 which provides lock out protection for the system to ensure that no beam particle or fragment preceded a valid trigger within a 300 ns time period. Finally for the April, 1991 runs a veto scintillator, V4, with a 4.5 cm diameter hole was placed downstream of the target to assure that events pass through the fully active region of the silicon solid state detector (SSD). Thus for the April, 1991 run period the main trigger for the experiment is

$$\mathrm{BEAM}=(\mathrm{S1E}*\mathrm{S1W})*(\overline{\mathrm{V1E}+\mathrm{V1W}})*(\overline{\mathrm{UDEW}})*(\mathrm{S2L}*\overline{\mathrm{S2H}})*(\overline{\mathrm{V2E}+\mathrm{V2W}})*\overline{\mathrm{V4}}*\overline{\mathrm{UDOS}} \quad (7)$$

Finally the beam trajectory is determined by the position sensing "MICKEY" detectors M1 and M2. Each of these detectors provides an X,Y pair which can be fit to provide the beam vector. The beam profile can then be projected onto the target face to determine the amount of liquid hydrogen traversed by the event or further downstream to assist in studying the acceptance of the V4 aperture.

The two detectors just downstream of the target (SSD & BV) provide redundant measurements of the fragment charge. A cross plot of the raw signal of these two detectors is shown in the top panel of Figure 18 for the 400 MeV/nucleon ^{32}S beam. The beam spot is readily

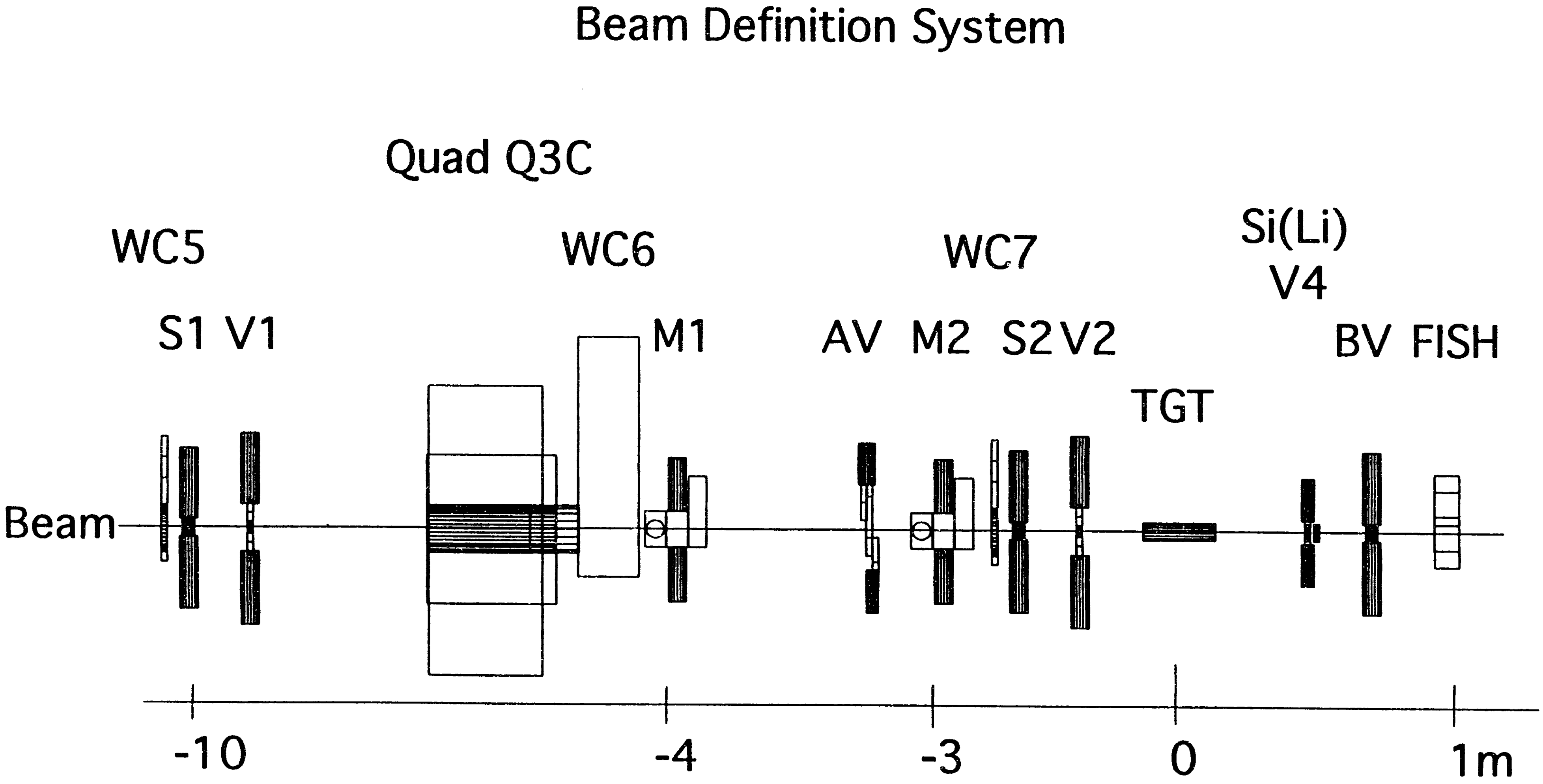

Figure 17. Schematic of the E938H detectors upstream of the HISS magnet.

apparent as well as those for fragments from Ne to P. The bottom panel of the figure also shows the effects of introducing the Beam Veto into the trigger logic. Here a discriminator level is set on the BV detector between the beam and first fragment peaks (i.e. at ADC value ~680 on the figure) so that beam particles depositing energy in BV above this threshold will be vetoed. The trigger in this case is then defined as

$$\mathrm{INT} = \mathrm{BEAM}^{*}\,(\overline{\mathrm{BV}}). \tag{8}$$

Using the INT (interaction) trigger, as shown on the bottom panel of Figure 18, has the effect of enhancing the number of fragments collected during a data taking run, but the collection efficiency of the fragments near the threshold must be carefully studied. Therefore, runs with and without the Beam Veto in the trigger were performed during data taking.

The resolution of the upstream charge is indicated in Figure 19 which is a histogram of the calibrated charge and cleaned up by requiring a consistent charge between the SSD, BV and TOF wall. Very clear charge peaks are evident and the measured resolution is better than 0.2 charge units. From similar histograms, of strickly the SSD, BV charge, the number of surviving beam (N_{Beam}) and fragment (N_Z) particles are determined using multiple gaussian fits of the peaks relative to the total number of valid incoming beam (N_{Total}) projectiles. These numbers were also determined for target out data obtained by using a "dummy" target. The charge changing total cross section $\sigma(\Delta Z \geq 1)$ then is defined as the cross sections for removing at least one charge from the beam particles and can be obtained from

$$\sigma(\Delta Z \geq 1) = \ln \left[\frac{\frac{N_{BEAM}}{N_{TOTAL}}\,(\text{Target out})}{\frac{N_{BEAM}}{N_{TOTAL}}\,(\text{Target in})} \right] \cdot \frac{A_H}{N_A \cdot t \cdot \rho 10^{-27}} (\text{mb}), \tag{9}$$

and the charge changing elemental production cross sections, $\sigma(Z_f)$, of a beam fragmenting to a particular charge (Z_f) are obtained using the "thin target" approximation from

$$\sigma(Z_f) = \left[\left(\frac{N_Z}{N_{TOTAL}}\right) (\text{Target In}) - \left(\frac{N_Z}{N_{TOTAL}}\right) (\text{Target Out}) \right] \cdot \frac{A_H}{N_A \cdot t \cdot \rho 10^{-27}} (\text{mb}). \tag{10}$$

In both Eq. 9 and 10, $A_H = 1.00797$ is the atomic weight of hydrogen, $N_A = 6.022 \times 10^{23}$ is the Avogadro's number, t is the target thickness (~3 cm) and ρ is the hydrogen density (~0.070 g/cm^3). These charge changing cross sections are scientifically interesting in their own right and can be published independently of the isotopic analysis. Currently, the calibration of the upstream detectors is completed, cross section values are available for all beams except He and a publication on these results is currently in preparation.

In parallel to the upstream analysis, effort has also been devoted to developing a simplified technique for obtaining isotopic cross sections and most of this development effort has used the 400 MeV/nucleon ^{32}S data. The technique approximates the HISS dipole field as having a constant bending power and the steps to obtain isotopic separation is illustrated in the four panels of Figure 20. First a fragment element is selected using a data cut on the upstream versus downstream chage cross plot (panel A). Then a rough rigidity measurement can be obtained from the horizontal (x) position and the angle (θ_x) measurement from the drift chamber and a plot of θ_x versus x for the selected silicon fragments is shown in panel B. Clumps of points corresponding to different Si isotopes can be seen. Although this approximation will resolve isotopes for fragments close to the beam charge (Z_b), the rigidity distribution width increases rapidly with increasing mass loss obscuring individual isotopes below Z_b-3.

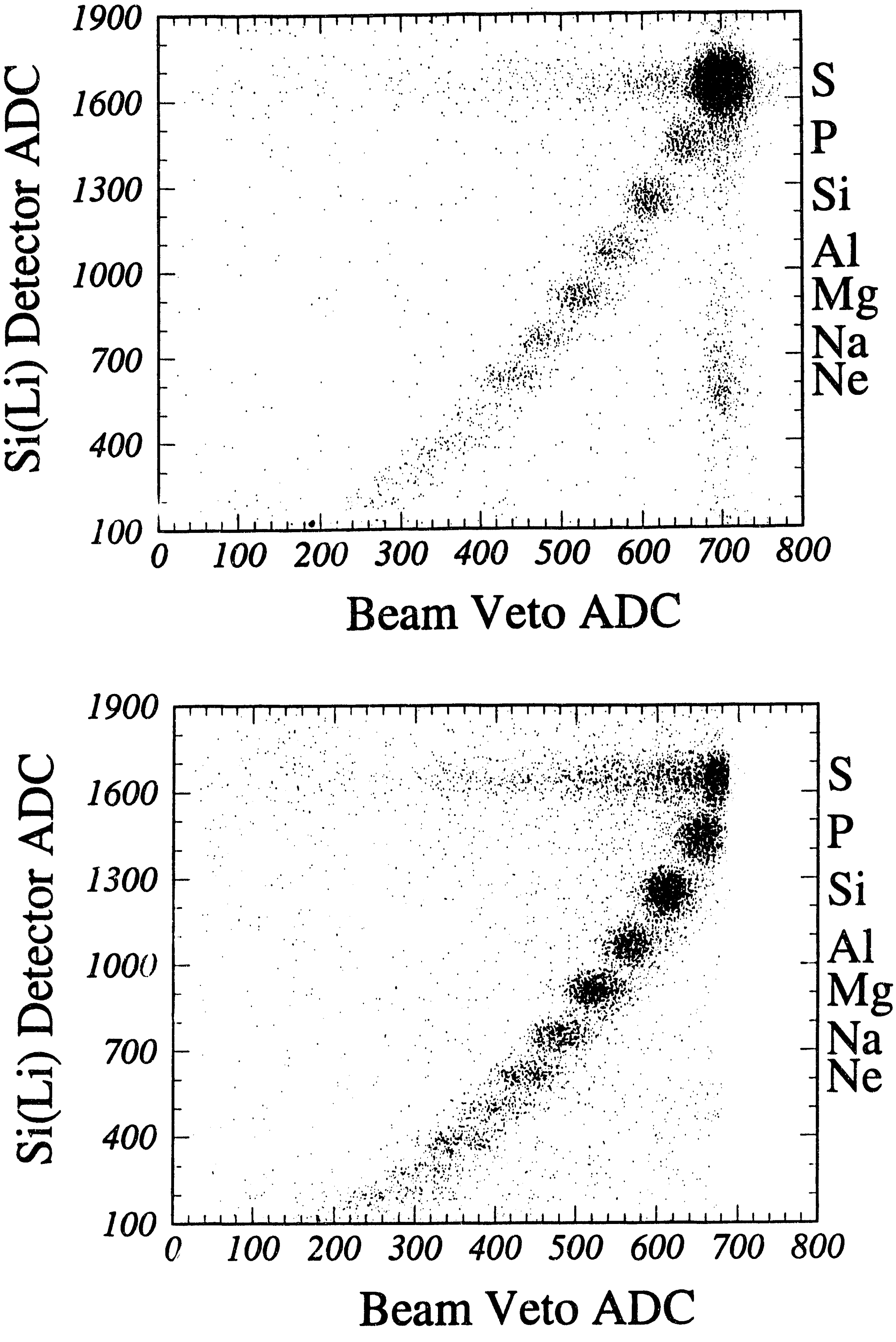

Figure 18. Scatter plot of raw SSD signal versus BV signal for the BEAM trigger (top panel) and for the INT trig (bottom panel).

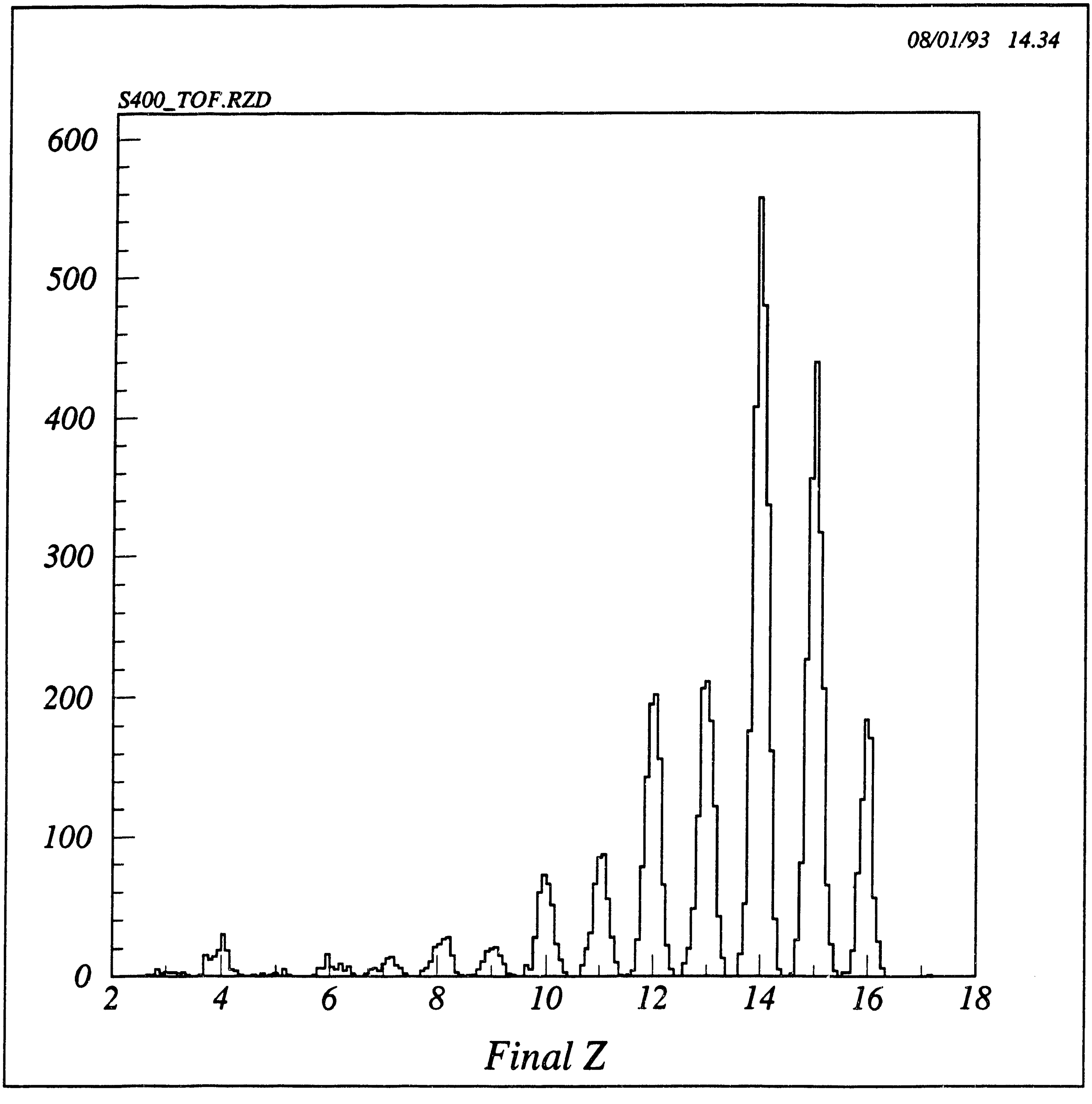

Figure 19. Charge resolution histogram for the 400 MeV/nucleon ^{32}S data.

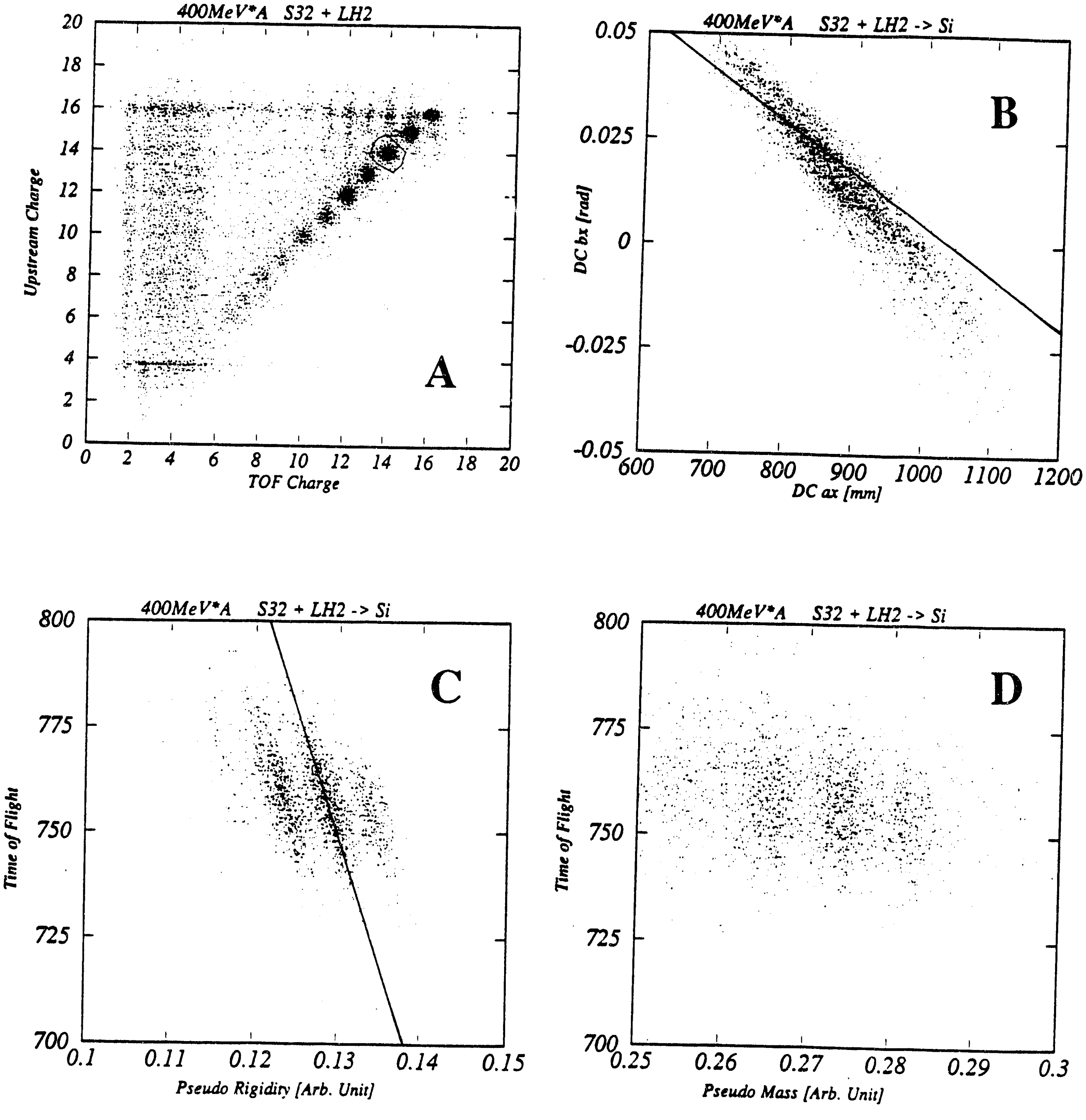

Figure 20. Illustrating the "pseudo-rigidity" method for obtaining isotope resolution.

To resolve isotopes with higher mass loss, we define a relative or "pseudo-rigidity" and incorporate the velocity information obtained from the time-or-flight measurement of the TOF wall. The "pseudo-rigidity" is determined from

$$R_p = x + K \cdot \theta_x , \qquad (11)$$

where K is obtained by fitting a line through an isotope clump (line on panel B). The calibrated time of flight (t) can then be plotted against R_p as shown in panel C and a clearly increased isotope resolution over the x, θ_x plot can be seen. From the t vs. R_p plot the mass line can be fit in a fashion analogous to the pseudo-rigidity as:

$$M_p = R_p + K' \cdot t , \qquad (12)$$

where K' is the slope of the fitted line. Panel D in the figure shows the scatter plot with respect to this derived mass.

This technique allows us to resolve fragment isotopes over the charge range from Z_b down to ~$Z_b/2$ as shown in Figure 21, where fragment isotope peaks from N (Z=7) to P (Z = 15) are resolved to a level of $\sigma<0.2$ amu. From such histograms the isotopic yields ($N_{Z,A}$) can be determined for both Target In and Target Out, and the isotopic cross section $\sigma(Z,A)$, computed in a manner similar to the charge changing elemental cross sections:

$$\sigma(Z,A) = \left[\left(\frac{N_{Z,A}}{N_{TOTAL}}\right) (\text{Target In}) - \left(\frac{N_{Z,A}}{N_{TOTAL}}\right) (\text{Target Out}) \right] \cdot \frac{A_H}{N_A \cdot t \cdot \rho 10^{-27}} (\text{mb}), \qquad (13)$$

where the other parameters are the same as in equations (9) and (10). From preliminary investigations we expect the pseudo-rigidity technique to yield good isotopic resolution for beams as heavy as ^{40}Ca, or possibly ^{52}Cr. The isotopic analysis of the Fe and Ni beams, however, will likely require determining the absolute rigidity.

The HISS analysis approach is summarized and graphically illustrated in Figure 22 which shows the two primary analysis tracks, upstream and downstream, proceeding more or less independently but eventually merging to yield the isotopic cross sections. Essentially all major components in the upstream analysis (data splitting, diagnostic plotting, beam vector calibration, "good" beam characterization, BV/SSD charge calibration, target density and thickness calibration, and the upstream fragment acceptance calculations) are complete leading to a finalized set of charge-changing cross sections.

In the meantime, work on the Downstream analysis is continuing. The first step in this operation is to provide the space-time calibration for the drift chamber (DC). To optimize the DC trajectory resolution, the wire plane voltage settings must be adjusted for each beam and, thus, an independent calibration is necessary for each run. Currently, a little over half of these beam specific calibrations have been completed. Level 1 processing then uses these calibrations to convert the raw DC signal to a fragment trajectory. All the April, 1990 data have been processed through Level 1 and processing for the 1991 data is in progress. Also incorporated in Level 1 is the pointing vector between the DC and TOF wall. This allows the DC trajectory projected to the TOF wall to accurately match "hit" scintillator slats and only depends upon the physical placement and orientation of the two detectors which do not change during a data taking period. The DC-TOF pointing has been determined for both the 1990 & 1991 datasets.

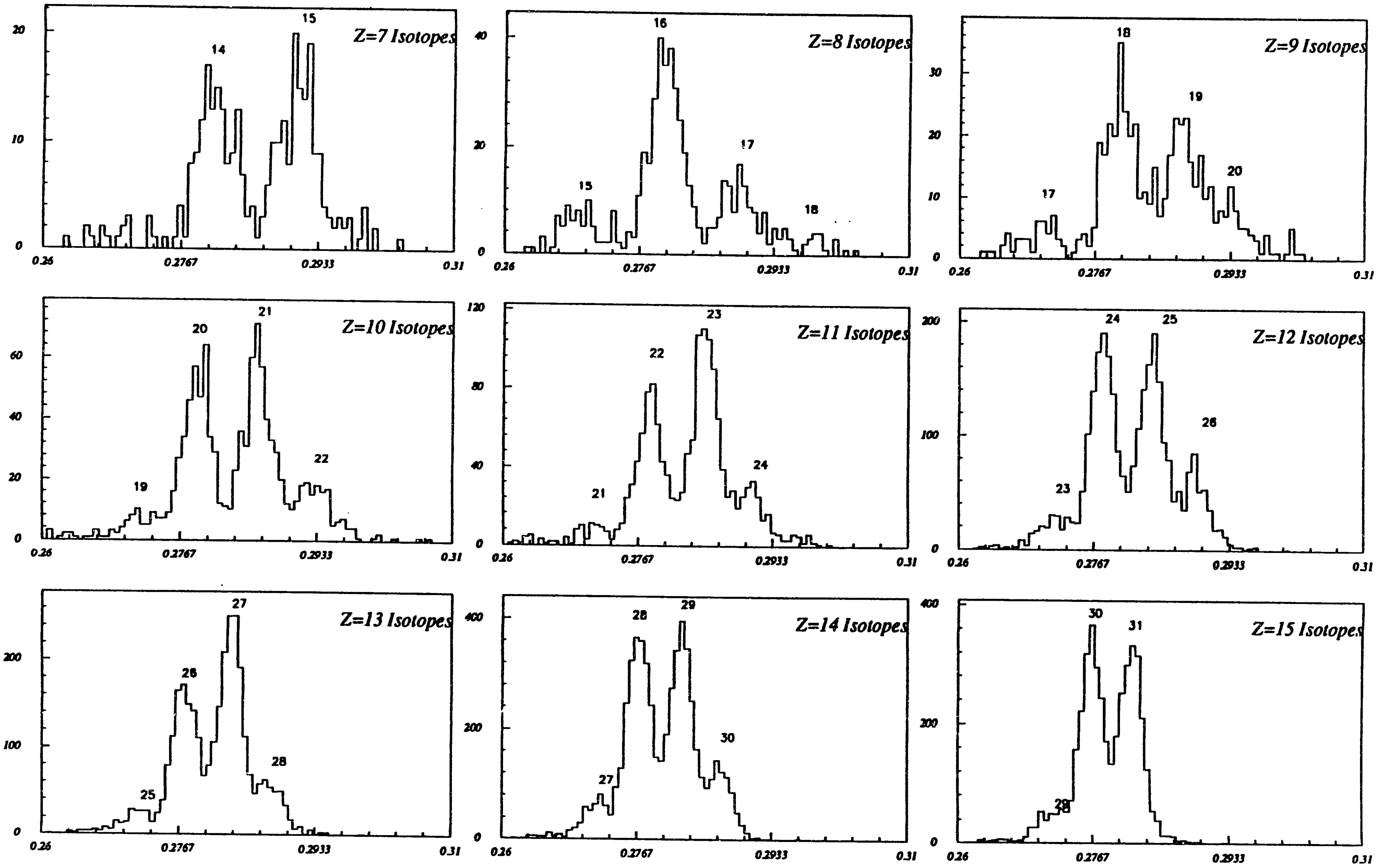

Figure 21. **Pseudo-mass histograms for 9 elements from fragmentation of 400*A MeV ^{32}S + H. The mass resolution is $\partial A \sim 0.2$ u HWHM.**

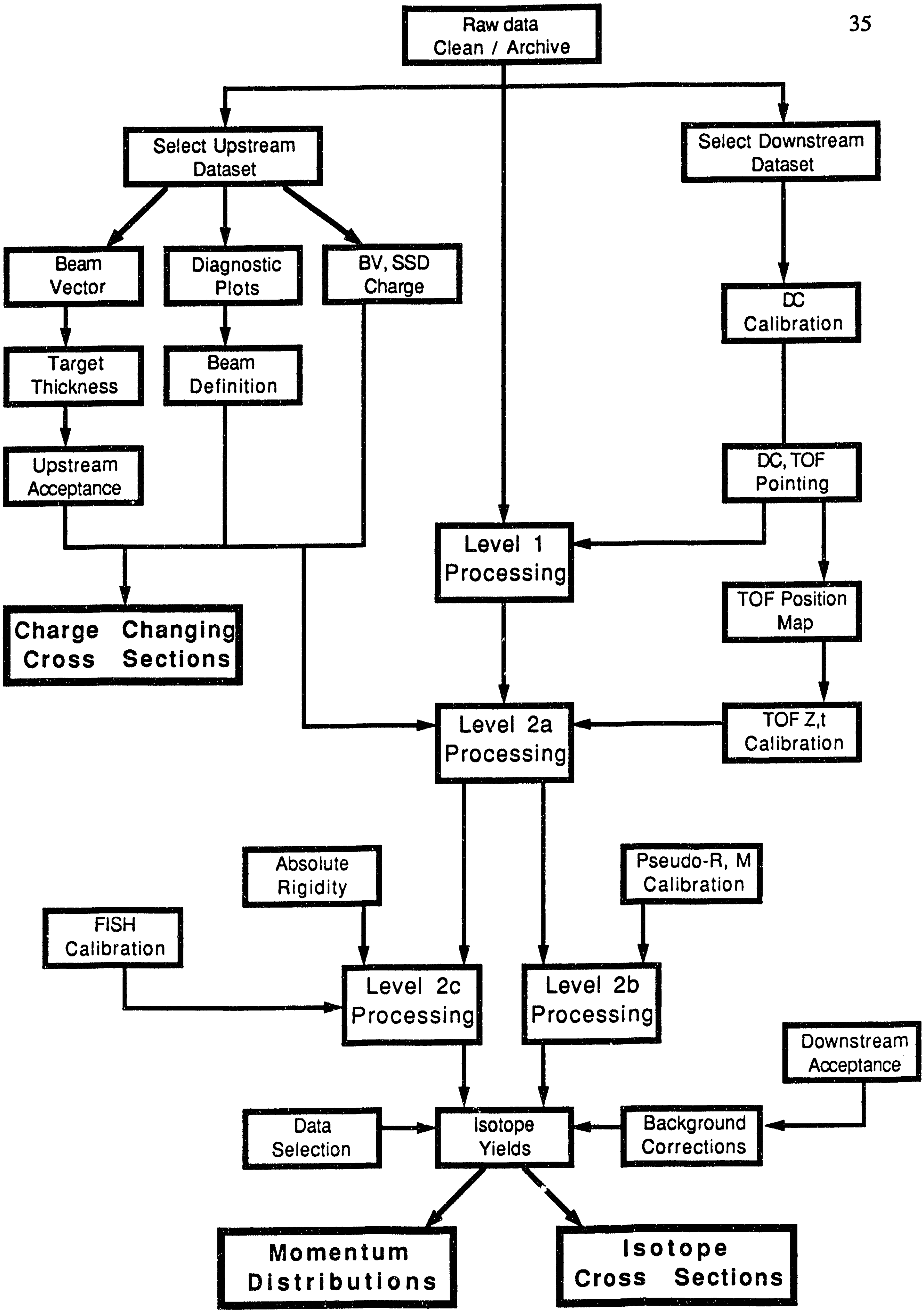

Figure 22. Flow chart of the HISS analysis approach.

Prior to our first data taking run in 1990 it was discovered that the individual scintillator slats making up the TOF wall had suffered from some surface crazing. This affected the linearity of the light attenuation as viewed by the photomultiplier tubes on each end of a slat. This had the effect of severely degrading the charge and time resolution of the TOF wall, but with an attenuation map tailored to each of the ~100 slats nearly full resolution could be restored. These attenuation maps were completed for the 1990 run period as a necessary prelude to determining the beam specific charge and time calibration. Recently, an analysis of the 1991 data has shown that the surface crazing has worsened and the attenuation maps must be redone for this data set. This work is now in progress.

The next analysis step is to incorporate all the detector specific calibrations for both upstream and downstream systems into the Level 2a processing. This dataset is then used to determine the pseudo-rigidity/isotope mass calibrations and the data is reprocessed to Level 2b. At this high level all of the detector information is presented in "science" units (i.e. trajectory vectors, charge, mass time). Only recently has the development of the Level 2a, 2b algorithms and coding been completed, and the software is now undergoing testing. Once the software is verified we will begin Level 2 production processing with the ^{32}S beams as the TOF calibrations already exist for these data and continue as more beam specific calibrations become available.

With the Level 2b dataset, obtaining the isotopic cross sections should involve (1) cleaning the data of events which interacted between the target and TOF wall, (2) determining correction factors for the clean-up cuts, (3) fitting the mass histograms and determining the isotopic yields, (4) obtaining the beam normalization, and (5) performing the target in/target out subtraction. In parallel to this effort is a study of the DC and TOF angular acceptance in order to determine correction factors as a function of beam and fragment charge, mass and energy for otherwise good events falling outside of the active detector regions. These correction factors are folded into the normalized, background subtracted isotopic yields and divided by the beam specific target thickness to obtained the mass changing isotopic cross sections.

Finally, the effort to develop an absolute rigidity calibration is now underway and will involve developing algorithms and coding specific to the E938H experiment along with incorporating a real field map of the HISS dipole. Once this software is completed and tested we will reprocess the Level 2a data to Level 2c replacing the pseudo-rigidity with the absolute rigidity. This processing will also need to incorporate calibrations of the FISH detector. The Level 2c data will then be used to obtain isotopic cross sections for the Fe and Ni beam as well as beginning a study of the fragment momentum distributions.

2. Detector Calibrations

Much of the HISS analysis effort over the last year has been devoted to developing the calibration algorithms and parameter files necessary to convert raw signals to "science" units. This subsection presents details of these calibrations for each of the major detectors or subsystems in the HISS experiment.

a. The Upstream Vector & Beam Profile

The upstream beam position sensing detectors are used to establish the beam vector and project the beam profile onto any upstream detector. This is important for detecting any beam movement during a run, for deriving the target interaction thickness, for evaluating the apparatus acceptance and for establishing the upstream trajectory constraint when determining the fragment absolute rigidity. All of these operations affect the quality of scientific results eventually resulting from E938H and it is critical to obtain an accurate calibration of these detectors.

While several different versions of these position sensing detectors (PLUTO, GOOFY, MICKEY) were used during the 1990 and 1991 run periods they all operated under the same basic principle as illustrated in Figure 23. In a light-tight box a thin (~0.5 mm) rectangular scintillator is placed at a 45° angle between two photomultiplier tubes (PMT). As a beam particle passes through the scintillator light is radiated at all angles. But only the light within the PMT field of view will be collected. As the field of view opening angle depends upon where the particle penetrates the scintillator the ratio of the signals from the two PMT will be directly related to this position. In the figure the right band PMT would have the larger signal. One such device provides information on only one coordinate. So to obtain an x,y position two detectors must be oriented at right angles and both mounted orthrogomal to the beam. Also incorporated with these detectors are grids of thin (~1 mm) scintillating optical fibers that are used for the detector calibration.

The advantage of such detectors is that they are simple, relatively easy and inexpensive to construct, and provide a fast signal as well as position information. The disadvantage is their relatively poor position resolution (~1.5 mm - ~3 mm) and their non-linear response. As it is actually an accurate beam vector that is required, spacing two such detectors as far apart as possible can reduce this uncertainty. In the E938H experiment a detector spacing of about 1 m was used. The non-linear response, however, requires a significant amount of man-effort to develop the beam specific calibrations. Prior to each data taking run a series of calibration files were generated where only events which trigger the calibration fiber grid are collected. The raw data from such a fiber calibration file are shown in Figure 24 where the natural log of the ratio of the vertical tubes is plotted against the same formula for the horizontal tubes. The grid is actually rectangular with two diagonal fibers to provide orientation. The calibration proceeds by locating and identifying the intersections of all visible fibers and entering their coordinates, in both logarithm of ADC space and real, physical space, in a calibration parameter file. This file must contain sufficient information to cover the full face of the detector, so the coordinates of any "invisible" intersections must be extrapolated from the known information. The calibration file is used with a 2-dimensional interpolation algorithm to generate physical space x,y coordinates from the raw data. In general, several iterations of the calibration parameter file are necessary before the fiber grid plot is uniformly populated and dimensionally correct. Finally, any drifts or fluctuations of the PMT voltages over the course of a data run must be taken into account. This is done by examining each data file, selecting events which trigger the calibration grid and looking for relative offsets in the fiber grid pattern. These offsets are then incorporated into the calibration parameter file. The fiber grid data for a completed calibration is shown in Figure 25 and in Figure 26 histograms of two vertical fibers (left panel) and two horizontal fibers (right panel) are shown as well. The gaussian fits to these distributions imply a position resolution in both the x and y direction of $\sigma \approx 1.5$ mm.

With calibrated position sensing detectors the beam vectoring can now be determined by incorporating the detector position and orientation information obtained from a survey of the apparatus following the completion of the run. However, even with survey information there is an uncertainty in the exact position of the detectors and for the April, 1990 run one of the position detectors (PLUTO) was removed and not surveyed. Thus it was necessary to determine the precise detector location by requiring self consistency between the beam vectoring, trigger vetos (hole scintillators) and the downstream beam vector determined from the drift chamber. For example, Figure 27 shows the beam profile of the 400 MeV/nucleon ^{58}Ni beam as seen by the Mickey 1 and Mickey 2 position detectors and projected downstream through the V2 trigger veto, the LH$_2$ target, teh SSD and BV detectors, the FISH fiber optic hodoscope and the V4 hole scintillator. Of these detectors both V2 and V4 are active elements in the trigger and with a correct beam vector all events should lie within the hole (circle on plot) and this is obviously not so. Similar information from the 1990 data was used to determine the position of PLUTO and adjust the position of the V2 hole until the projected beam profile yielded consistent results. In the case of Figure 27 the inconsistency is the result of a somewhat different cause. Here, the Mickey 2 vertical resolution is severely degraded, possibly due to magnetic field effects, and this causes the beam profile to be unrealistically elongated. Several examples of this problem were discovered and the adopted solution is to replace the Mickey 2 y measurement with the requirement that all beams pass through V2.

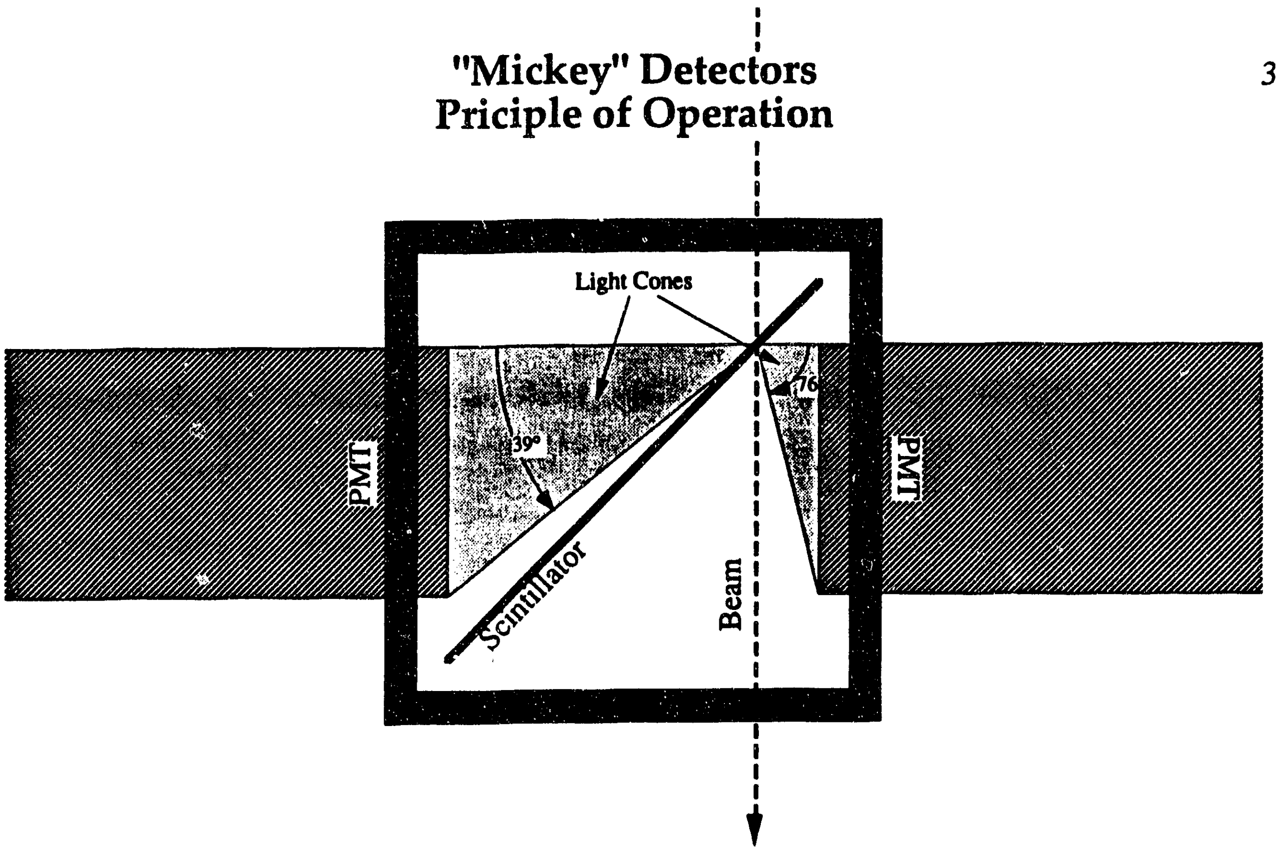

Figure 23. Schematic of a "Mickey" position sensing detector.

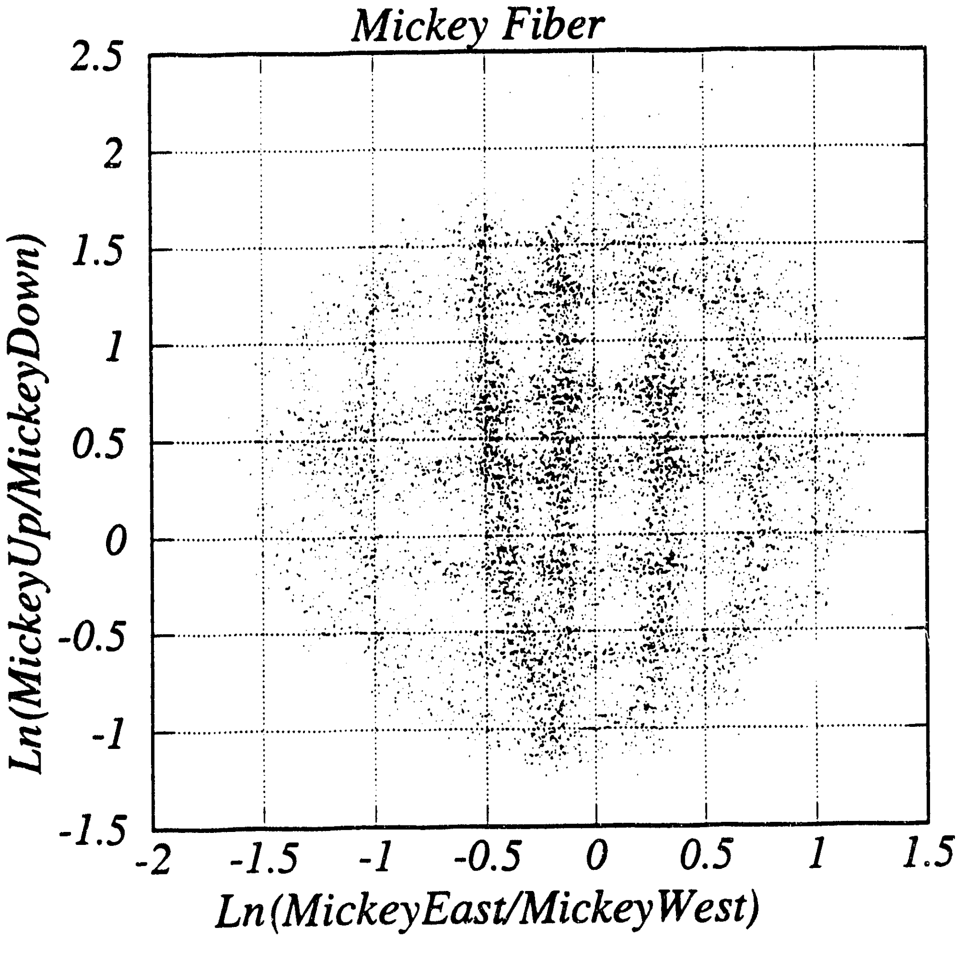

Figure 24. Raw Mickey calibration fiber grid data.

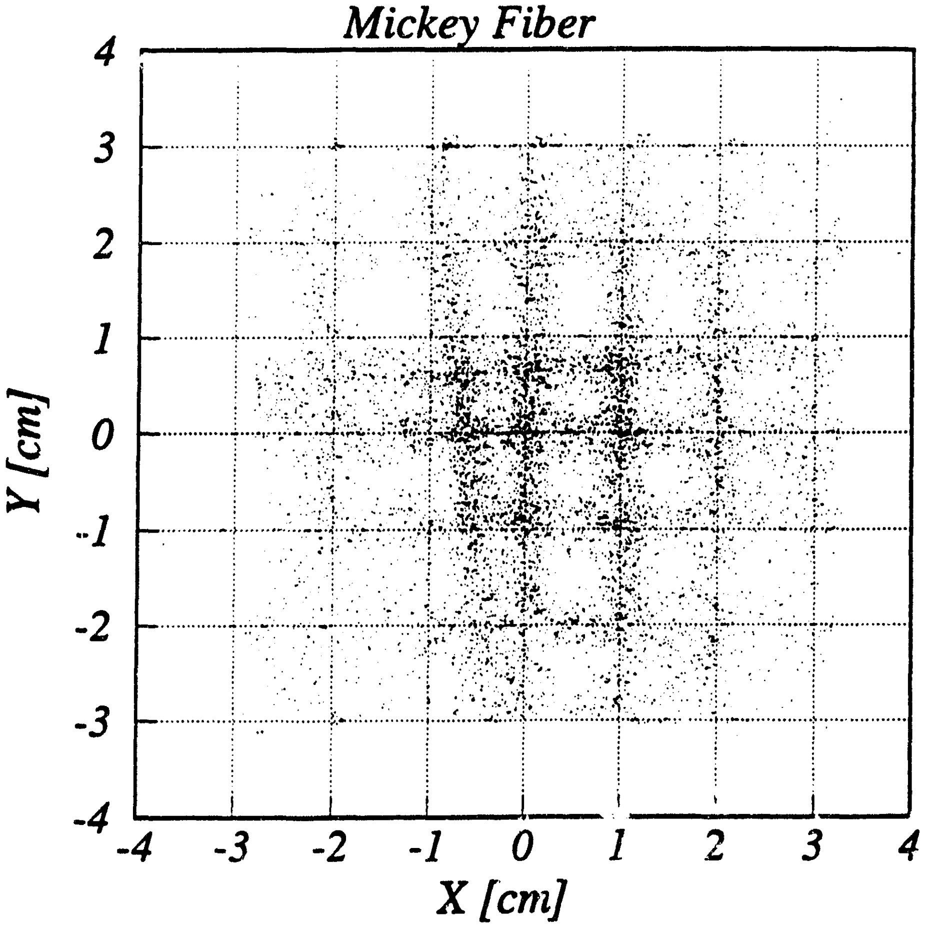

Figure 25. Calibrated position detector data showing the fiber grid.

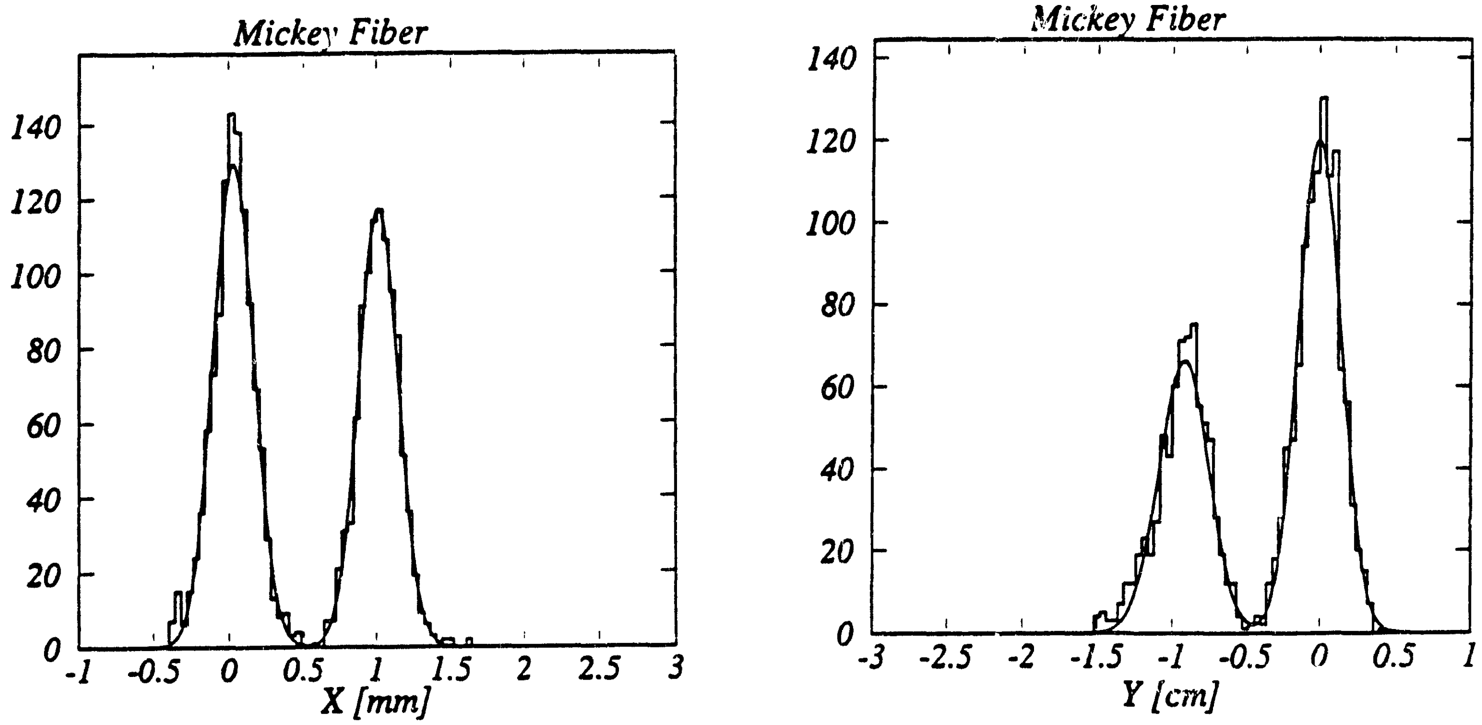

Figure 26. Position resolution histograms for two vertical fibers (left) and two horizontal fibers (right).

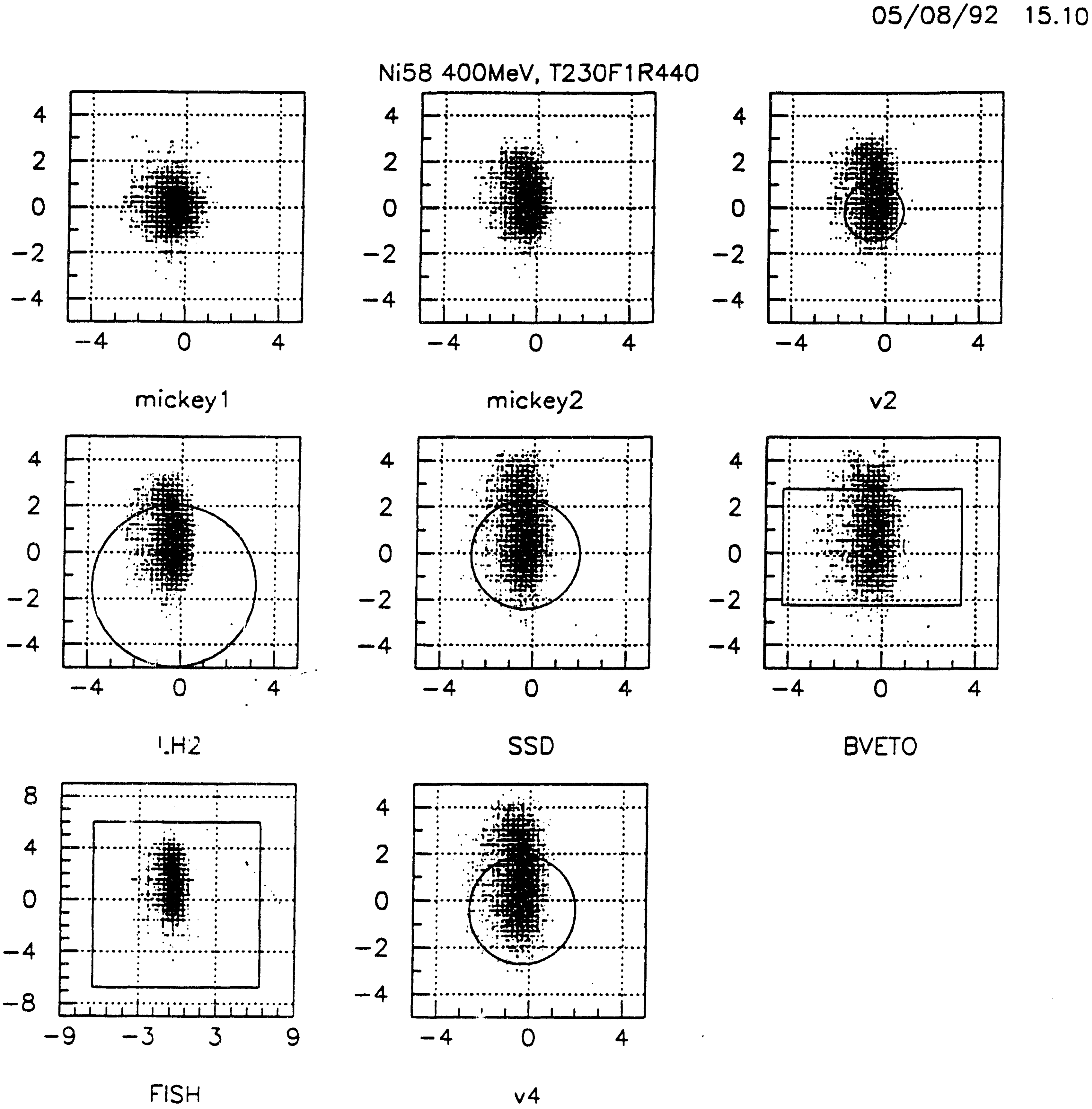

Figure 27. Beam profile projected to upstream detectors showing an inconsistancy with the event trigger.

Following this procedure the adopted positions of the upstream position detector, V2 hole and liquid hydrogen target are shown in the top panel of Figure 28 for the April, 1990 run configuration and in the bottom panel for the 1991 run. With these configurations the upstream vectoring resolution varies from 2 mrad to 4 mrad and the projected beam profile using the calibrations is shown in Figure 29. At this point the upstream beam position and vectoring calibration is considered to be final for both the 1990 and 1991 dataset, except for He beams which are near completion.

b. The Liquid Hydrogen Target

A key component in the E938H experiment is the liquid hydrogen (LH_2) target provided and operated by our French collaborators, A. Soutoul and O. Testard, from Saclay. While such a target can be difficult to handle and calibrate it allowed the experiment to avoid the CH_2 - C target subtraction method for obtaining projectile on H interaction cross sections. The LH_2 target provides a direct measurement of such interactions and reduces the amount of beam time required to obtain the same statistical uncertainty relative to the CH_2 - C subtraction by a factor of 2 or more.

A schematic of the target subsystem is shown as Figure 30 The target head contains approximately 1 liter of liquid hydrogen that is condensed directly onto a "long" (≈100 mm long) and a "short" (≈27 mm long) target vessel. All of the E938H data was collected with the 27 mm vessel to reduce multiple interactions and scattering in the target and allow the "thin-target" approximation to be used in the data analysis. These vessels are contained in a multi-walled stainless steel cylinder with 0.01 cm titanium windows and the condensed liquid is held at a working pressure of about 2 atm and a temperature of 19°K to 20°K by a temperature/pressure controlled feedback system. The cooling necessary for condensing and maintaing the liquid hydrogen is provided by a reservoir of liquid helium in a dewar mounted beneath the target head. In addition to the "active" head there is an exact mass equivalent dummy target that can be rotated into the beamline for "target out" measurements.

The most important parameter associated with the target is the actual thickness (in g/cm^2) of liquid hydrogen traversed by the beam, which must be derived for each beam by knowing the density (g/cm^3) of the liquid and the pathlength (cm) distribution of the beam through the target vessel. The target is designed to operate along the saturation curve for hydrogen and the LH_2 temperature changes slowly enough that the hydorgen never stays away from the equilibrium state where temperature is a function of pressure alone. Because of this one-to-one relationship between the temperature and pressure of the hydrogen in the target, we were able to derive the LH_2 density from the temperature. The saturation curve relating density to temperature is shown in Figure 31 along with the gross temperature range monitored during the April, 1990 and April, 1991 run times. In fact, the liquid temperature was very closely monitored so that any density variation could be identified. Such variations can be seen in Figure 32 for a several day period during the 1990 run time and in Figure 33 for a portion of the 1991 run. The top panel of the figures shows the monitor voltage while the bottom panel shows the corresponding calibrated temperature. At the very top of each figure is shown the time period when a particular beam was "active" and the "thick" portion of the line indicates when actual data taking occurred. The widest temperature variations occur during the initial "filling" period, but then stabilizes and shows little variation (1% for 1990, 0.2% for 1991) until the vessels are emptied. During the data taking runs the temperature variations are actually much smaller and are on the order of less than 0.2%. The exception to this is the 400 MeV/nucleon ^{40}Ca where the data was taken before the target was stable. However, with the continuous monitoring available the liquid density can be determined for each data file collected.

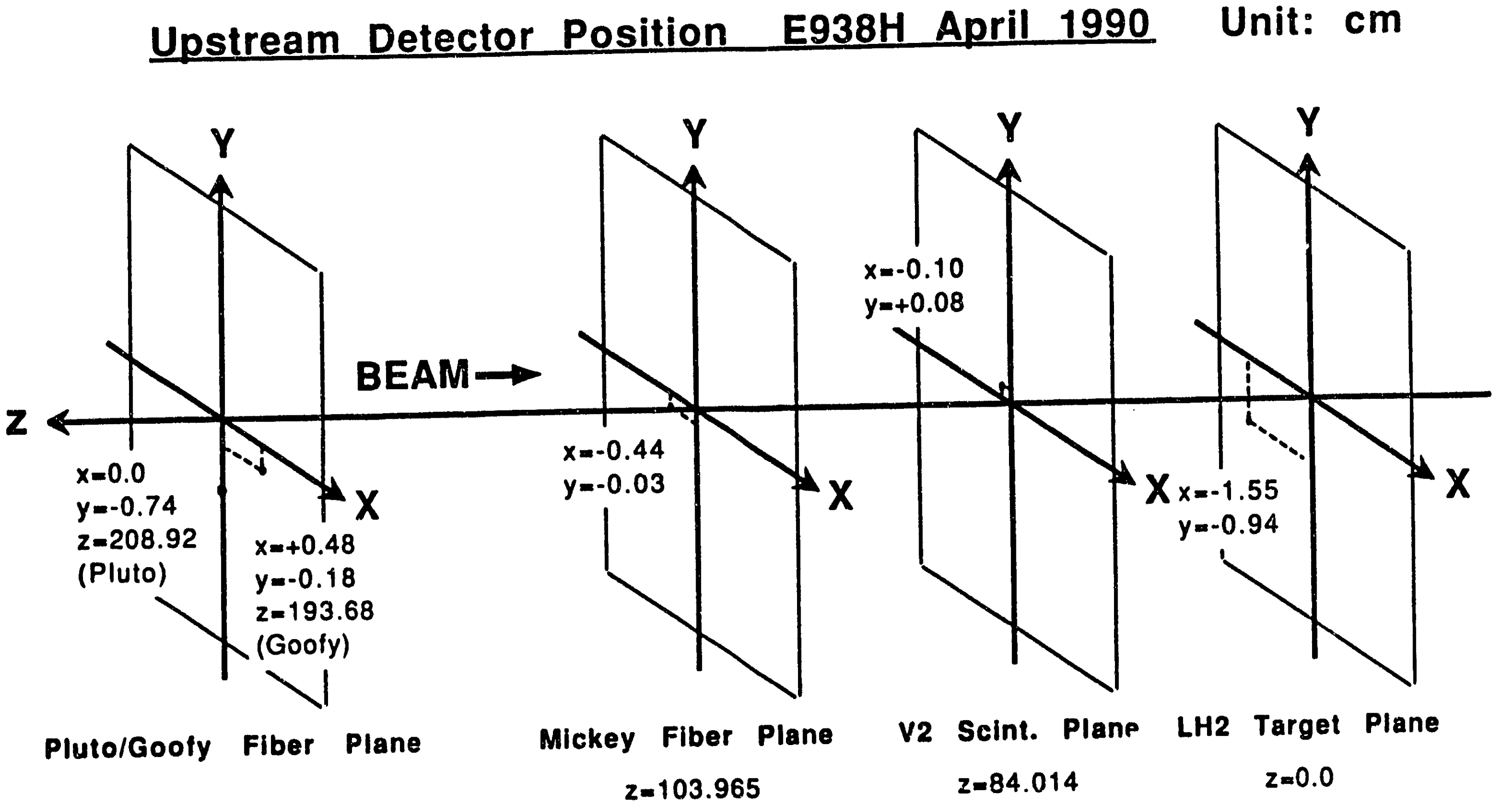

Upstream Detector Position E938H April 1990 Unit: cm

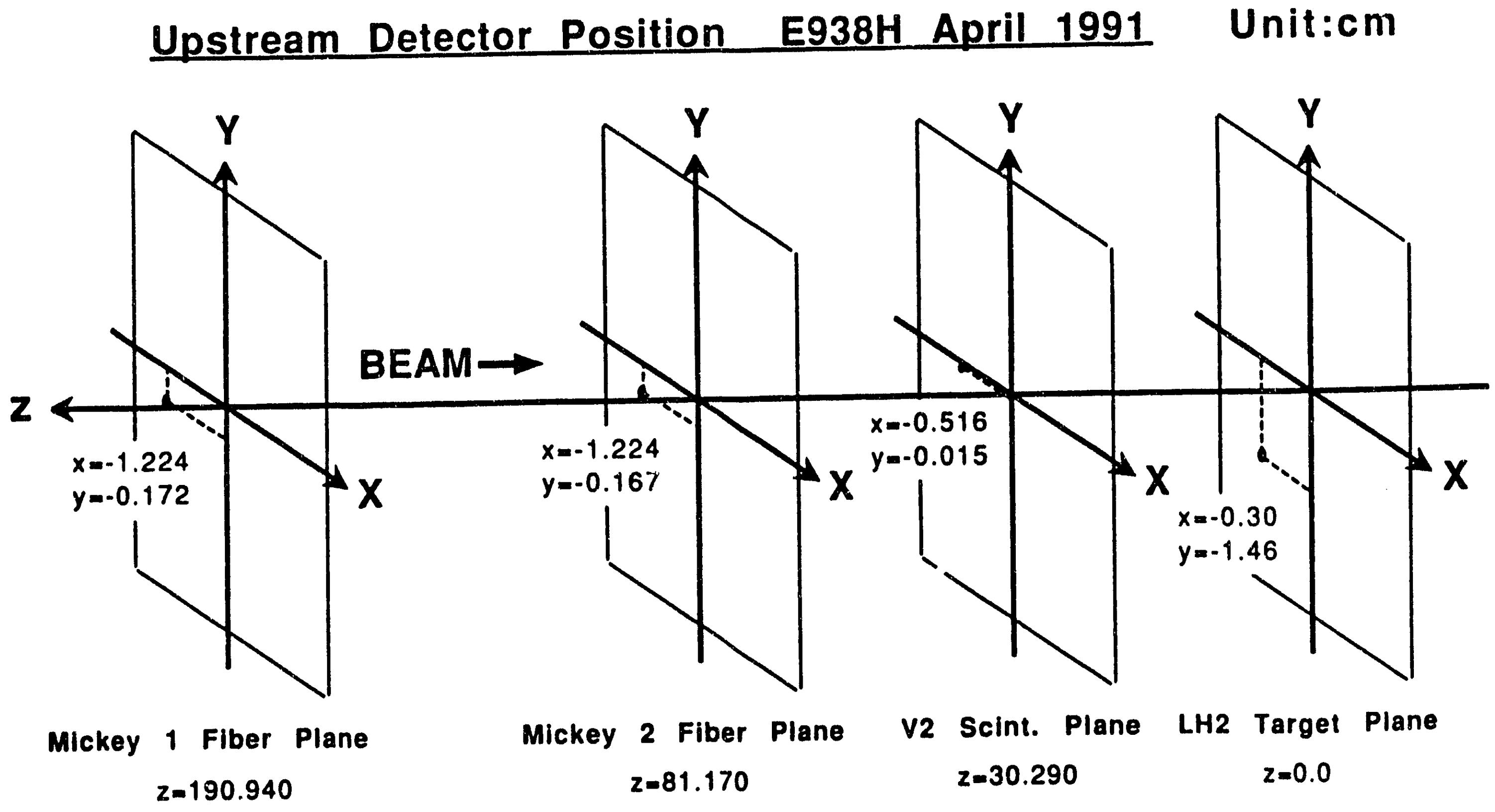

Upstream Detector Position E938H April 1991 Unit:cm

Figure 28. Critical upstream detector locations for the April, 1990 (top) and April, 1991 (bottom) run times.

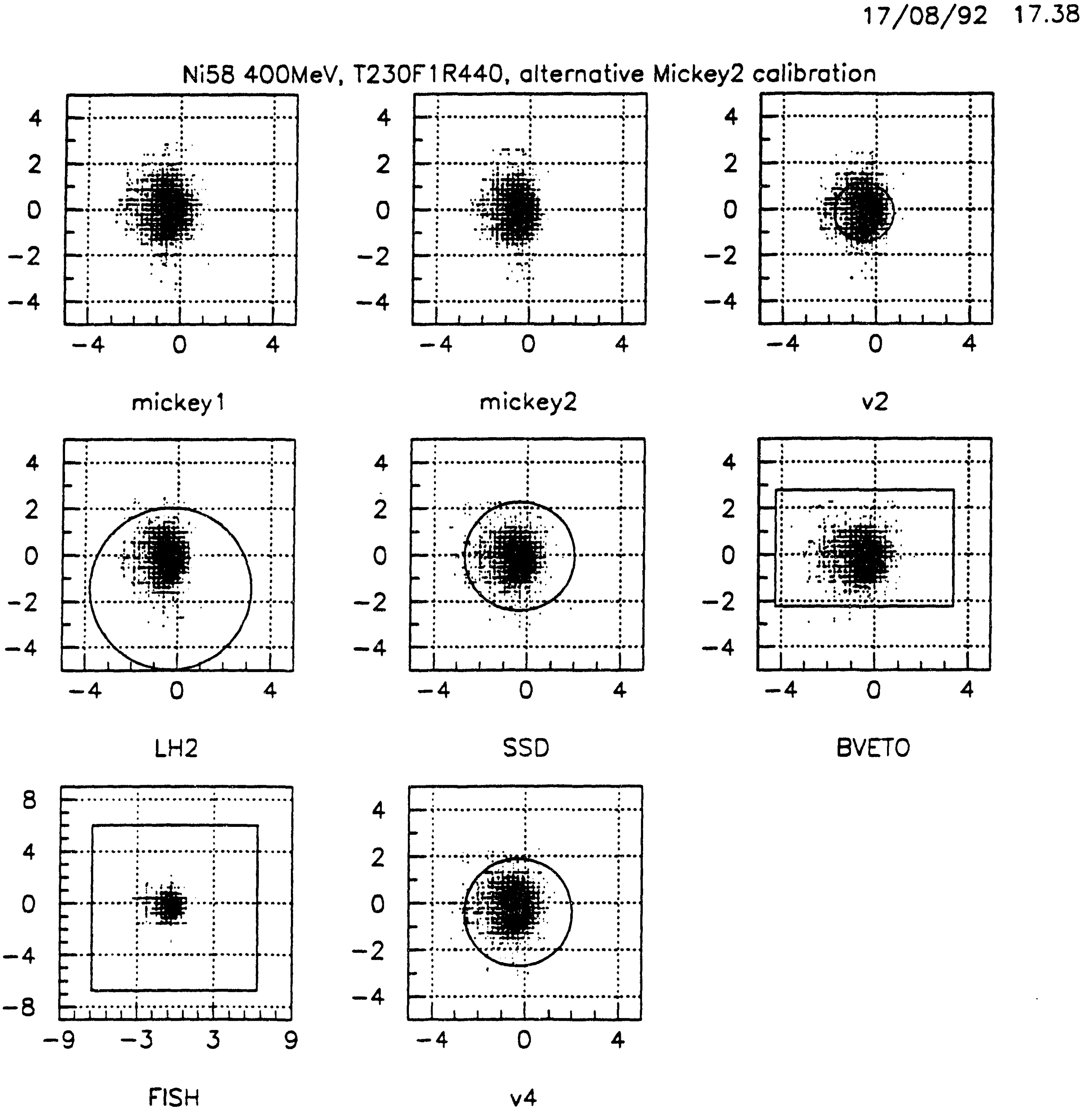

Figure 29. Beam profile projected to upstream detectors using the full vector calibration.

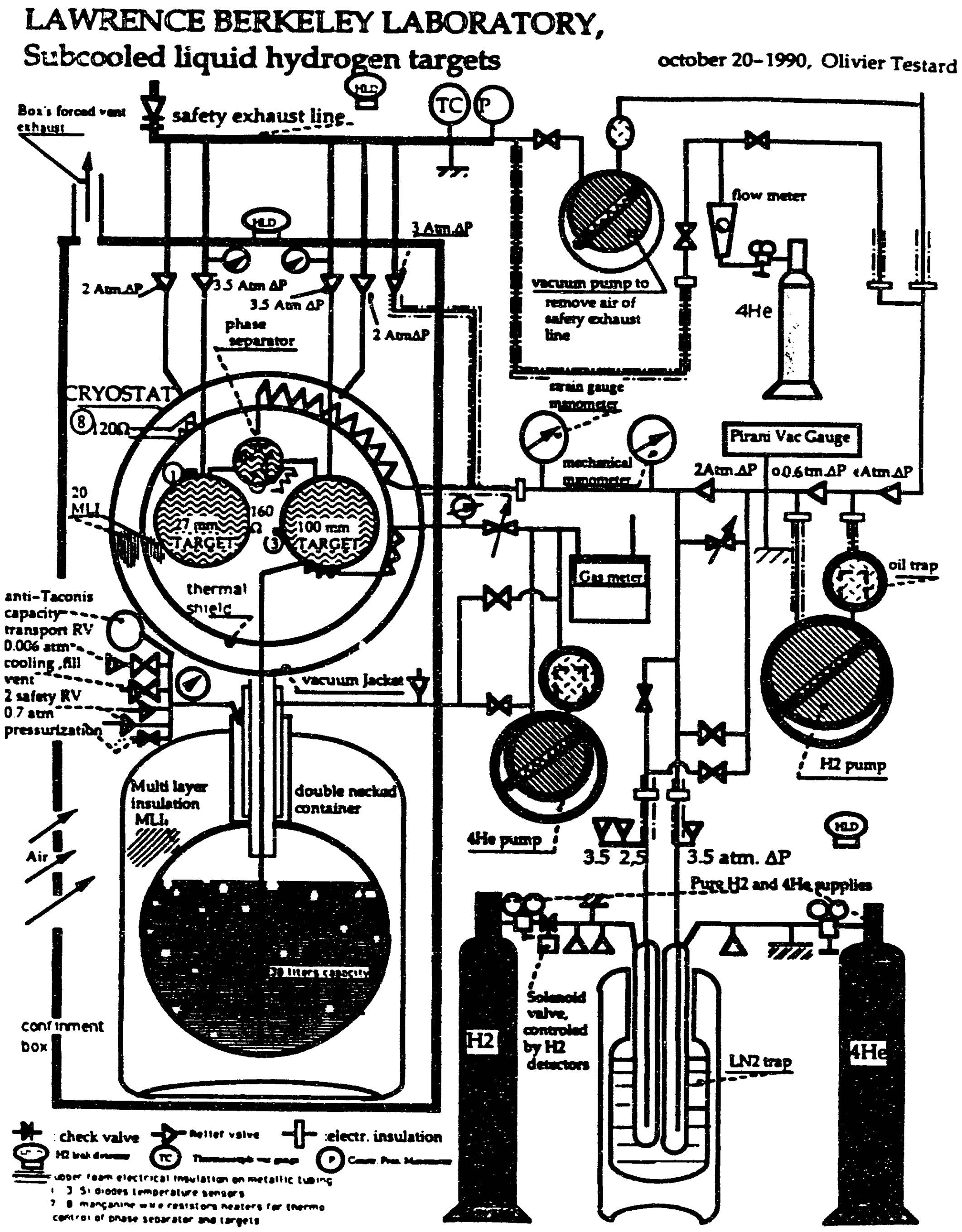

Figure 30. Schematic of the Liquid Hydrogen target system.

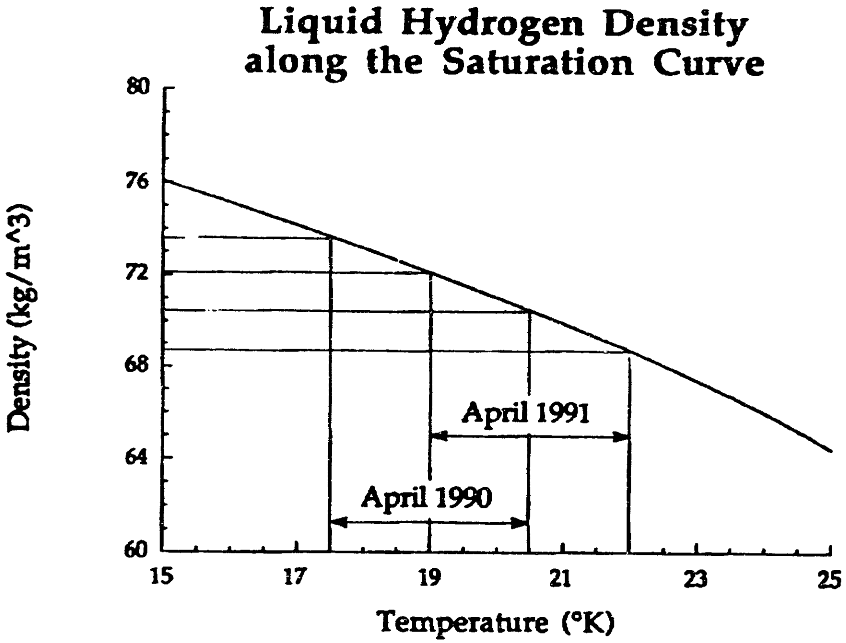

Figure 31. LH$_2$ density vs. temperature saturation curve.

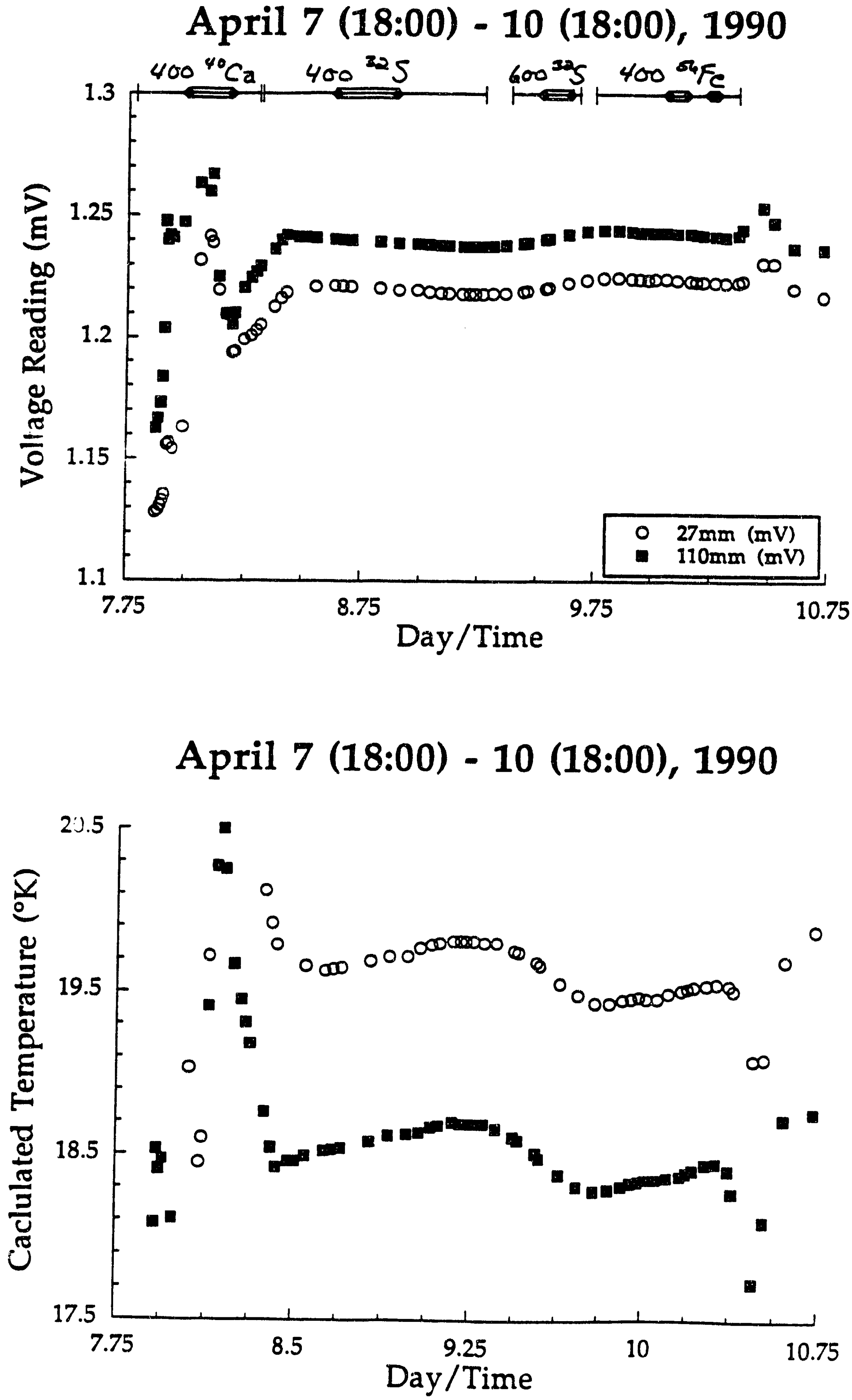

Figure 32. Target temperature monitor for a portion of the April, 1990 run time.

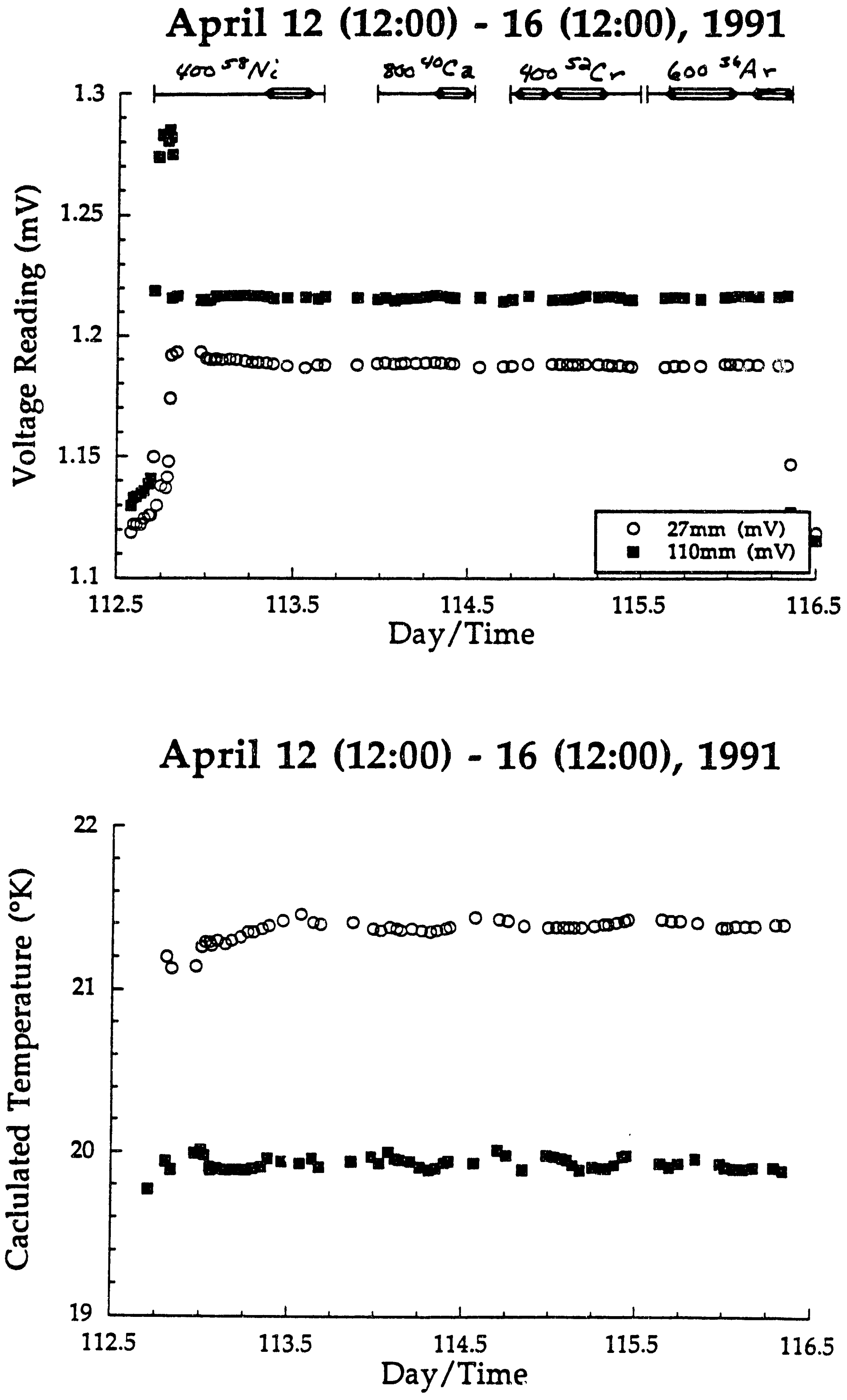

Figure 33. Target temperature monitor for a portion of the April, 1991 run time.

In this manner a mean density for the liquid hydrogen can be determined for each of the beams and these are listed in Table 2 along with the derived uncertainty. The uncertainty is roughly 2%, and is dominated by systematics in the exact shape of the saturation curve relating density and temperature. This uncertainty, however, is relatively small when compared to other sources of experiment error and does not dominate the overall accuracy of the cross sections.

A complication in determining the target thickness is that under the standard working pressure of ~2 atm the target vessel titanium windows bow out in the center by about 4.5 mm. For the short (27 mm) target vessel used in the HISS experiments this window curvature introduces a length variation of ~33% across the face of the target as illustrated in Figure 34 which shows a dimensioned profile of the short target vessel. A realistic beam, also illustrated in the figure, has a finite extent over the curved surface of the target and varies in intensity over this area. Thus, the actual nuclear interactions in the target occur over a distribution of LH_2 pathlengths. With the upstream beam vectoring, however, the exact beam profile can be determined for each run as discussed in the previous section. This beam profile is then convoluted with the target pathlength variation and multiplied by the mean density for the particular beam to yield the target thickness distribution. This process is illustrated in Figure 35 where the left most panel shows the vertical (y) profile of the 400 MeV/nucleon ^{32}S beam, the middle panel shows the calculated target vessel pathlength distribution, and the right most panel shows the resulting LH_2 thickness distribution.

The uncertainty in the mean target thickness is actually dominated by the accuracy of the upstream vectoring which in turn is determined by the uncertainty in the physical location of the position sensing detectors. Thus, to evaluate the target error, thickness distributions were derived for beam profiles generated by moving one of the position detectors ±2 mm along both the X and Y axis. The mean of each of these 9 distributions is then used to determine the variance of the derived thickness.

Table 3 lists the adopted target thickness, in g/cm^2, as a function of beam species and energy. Also shown is the absolute and percentage uncertainty in the derived thickness. Most of these uncertainties are less than ~3%, with a few exceptions. One of these is the 400 MeV/nucleon ^{36}Ar where the error is dominated by the uncertainty in the LH_2 density (see Table 2). The other two, 400 MeV/nucleon ^{26}Mg and 800 MeV/nucleon ^{36}Ar, have a projected beam profile close to the edge of the target where the variation in the pathlength is large.

c. Upstream Charge Identification

Two detectors located just downstream of the target, SSD and BV, provide an initial measure of the fragment charge as it just leaves the target and before it has a chance to interact in any of the downstream detectors or air gaps. In addition, the BV detector was used in the event trigger to identify uninteracted beam particles and remove a majority of these from the data stream to enhance the collection of fragments. The SSD detector is a Li-drifted Silicon solid state detector of 1mm thickness and ~4.6 cm active area diameter. This detector is normally run at a bias voltage of +400 V and is readout by a peak sensing ADC via a charge integrating preamp and shaper. The BV detector is a 3mm thick scintillator of dimensions 2.5" high by 5" long viewed by two photomultiplier tubes one attached to each end, and is contained within an iron pipe that has a 2.5" x 4" aperture cut into it to shield the phototubes from the HISS magnetic field.

As these detectors are relatively simple and have very good charge resolution their calibration is relatively straight forward. A scatter plot of the raw SSD signal verses the BV is shown in Figure 36 for the 400 MeV/nucleon ^{32}S beam. Dominating the plot is the beam "spot" but there are also well defined "spots" for fragments from P down to O. Also seen in this raw plot are some backgrounds which must be removed before the calibration can proceed. These include multiple particle pile-up effects caused by two or more particles passing through the detector within a short period of time (microseconds). Pile-up causes the detector signal to either saturate (lines at top and

TABLE 2: LH$_2$ Density For All Beams

Beam	Energy (MeV/n)	$<\rho>$ (kg/m^3)	dρ (kg/m^3)	Beam	Energy (MeV/n)	$<\rho>$ (kg/m^3)	dρ (kg/m^3)
^{4}He	400	69.47	1.39	^{36}Ar	400	69.87	2.67
^{4}He	800	69.99	1.40	^{36}Ar	600	69.47	1.39
^{22}Ne	400	69.56	1.39	^{36}Ar	800	69.54	1.40
^{22}Ne	600	69.65	1.39	^{40}Ar	393	69.31	1.40
^{22}Ne	910	69.62	1.39	^{40}Ca	400	71.31	1.43
^{26}Mg	400	69.55	1.39	^{40}Ca	600	71.07	1.47
^{26}Mg	600	69.55	1.39	^{40}Ca	800	69.49	1.39
^{32}S	400	71.62	1.44	^{52}Cr	400	69.48	1.39
^{32}S	600	71.68	1.50	^{56}Fe	400	71.43	1.44
^{32}S	800	69.50	1.39	^{58}Ni	400	69.46	1.39

TABLE 3: Devired Target Thickness For All Beams

Beam	Energy (MeV/n)	L (g/cm^2)	dL (g/cm^2)	Error (%)	Beam	Energy (MeV/n)	L (g/cm^2)	dL (g/cm^2)	Error (%)
^{22}Ne	400	0.2380	0.0061	2.6	^{36}Ar	600	0.2368	0.0067	2.8
^{22}Ne	600	0.2392	0.0061	2.6	^{36}Ar	800	0.2264	0.0081	3.6
^{22}Ne	910	0.2367	0.0064	2.7	^{40}Ar	393	0.2327	0.0073	3.1
^{26}Mg	400	0.2262	0.0083	3.7	^{40}Ca	400	0.2502	0.0062	2.5
^{26}Mg	600	0.2338	0.0070	3.0	^{40}Ca	600	0.2507	0.0064	2.5
^{32}S	400	0.2525	0.0061	2.4	^{40}Ca	800	0.2379	0.0062	2.6
^{32}S	600	0.2482	0.0074	3.0	^{52}Cr	400	0.2364	0.0069	2.9
^{32}S	800	0.2384	0.0063	2.6	^{56}Fe	400	0.2510	0.0066	2.6
^{36}Ar	400	0.2443	0.0100	4.1	^{58}Ni	400	0.2382	0.0063	2.6

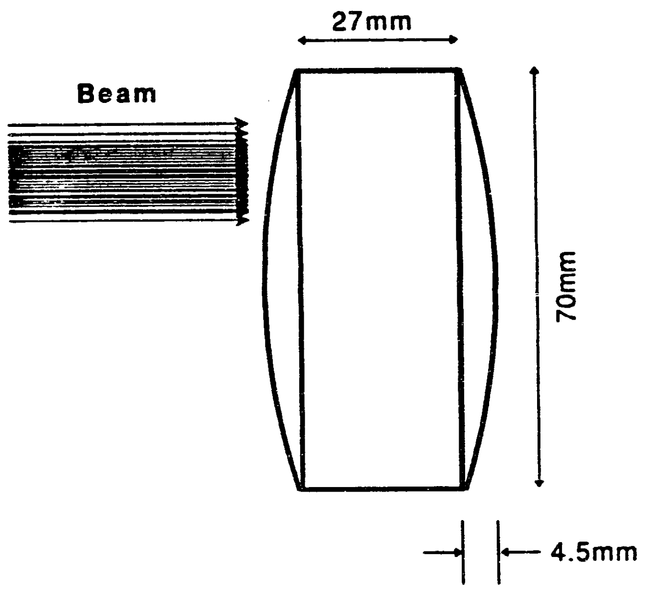

Figure 34. Target vessel used for the E938H experiments.

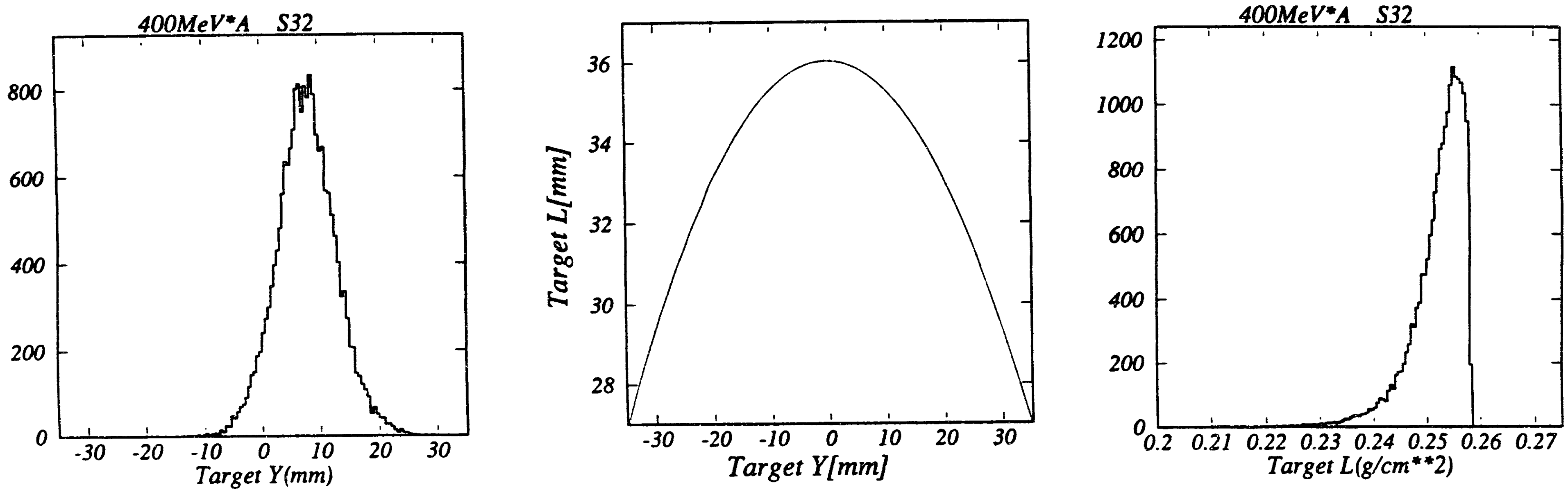

Figure 35. Vertical section of beam profile at target (left), target pathlength (center), and derived target thickness in g/cm^2 (right).

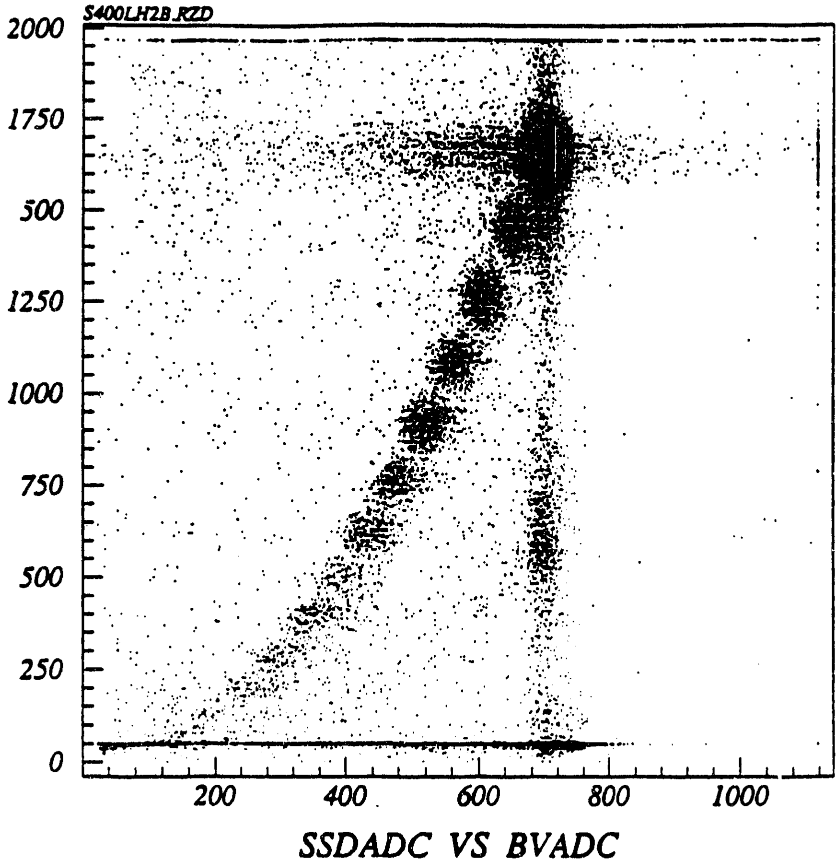

Figure 36. Raw data SSD versus BV scatter plot.

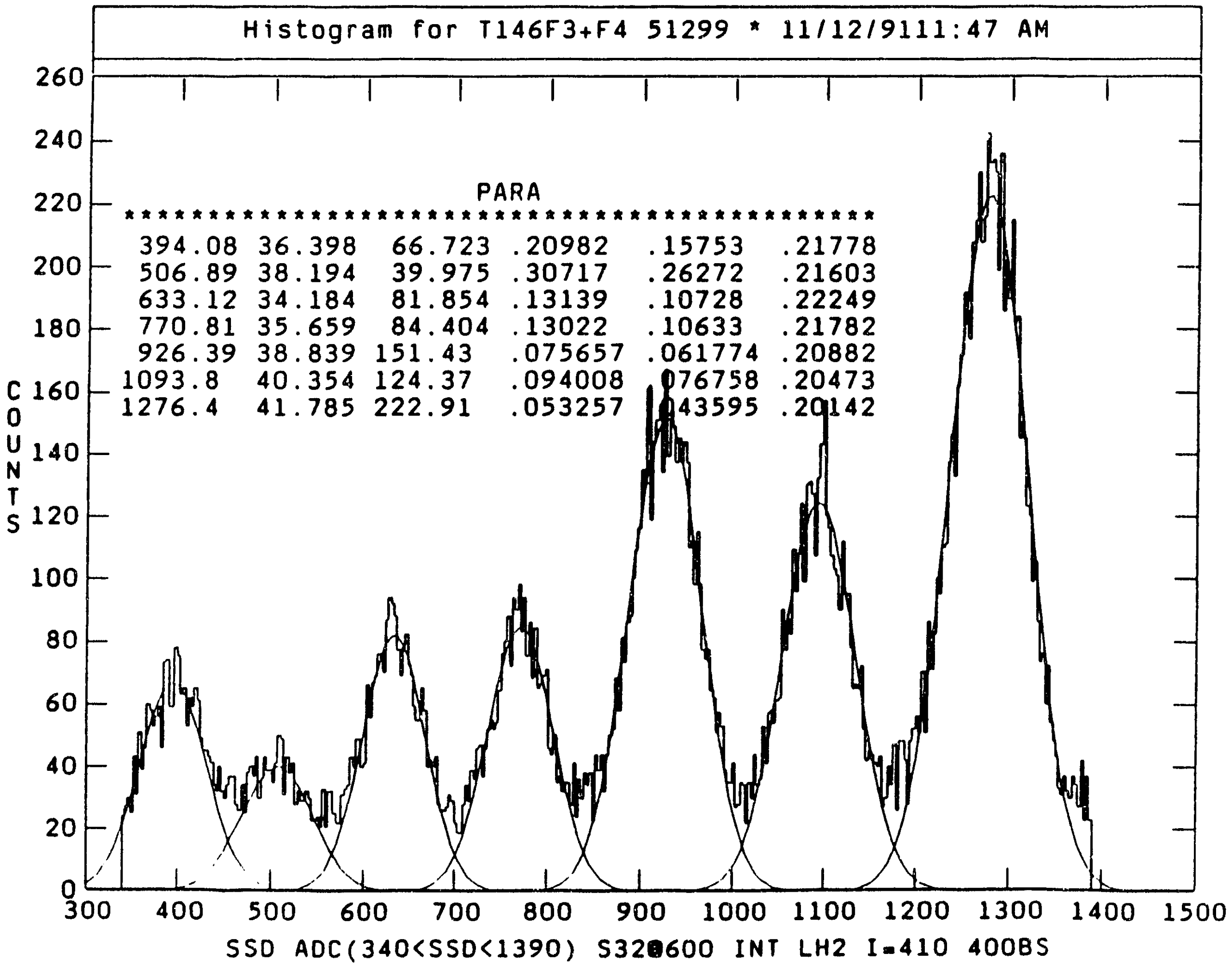

Figure 37. Multiple gaussian fit of a SSD charge histogram.

right side) due to the excessive energy deposit or, in the case of the SSD, to be reduced (e.g. vertical "line" at about BV ADC of 700) due to the finite period of time (several microseconds) that it takes the SSD shaper circuit to return to baseline. While the experiment trigger did include some pile-up protection, this could not be extended over the full time scale necessary for integrating the SSD charge signal. Also seen in the raw data plot are SSD "underflows" (line at the bottom of the plot) which are caused by particles missing the active region of the SSD but hitting the larger BV detector. Finally to the left of the diagonal formed by the valid events are particles which have interacted between the SSD and BV detectors.

After the background is removed the SSD signal is histogramed and a multiple gaussian fit is used to determine the means of the charge peaks as shown in Figure 37. These means form a linear relationship with Z^2 and, as shown in the top panel of Figure 38, can be fit with the least square method to provide the SSD charge calibration parameters.

The BV detector has somewhat poorer charge resolution and the charge peaks are not as easily identified. Instead, the calibrated SSD is used to select a particular element and then the BV signal is histogramed. These elemental histograms are then fit with a gaussian distribution to determine the mean signal. The process is repeated for each of the fragment elements and the means form a linear function of charge as shown in the bottom panel of Figure 39

These calibrations need to be performed for both Target In and Target Out, as the energy deposit in the detectors is different for the two cases, as well as for each beam as the tube voltages and amplifier gains are adjusted to optimize the charge resolution for each run. Table 4 lists the derived calibration parameter for all these cases. Figure 40 shows a scatter plot similar to Figure 36 but with some of the background effects removed and the charge calibrations applied. Here the element "spots" are identified with a change number and the resolution especially along the diagonal, is quite clear. In fact the upstream charge assigned to the event is actually a combination of the independent charge measurements weighted 3 to 1 in favor of the higher resolution SSD. A histogram of the combined charge is shown in Figure 41 and a change resolution of 0.16e is indicated.

d. Drift Chamber

The HISS facility Drift Chamber (DC) was used for the E938H downstream fragment tracking and details of the electronics design and operation principles can be found in Kobayashi et al.[14]. The chamber itself consists of an active volume that is dimensions 150 cm vertical by 200 cm horizontal by 140 cm deep and which is filled with P10 (90% Argon and 10% Methane) gas. This active volume is isolated from the laboratory environment by two 50 μm thick mylar windows separated by 3 cm at both the entrance and exit of the DC, between which dry nitrogen is constantly flowed. Within the active volume are 15 wire planes of drift cells. Seven of these planes are orientated in the vertical direction (S) and the rest have wires tilted by 30° to the left (T) or to the right (U). The S planes have 96 drift cells while each of the T and U planes have 120 cells. The wire arrangement in each drift cell is shown in Figure 42 and consists of a 1 cm by 2 cm rectangular arrangement of field-shaping (FS) wires with a sense wire (S) at ground potential in the center. The voltage on the field-shaping wire follows the formula $V_i = V_o + \partial V \cdot (i-1)$ where ∂V = -200 V and V_o is adjusted according to the particular beam to maximize the dynamic range of the detector system. This voltage varied from -1570 V for 400 MeV/nucleon ^{58}Ni to -1850 V for 400 MeV/nucleon ^{4}He.

The main objective of the DC calibration is to obtain a drift-time to drift-distance or space-time curve appropriate to the particular beam. In fact, for each beam we determine three separate space-time curves corresponding to the separate trigger-delay (TDC offset) of the three CAMAC crates containing the LeCroy 4291 TDC readout modules. To start the calibration procedure an initial guess is made for the space-time function. This is usually a linear function such as shown in

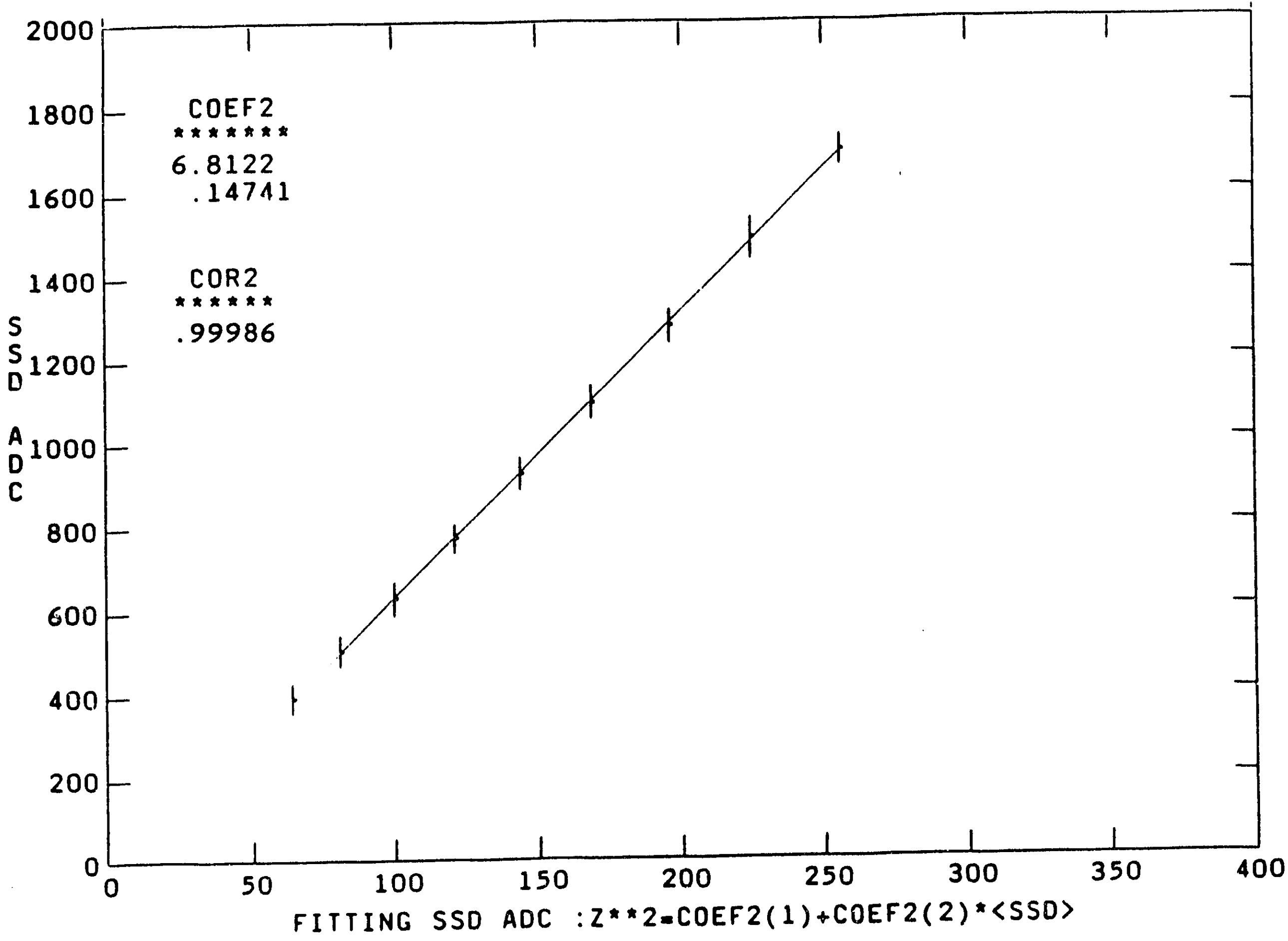

Figure 38. Calibration curve for the SSD as a function of Z^2.

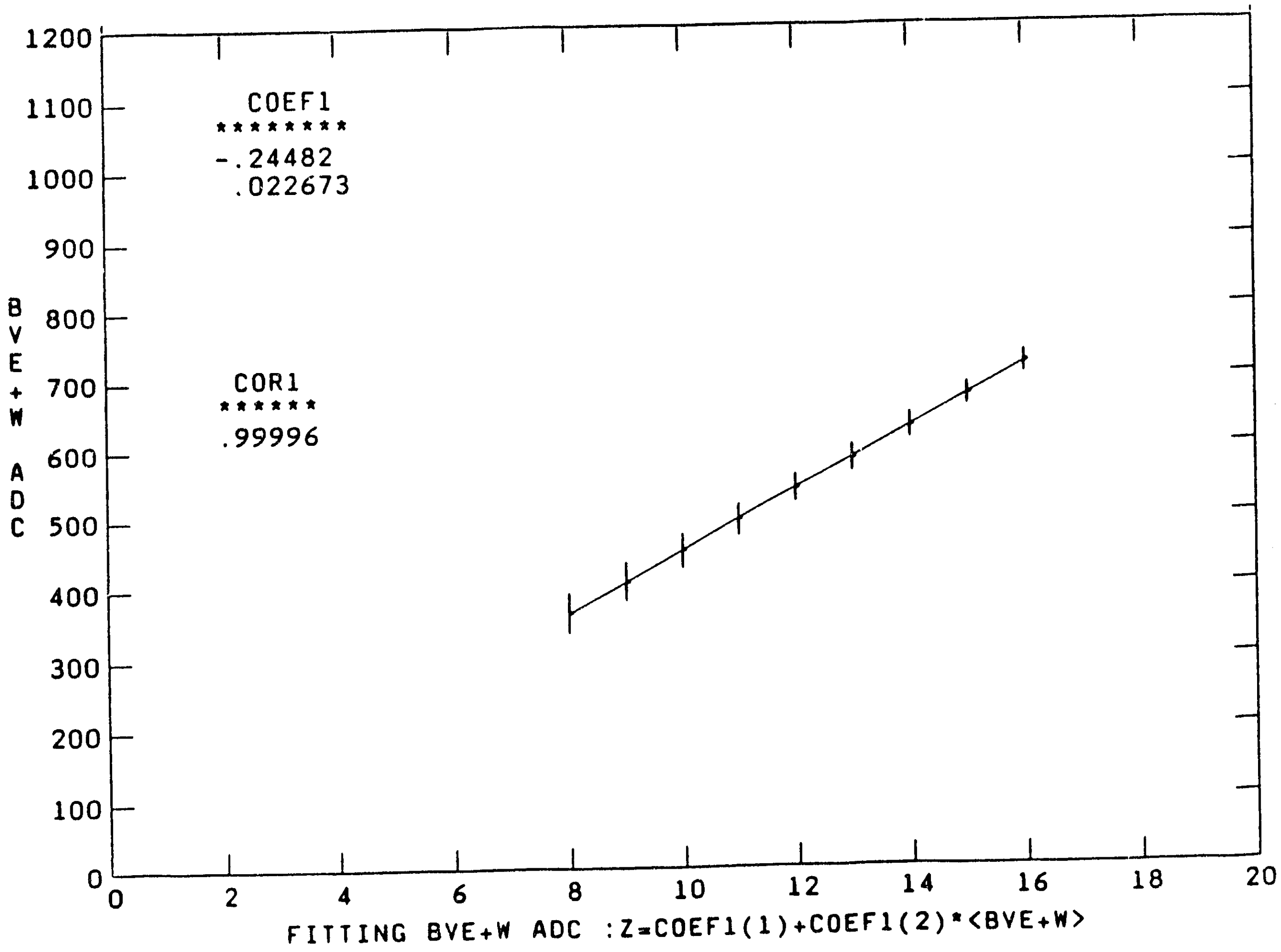

Figure 39. Calibration curve for the BV as a function of Z.

TABLE 4: Upstream Charge Calibration Parameters

SOLID STATE DETECTOR

Beam	Energy (MeV/n)	Target In		Target Out	
		Slope	Intercept	Slope	Intercept
^{22}Ne	400	0.056571	2.196400	0.056340	3.246100
^{22}Ne	600	0.057792	1.345250	0.056926	2.832900
^{22}Ne	910	0.058784	0.832570	0.057923	2.305300
^{26}Mg	400	0.080857	4.242770	0.081988	4.348200
^{26}Mg	600	0.082689	2.229670	0.081772	4.567300
^{32}S	400	0.150790	6.915500	0.151540	9.642100
^{32}S	600	0.147410	6.812200	0.146400	8.940500
^{32}S	800	0.140270	6.315000	0.138370	9.871500
^{40}Ar	393	0.174710	10.45600	0.178230	10.94900
^{36}Ar	400	0.183580	12.03100	0.189760	10.50200
^{36}Ar	600	0.180590	7.896100	0.177570	13.30700
^{36}Ar	800	0.175670	8.512400	0.175190	10.63100
^{40}Ca	400	0.229480	12.86100	0.233520	14.83400
^{40}Ca	600	0.222360	10.81600	0.223030	12.52500
^{40}Ca	800	0.219590	10.47100	0.218790	13.26400
^{52}Cr	400	0.315740	21.52000	0.325990	21.54800
^{56}Fe	400	0.382140	22.68600	0.397280	22.16500
^{58}Ni	400	0.430650	33.29000	0.452130	29.58000

BEAM VETO DETECTOR

Beam	Energy (MeV/n)	Target In		Target Out	
		Slope	Intercept	Slope	Intercept
^{22}Ne	400	0.011304	-0.340200	0.010201	0.604020
^{22}Ne	600	0.011293	-0.163330	0.010284	0.606800
^{22}Ne	910	0.011401	0.231270	0.010671	0.775530
^{26}Mg	400	0.012413	0.590940	0.013601	-0.254300
^{26}Mg	600	0.013848	-0.923880	0.012739	0.032707
^{32}S	400	0.023483	-0.359640	0.022397	0.430130
^{32}S	600	0.022673	-0.244820	0.021685	0.436730
^{32}S	800	0.021226	-0.493570	0.020254	0.242000
^{40}Ar	393	0.020593	-0.703500	0.020479	-0.600340
^{36}Ar	400	0.023688	-0.723920	0.023098	-0.247420
^{36}Ar	600	0.021350	-1.378400	0.020470	-0.588800
^{36}Ar	800	0.020898	-1.408700	0.020083	-0.704230
^{40}Ca	400	0.025945	-0.357760	0.025052	0.385560
^{40}Ca	600	0.027384	-0.120330	0.025309	0.931360
^{40}Ca	800	0.023555	-1.107500	0.022826	-0.431770
^{52}Cr	400	0.028763	0.603580	0.028571	1.134900
^{56}Fe	400	0.031193	0.598650	0.031212	1.103800
^{58}Ni	400	0.030959	0.604370	0.031337	0.670710

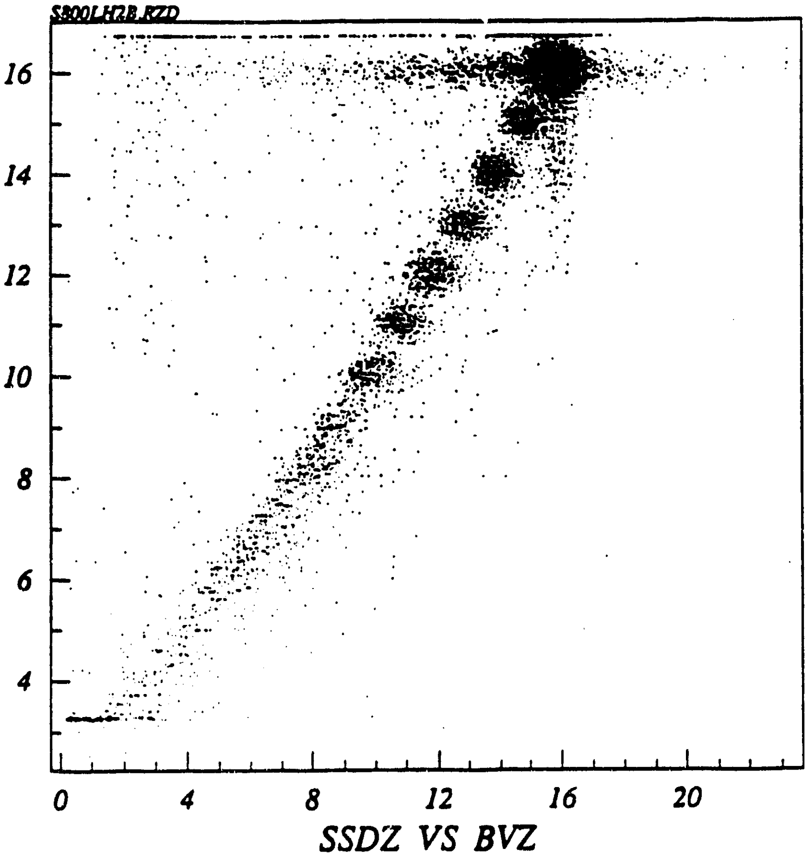

Figure 40. Scatter plot of calibrated SSD versus BV charge.

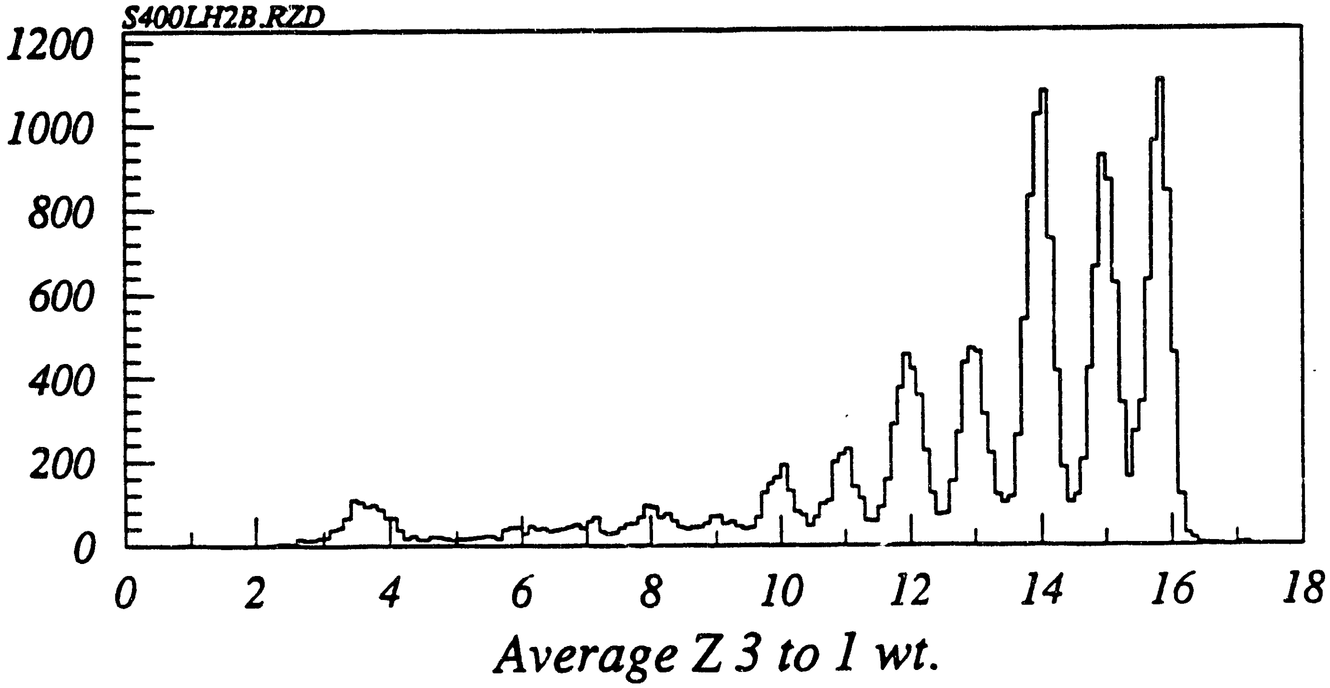

Figure 41. Histogram of combined upstream charge.

Figure 43 which has roughly the correct amount of TDC offset and approximately 150 ns time span corresponding to the maximum drift time within a drift cell. Using this function to calculate the hit position within a cell a scatter plot of this position versus TDC channel can be generated (Figure 44) and used in the initial iteration of the space-time function.

Next the particle trajectory is fit and the track residual is plotted against the hit position as shown in the top panel of Figure 45 and histogramed in the bottom panel. These residuals are the difference between the position of the track in a given plane as calculated from the current version of the calibrations and the position predicted in the same plane from the fitted track using all other planes associated with this track except the given plane. These plots are used for the remaining, fine-tuning of the space-time function. An incorrect TDC offset causes an uneven left-to-right distribution with respect to the cell center. A non-zero average residual, such as indicated in Figure 45, is generally caused by incorrect offsets between the different wire planes. Finally, an incorrect shape to the space to time function would introduce tilting and/or waving in the residual vs. hit position distribution. These parameters are adjusted until the residuals yield a flat, even distribution within the cell as shown in Figure 46. In addition, the timing can have a "walk" associated with the signal pulse height (ADC slewing) that, in general, is small, but which is also taken into account. An example of a final space-time function is shown in Figure 47.

The vertical (S) planes are the most crucial in determining all aspects of the space-time calibration as it is in the horizontal direction that the isotopes are separated. In addition the design of the DC precludes obtaining the same resolution along both the horizontal and vertical axis as the vertical position is derived from the tilted T and U planes. To date, DC calibrations for all of the April, 1990 runs and five of the 1991 beams have been completed. Over these runs we have consistently been obtaining a horizontal resolution of 350 μm and a vertical resolution of 450 μm.

e. The TOF Wall

The Time-of-Flight (TOF) wall is positioned as the last detector in the E938H configuration and is used to obtain a final measure of the fragment charge and to determine the particle velocity. The TOF wall is composed entirely of scintillator slats of varying width and length, the light output from which is viewed by independent photomultiplier tubes mounted on each end of a slat. A schematic of the TOF wall is in Figure 48 and shows the high resolution inner 1 m by 1 m portion composed of a double layer of 2 cm wide slats with an offset of 1 cm between the layers. Surrounding this region, in both horizontal and vertical directions, are 8 cm wide slats used to increase the effective aperture of the detector.

The charge resolution of this detector is normally quite good as can be seen from Figure 49 which is a histogram of the square root of the product (geometric mean) of the ADC values of the two phototubes viewing a single slat in the back layer of the central region. As these slats are thin compared with their length there is little horizontal (x) dependence to the signal and the vertical (y) dependence is directly proportional to the scintillator attenuation. This attenuation is normally quite uniform and using the geometric mean ADC cancels out the vertical dependence. However, just prior to the 1990 run time it was discovered that many of the front layer slats had developed surface crazing which effectively introduced a non-linear component to the light attenuation and, as shown in Figure 50, severely degraded the charge resolution. Fortunately, we were able to correct this effect in the 1990 data by generating plots like Figure 51 of the geometric mean ADC versus the vertical position determined from the DC vectoring for each of the 100 central (2 cm wide) slats. In a slat without the surface crazing such a plot would consist of horizontal bands where each band corresponds to a particular elemental charge. Thus, using the shape shown in Figure 51 a y-dependent correction factor for each slat can be determined. Applying these factors to the data results in almost fully restored charge resolution (see Figure 52).

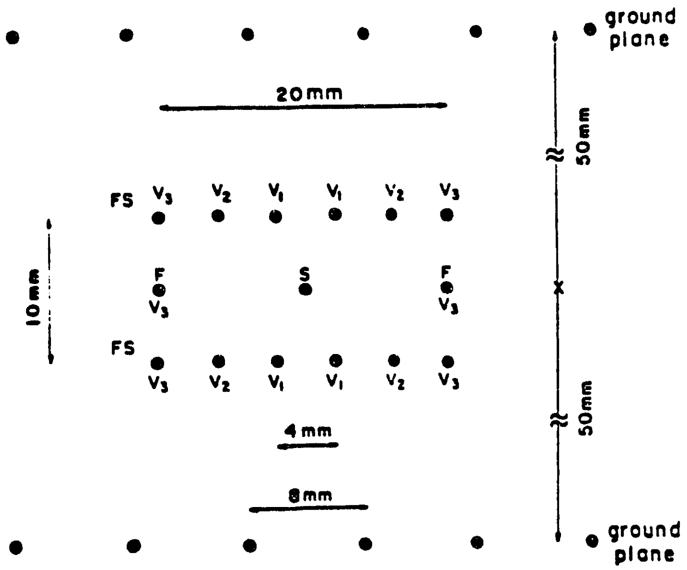

Figure 42. Drift cell wire arrangement.

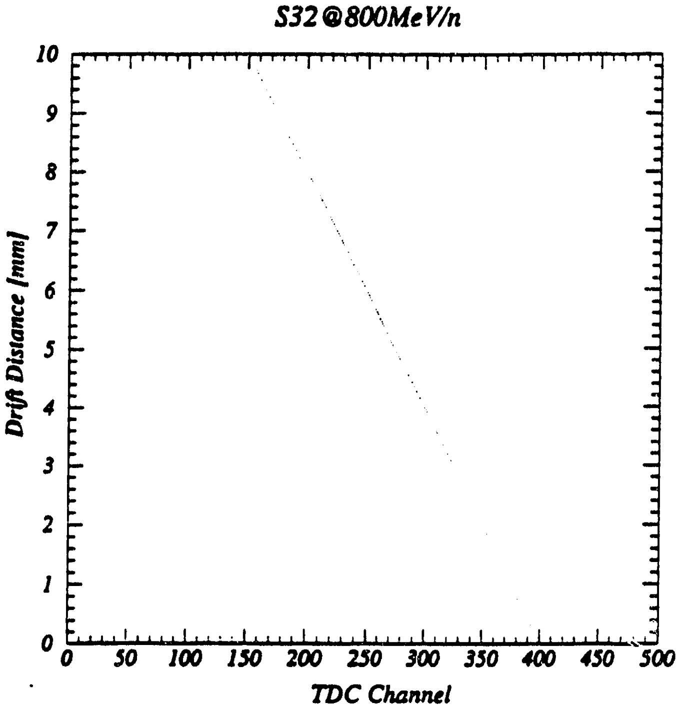

Figure 43. Initial guess at space-time function.

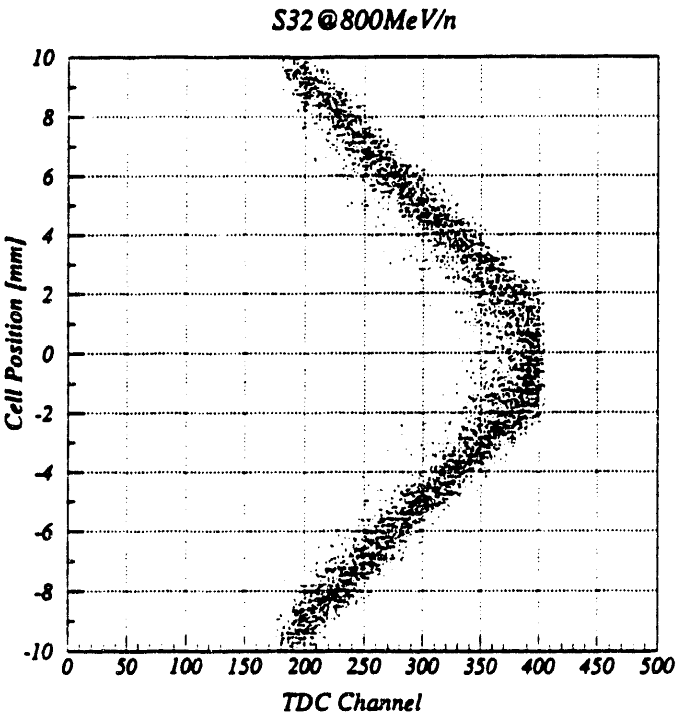

Figure 44. Initial hit position vs. time.

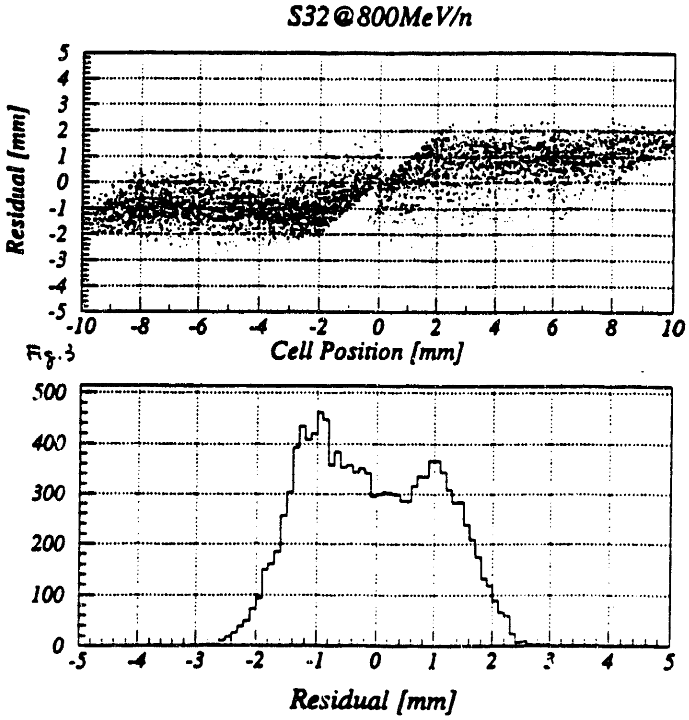

Figure 45. Initial trajectory residuals.

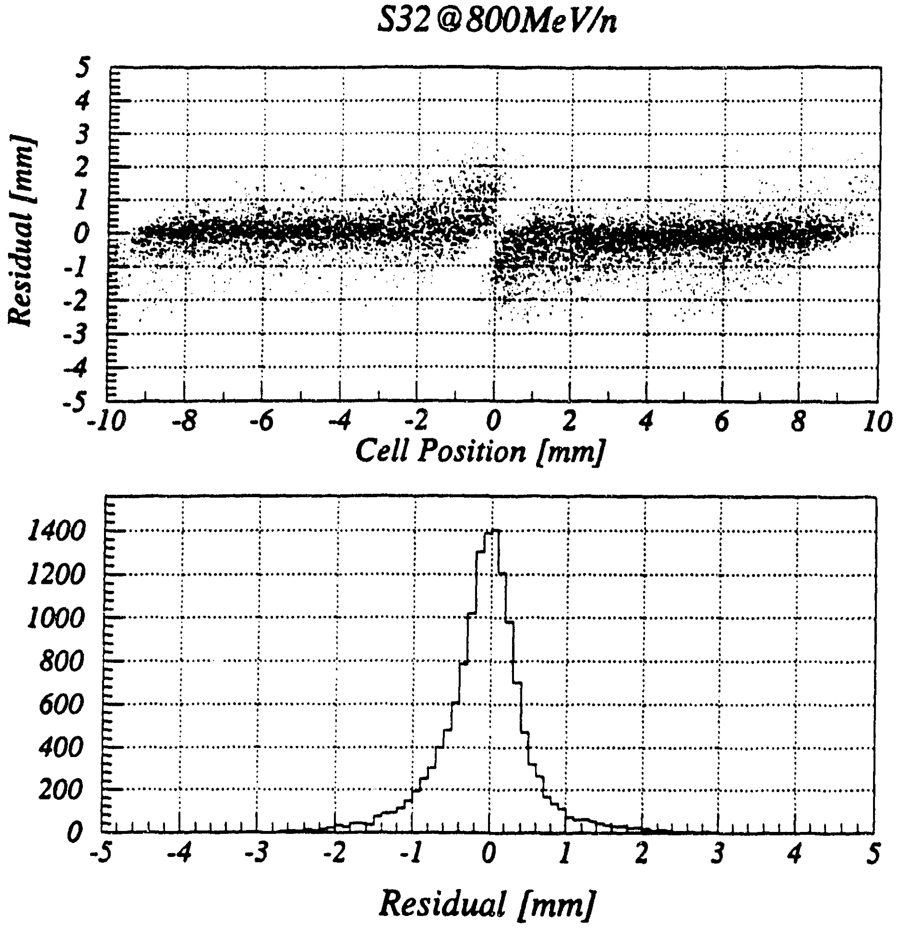

Figure 46. Trajectory residuals as a result of the final calibrations.

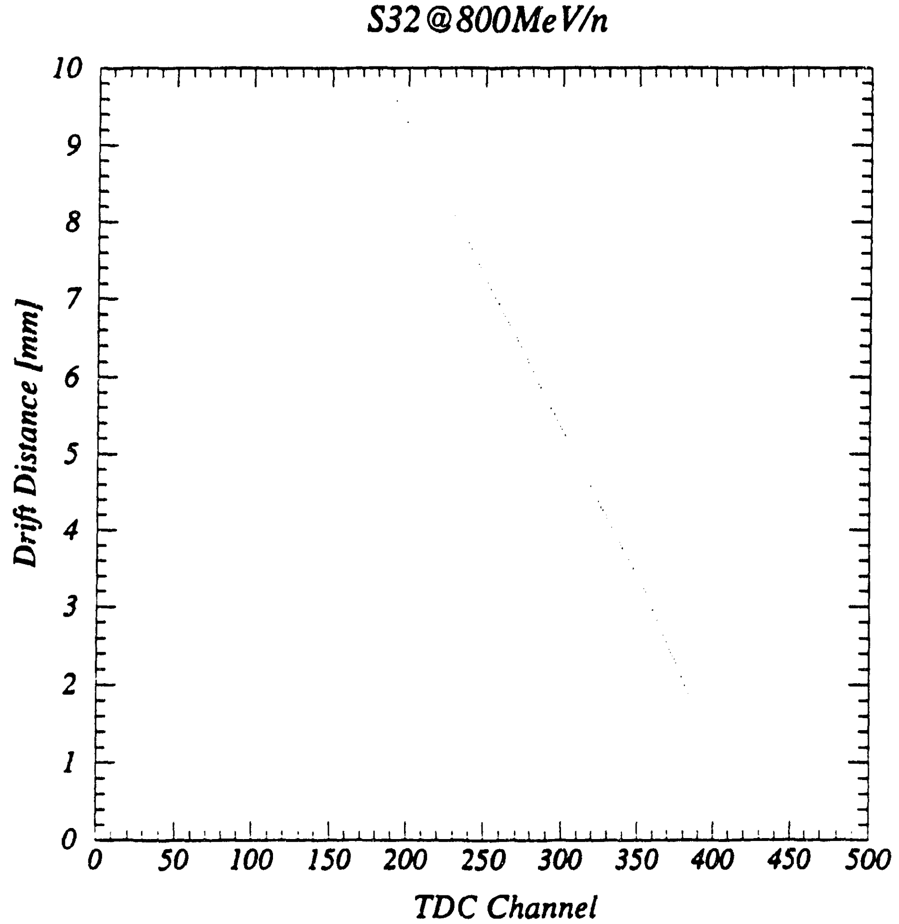

Figure 47. Final version of space time function.

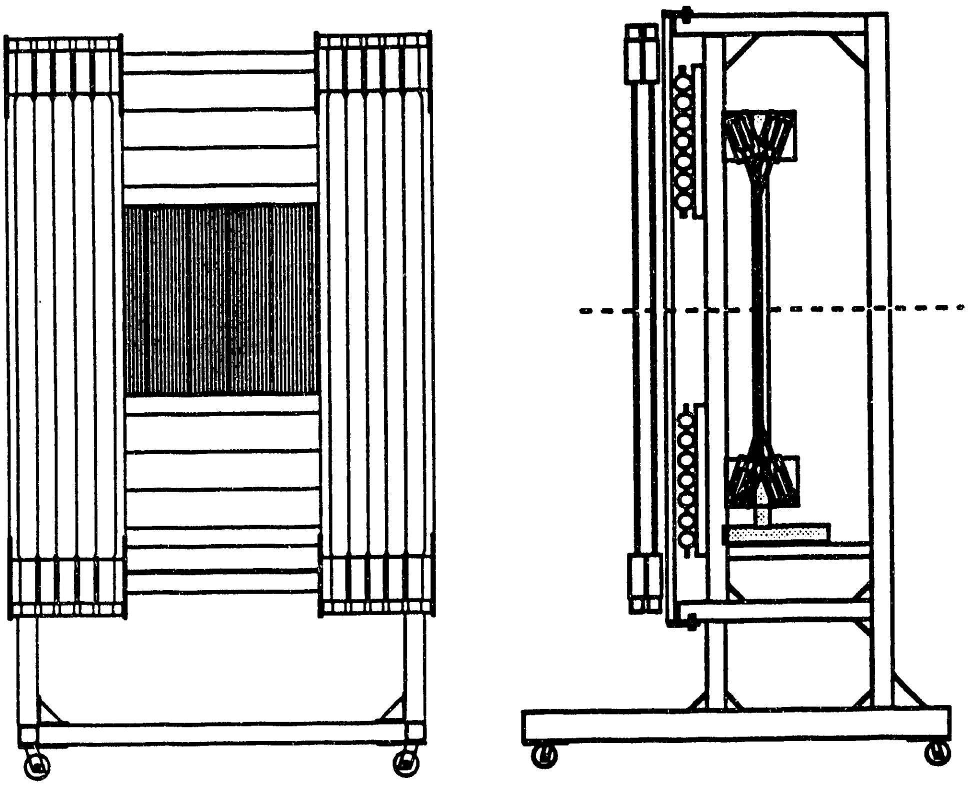

Figure 48. Schematic of time-of-flight (TOF) detector wall.

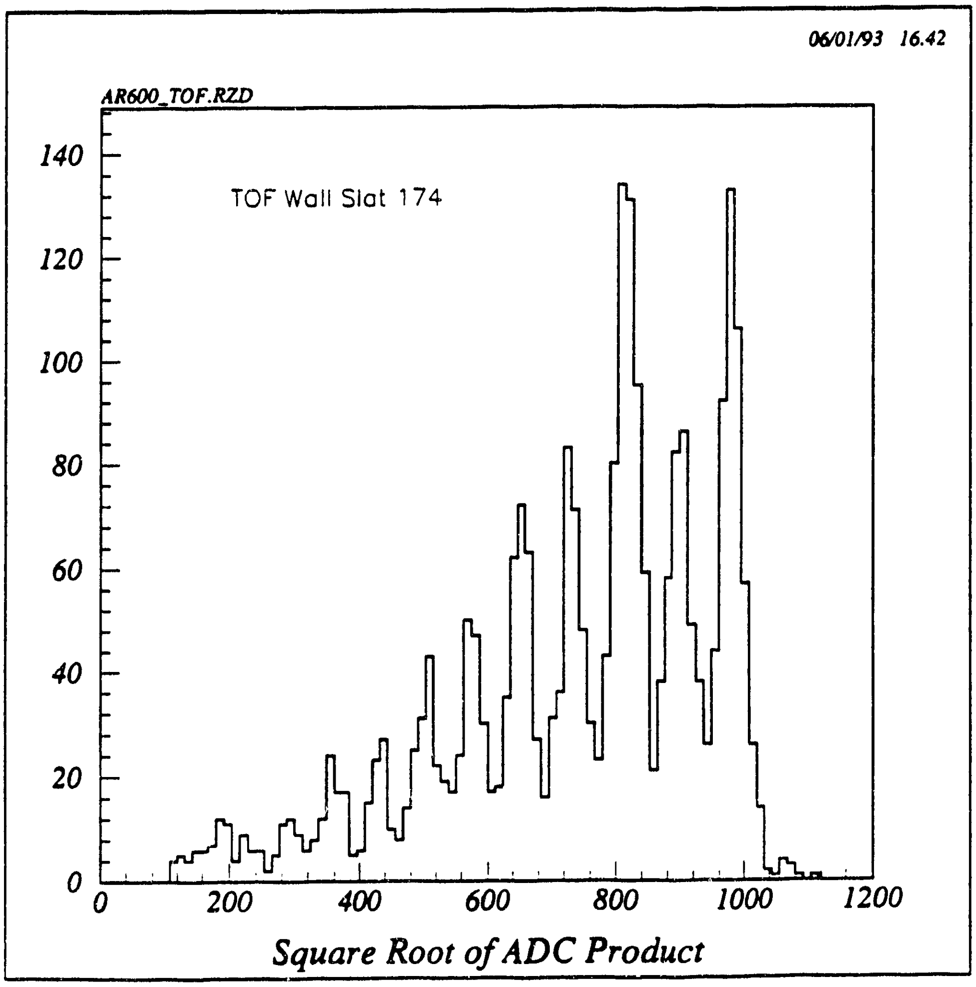

Figure 49. Charge histogram from an undamaged TOF wall slat.

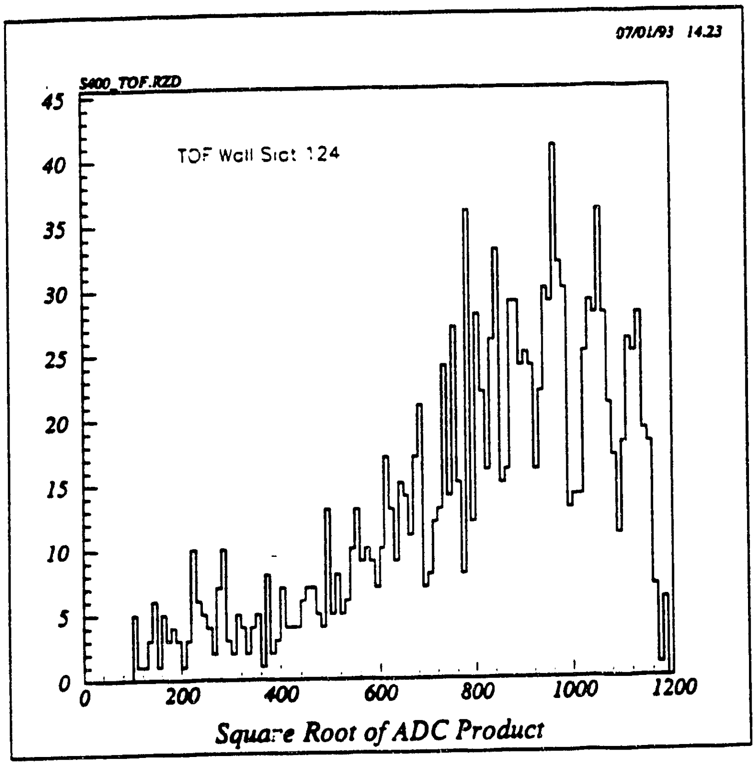

Figure 50. Charge histogram showing degraded resolution.

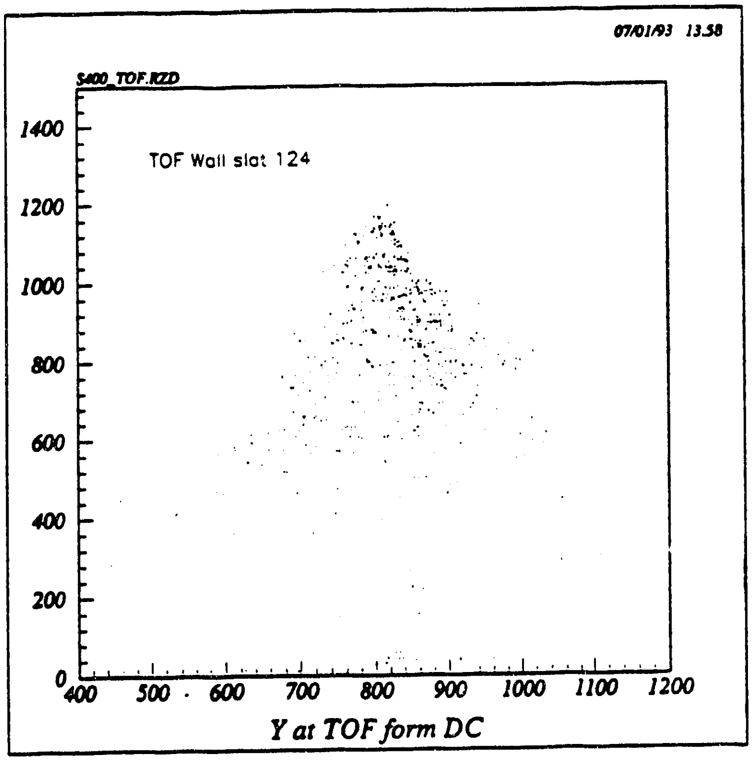

Figure 51. Slat ADC response as function of position.

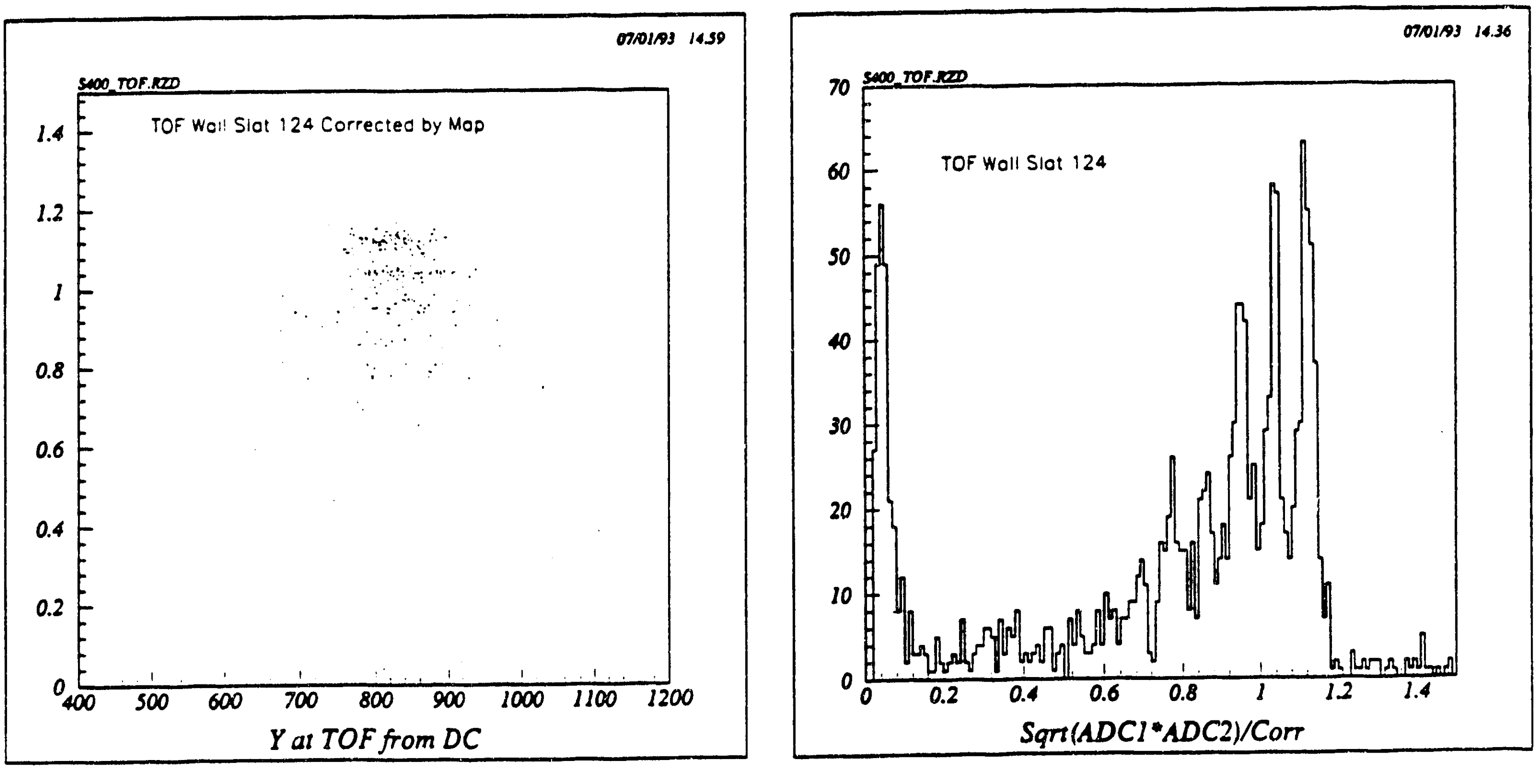

Figure 52. April, 1990 data corrected by an attenuation map with the ADC response vs. position on left and the charge histogram on the right.

The source of the surface crazing was investigated but it could not be determined whether it was due to a design flaw in the individual slat mounts or possibly due to radiation damage, or a batch of bad scintillator. Further it could not be determined whether the defects had stabilized or whether the crazing would grow worse. Recently, we began examining this problem using the 1991 data and in Figure 53 an identical plot for the same slat as in Figures 50-52 is shown for the more recent data set. At first glance the uncorrected data of both figures (51, 53) show the same shape, but when the 1990 correction map is applied the result is Figure 54 where clearly the charge bands (left) are not strictly horizontal. In fact, the "corrected" charge bands show a residual hump at the y position of the uncorrected feature indicating that the slats have degraded further. A histogram of the "corrected" geometic mean ADC is given in the bottom panel of Figure 54. Thus, we will need to regenerate the attenuation correction map for the 1991 data and this work is now in progress.

The particle velocity is determined by timing the events from the S1,S2 trigger scintillators to the TOF wall. To obtain this time the raw signals must be corrected for TDC offsets (e.g. cable delays), pulse-height dependent timing walk (ADC slewing), effective velocity light propagation delays, and non-linear effects introduced by the TOF wall damage. Currently, these TOF calibrations are in a preliminary state that are sufficient for the 400 MeV/nucleon ^{32}S beams. A sample of the timing for this beam is shown in Figure 55 and the gaussian fit has a sigma of 5.1 "channels" which corresponds to a time resolution of about 150 ps. There is still a considerable amount of work associated with this calibration and it is expected that the time resolution can be improved.

Particular improvements include an analysis of ADC slewing effect which is currently not incorporated into the analysis code. ADC slewing is caused by the relationship between the TDC discriminator threshold and the shape of the rising edge of the phototube output pulse shape. With a fixed threshold the relative time to trigger the TDC varies according to position of this level on the pulse leading edge and this is directly related to the pulse height. From this effect one expects the timing delay to increase with decreasing pulse height. This is, in fact, the behavior seen in the TOF wall as illustrated in Figure 56 for a particular slat. What is required is to produce a correction which will straighten out this curve for each ADC, TDC combination on the TOF wall.

Other necessary effort includes mapping the TDC offsets to take care of various differences such as cable delays. since these offsets are hardware setup related only they are beam independent and need to be determined once for a given run period. The offsets are currently available for the 1990 data, but still need to be determined for the 1991 run time.

The effective velocity of light propagation in the scintillator introduces a delay in the TDC signal that will be dependent upon the position of particle penetration through the slat. Normally this would be a more or less linear effect, but the scintillator crazing which seriously affects the light attenuation also affects this propagation delay. While the effect on the TDC's, fortunately, appears to be less drastic than on the ADC's, it nevertheless requires some corrections to be applied to the TOF wall time calibrations. This TDC position correction map is generated in the same way as the ADC position correction map; by plotting the average slat TDC versus position from the DC trajectory and using the digitized curve as a correction. This must be done for every slat in the TOF wall. Currently the work is complete for the April 1990 run, but has not yet been verified to apply to the 1991 data. Given the fact that the crazing problem has worsened, it is likely that these maps will need to be regenerated for the 1991 runs.

3. Data Selection and Validation

The detector calibrations allow the raw data to be converted toscience units, where physical effects can be more easily displayed and interpreted. At this stage, the analysis turn toward determining criteria for valid events, selecting these events, determining whether any biases exist in

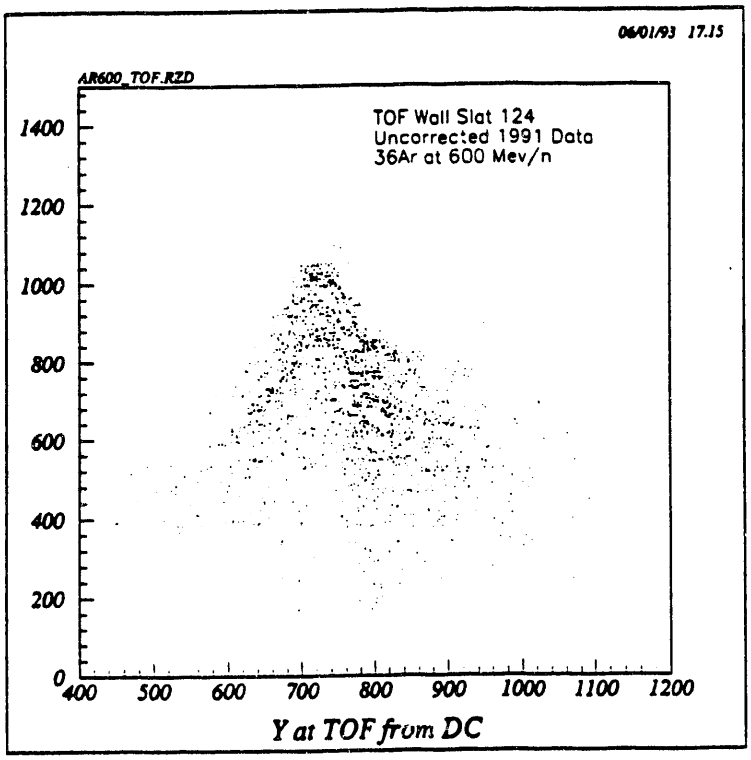

Figure 53. Slat ADC response versus position for the April, 1991 data and the same slat in Figures 51 and 52.

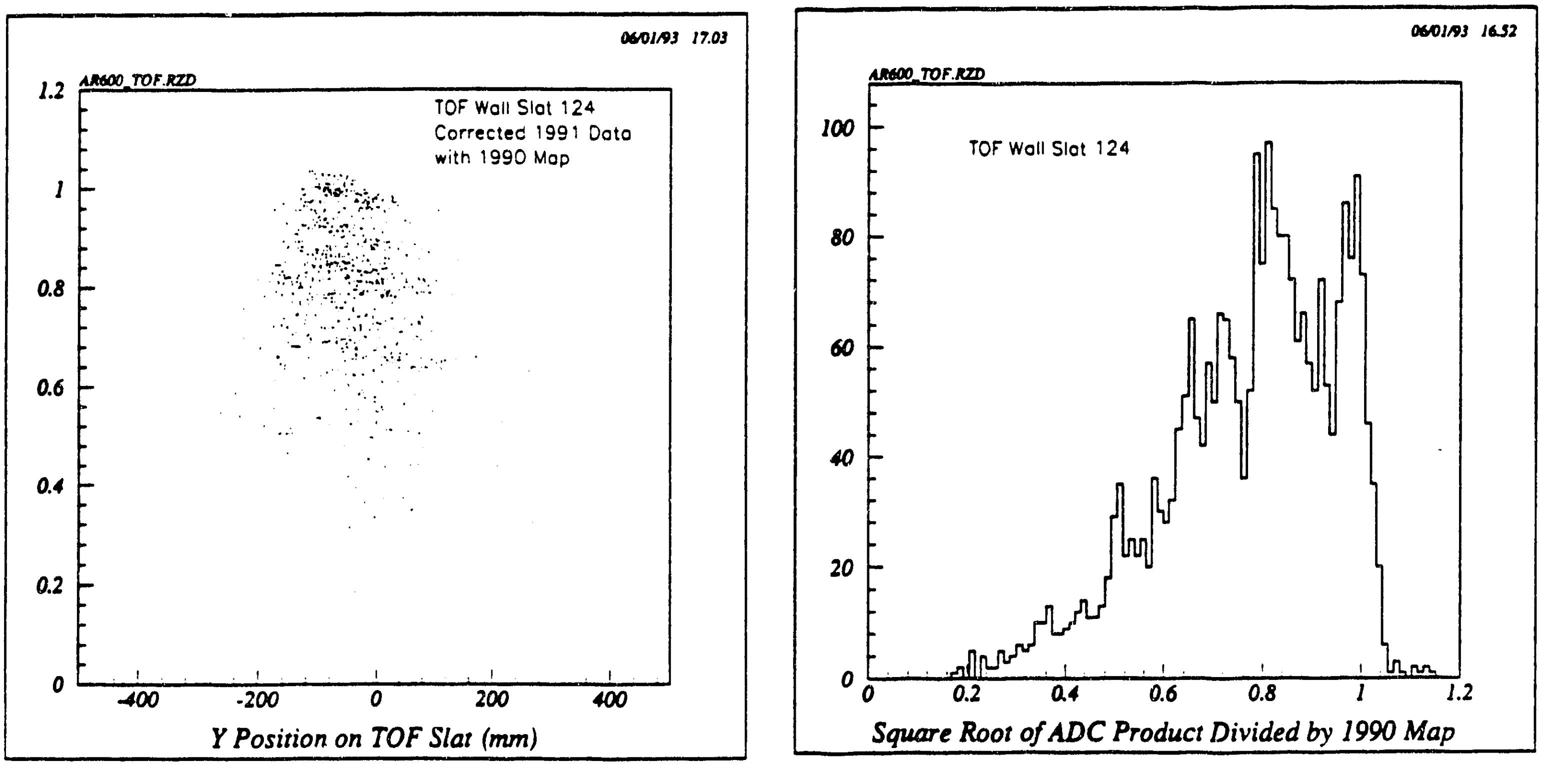

Figure 54. Results of applying the 1990 attenuation map to the 1991 data indicating continued damage to the TOF wall slats.

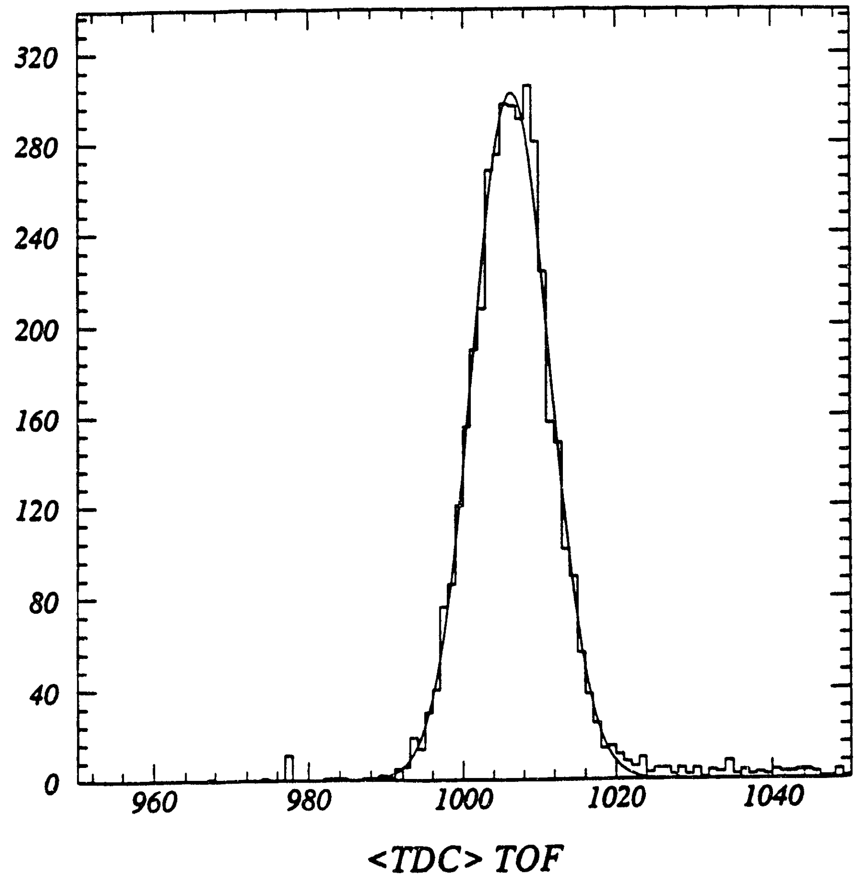

Figure 55. Current timing resultion from the TOF wall.

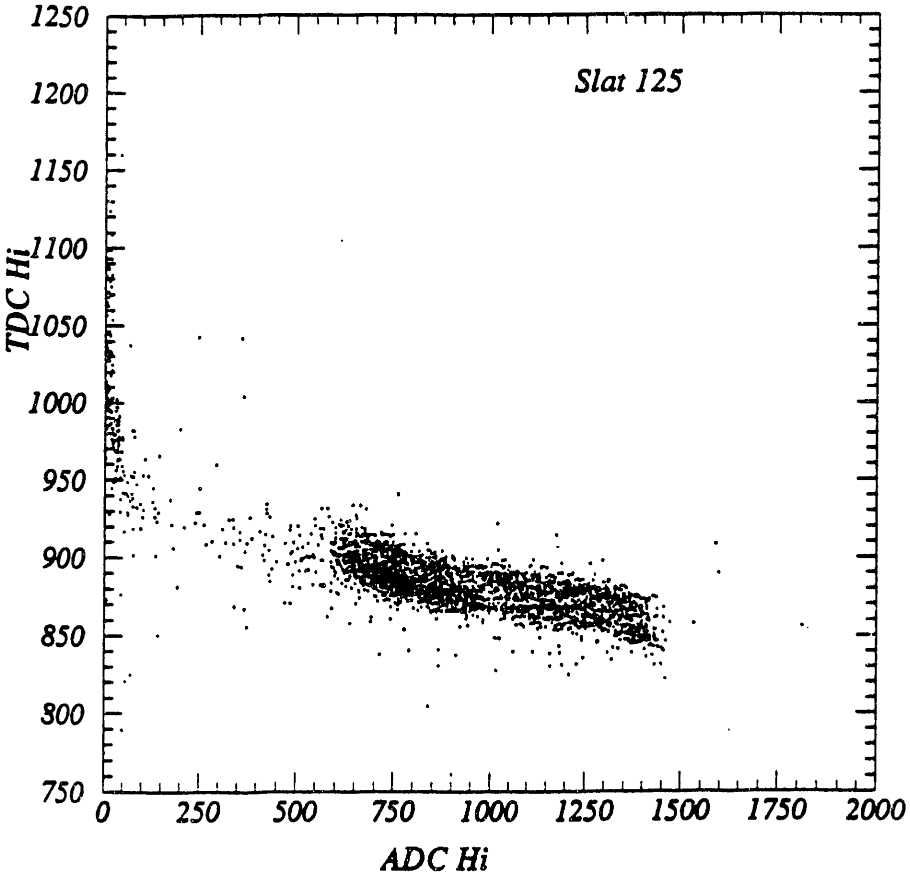

Figure 56. Scatter plot indicating the pulse-height dependent timing walk for a single tube on a TOF wall slat.

the data subset, developing correction techniques and/or parameters for these biases, and finally validating the scientific results. Over the last year considerable effort has been devoted to developing the techniques and procedures for assuring a high quality scientific product. This has involved several iterations of the 400 MeV/nucleon ^{32}S isotopic cross sections and the full complement of charge-changing cross sections as the sophistication of our validation procedure and detector calibrations improve. In fact, our initial cross checking identified several areas where our system calibrations had to be improved.

There are a number of approaches that we can take to assure the quality of our cross section data. These approaches include checks on internal consistency of the various independent cross section calculations, monitoring of the incident beam flux and beam focus, and investigation of the effects of our cuts on the resultant cross section values.

Monitoring the incident beam serves two purposes: (1) Any dramatic change in the incident beam characteristics signifies the potential for unknown and unwanted contamination of the beam by fragmentation upstream of the LH_2 target. (2) Various types of common-mode noise and/or electronics problems will show up most clearly in the beamline ADCs and TDCs since we are dealing with a single nuclear species at a well-defined single energy.

The actual process of monitoring the incident beam is relatively simple as a full set of diagnostic scalers, ADC's and TDC's are embedded in the data stream. These can be plotted and examined for any deviation in the diagnostics from some nominal set of values determined when the beam is stable. A sample of these plots for the 400 MeV/nucleon ^{36}Ar "Interaction" (INT) trigger is shown in Figures 57 through 68. The first set of plots shows nominal behavior for a variety of data stream monitors (Figure 57), scaler rates from the trigger scintillators (Figure 58), trigger logic monitoring rates (Figure 59), trigger scintillator ADCs (Figure 60), monitors of the SSD detector ADC (Figure 61), and trigger scintillator TDCs (Figure 62). These can be compared to the same displays where a glich in the the event triggering occurred during mid-run (Figure 63 to 68). By examining these diagnostic variables as a function of time,we can detect any change in the beam,whether a gradual drift of a variable, or a sudden discontinuity. Any such change in the beamline variables disqualifies the events in question from inclusion in our data analysis.

With the large volume of data currently under analysis we have also automated part of this diagnosis process. In particular the upstream beam definition detectors are most critical to assuring that a good dataset is analyzed. For this case the ADC's, TDC's and scalers from detectors upstream of the LH_2 target are statistically analyzed to obtain averages and variances when the beam is in a stable state. These nominal values used to define "good" beam are contained within a disk file along with a limit, in units of standard deviation, to the range that a particular event would be allowed to deviate from the mean value. Normally this limit is set to $\pm 2.75\ \sigma$. As for diagnostic scalers, proper values or ranges of values are set according to the function of the scaler. An example of such a Beam Definition File is shown in Table 5 for the 400 MeV/nucleon ^{32}S beam and in Figure 69 a sample set of beam definition histograms are shown. The nominal values and range limits indicate that only events with extreme deviations are cut while a majority of the data is left intact as illustrated in Figure 70.

Applying cuts to the data is always checked in the following manner. If the cut being applied is an upstream cut (i.e. upstream of the LH_2 target), the cross section calculation should be unaffected since the cut changes both the measured fragment populations and the measured incident beam flux independent of the resultant fragment species. If the cut depends upon variables associated with detectors downstream of the LH_2 target, careful consideration is given to the possible charge or mass dependence of the resultant fragment populations. In either case, we investigate the effects of our cuts upon the cross sections by recalculating the cross sections for various degrees of the same cut (typically, a cut is defined as a range of a real variable about its

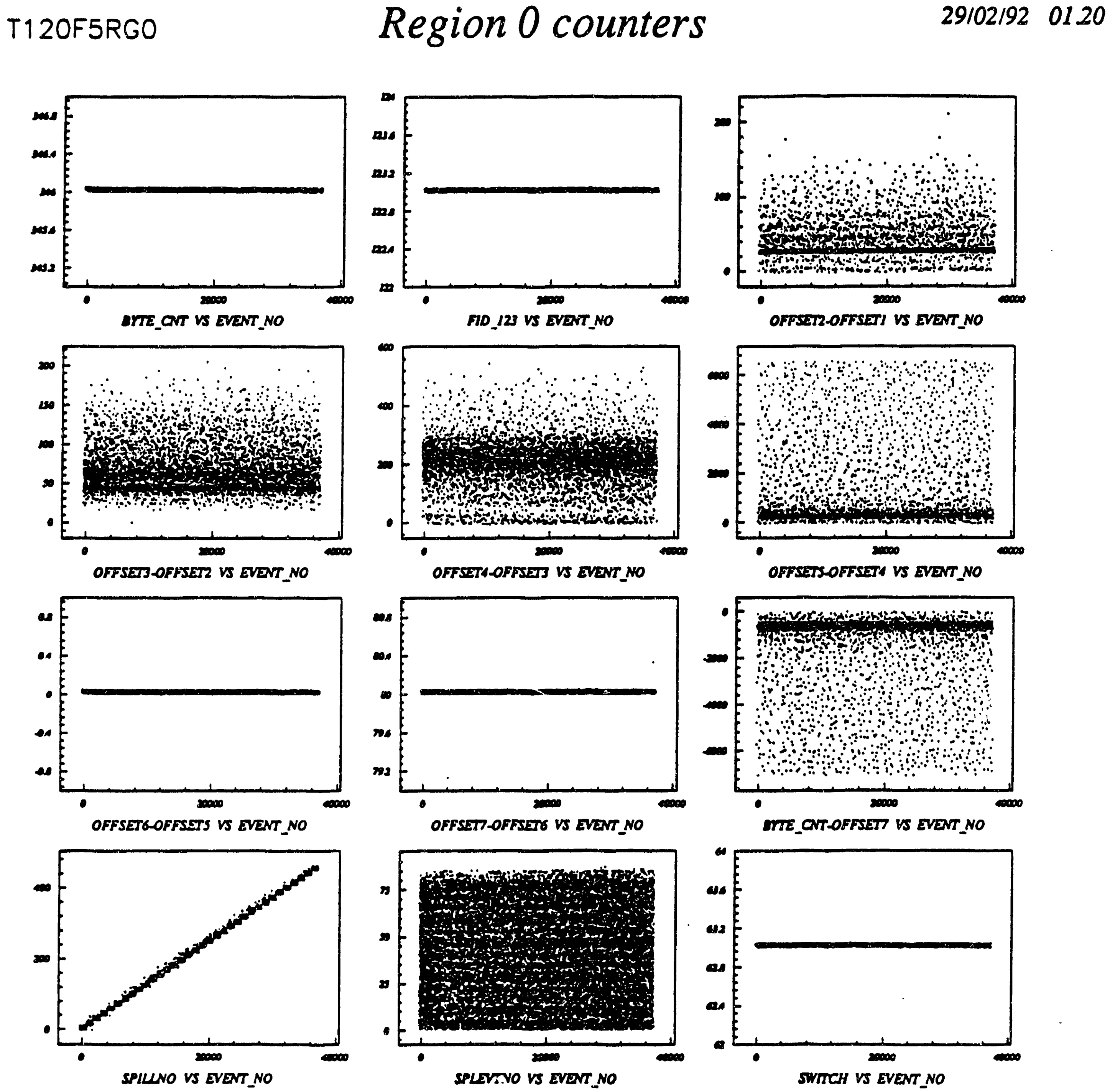

Figure 57. Normal run diagnostic plots for data stream monitors.

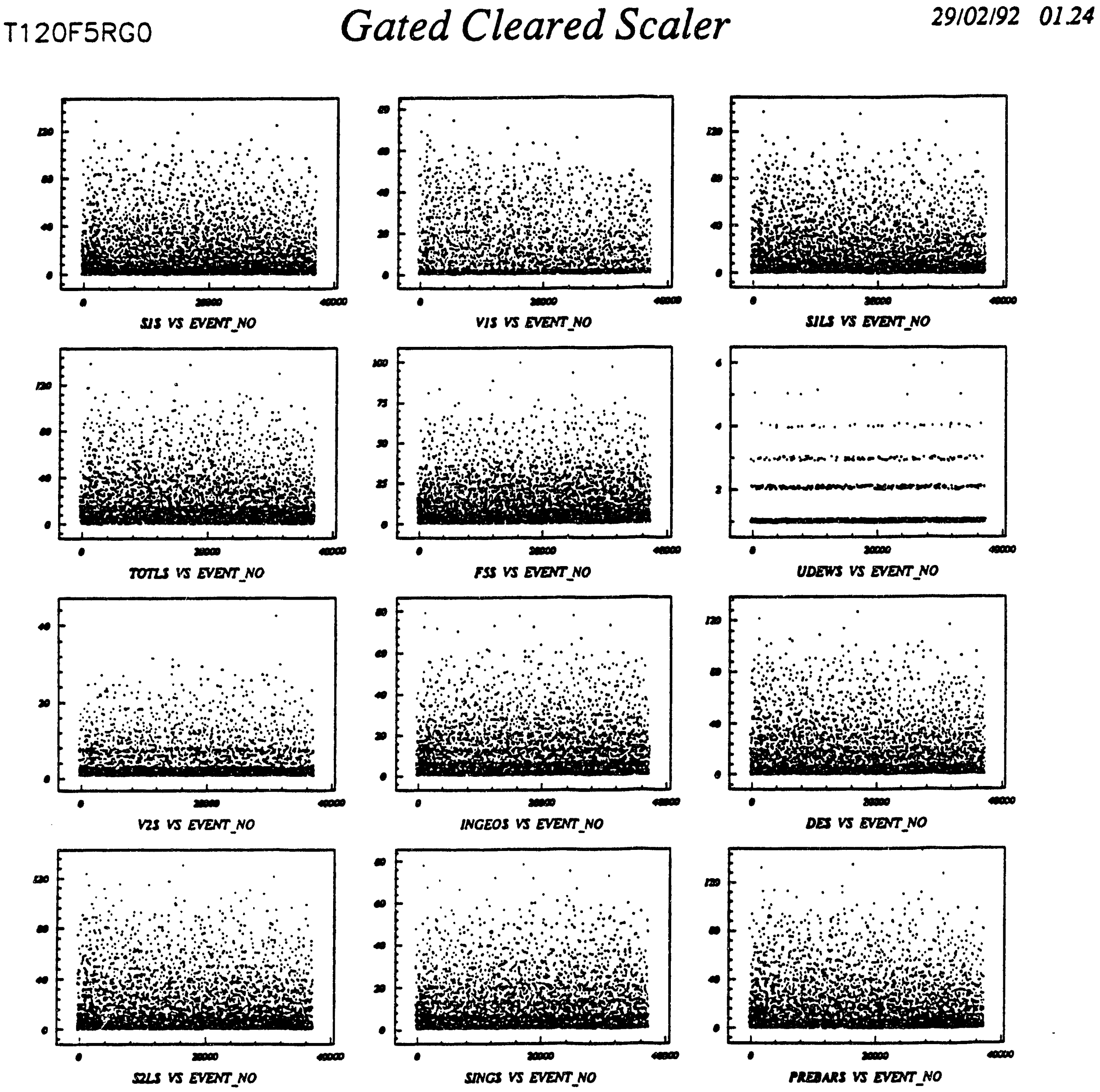

Figure 58. Normal run diagnostic plots for trigger scintillator scaler rates.

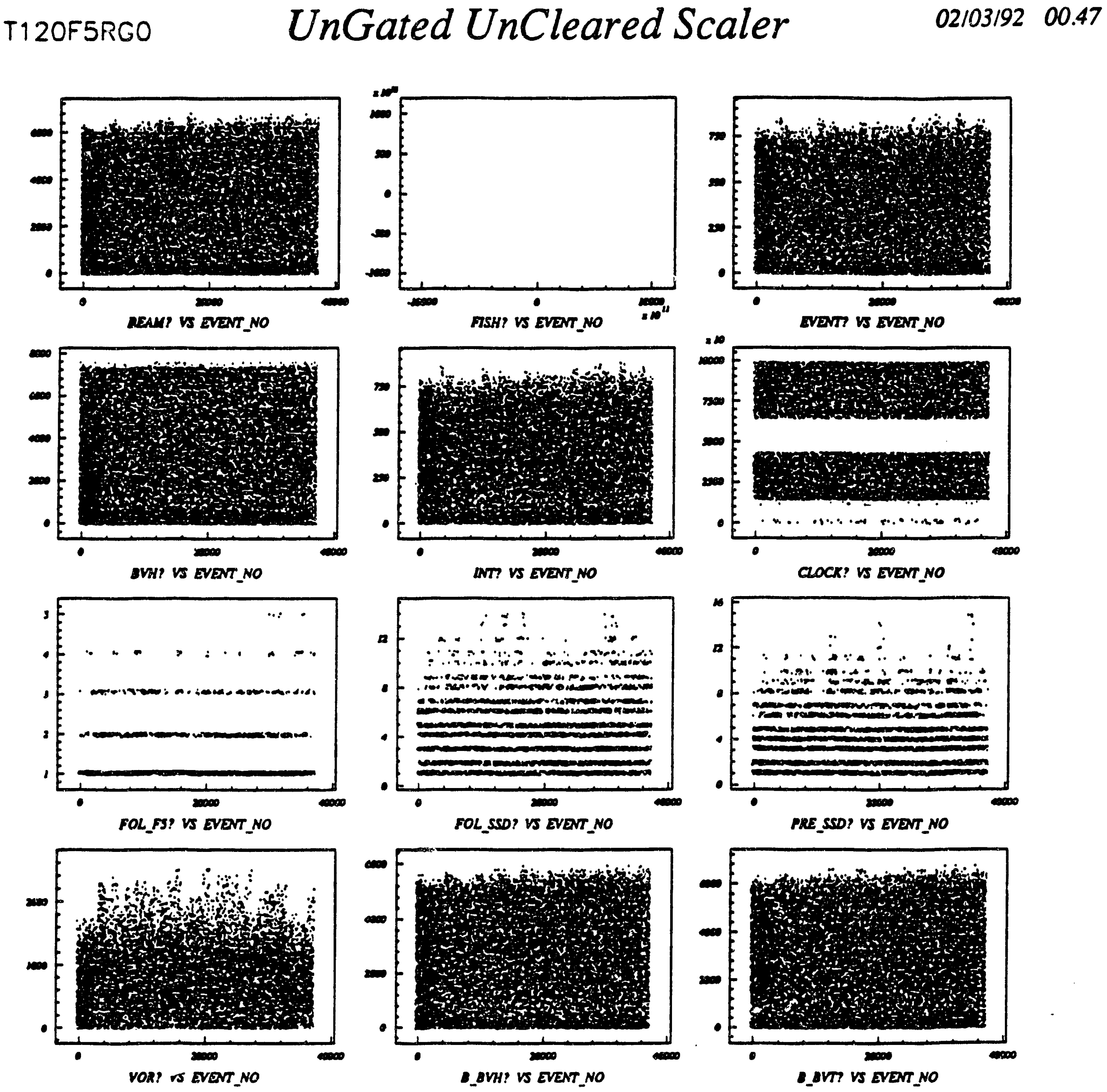

Figure 59. Normal run diagnostic plots for trigger logic monitoring rates.

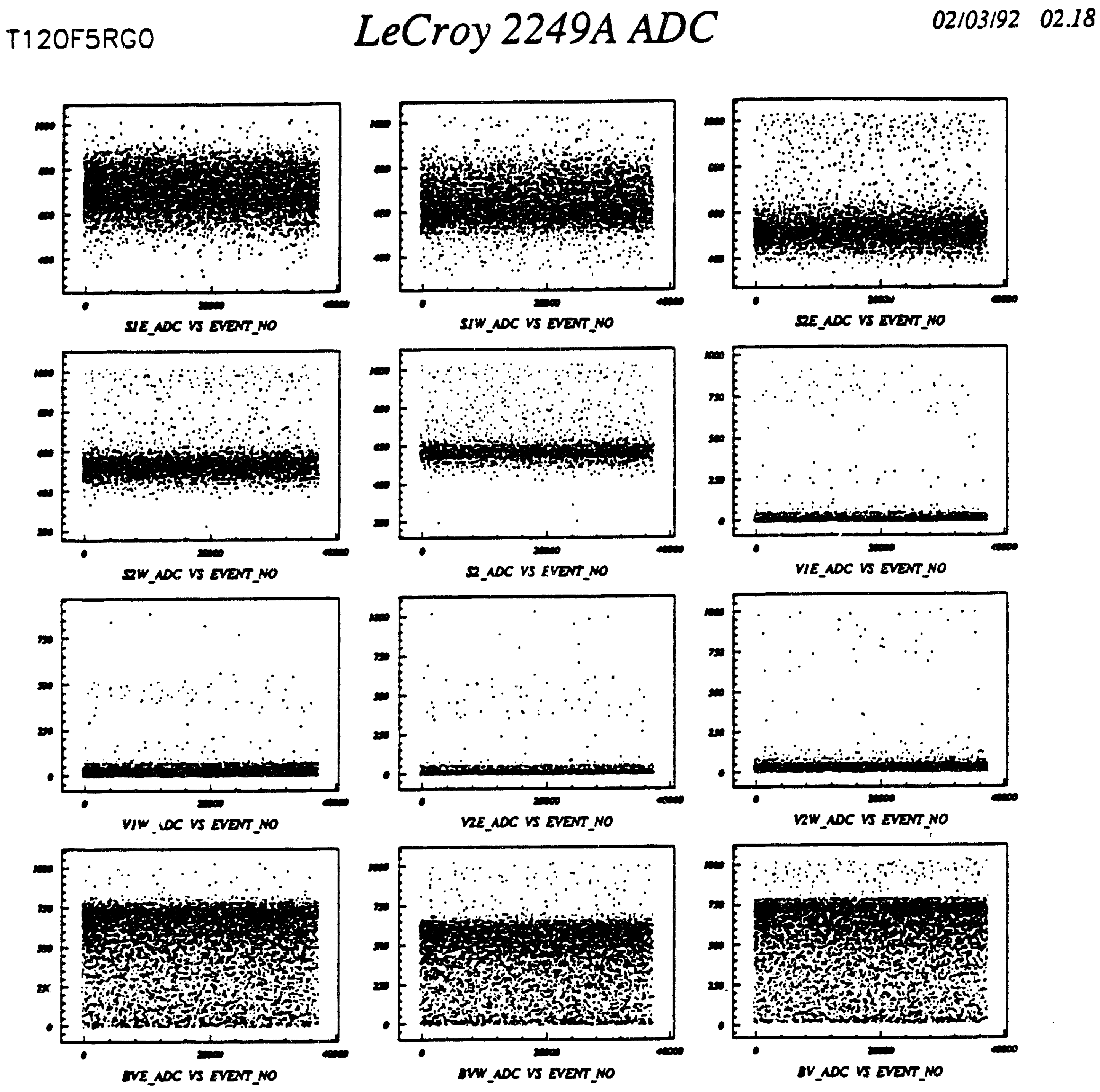

Figure 60. Normal run diagnostic plots for trigger scintillator ADCs.

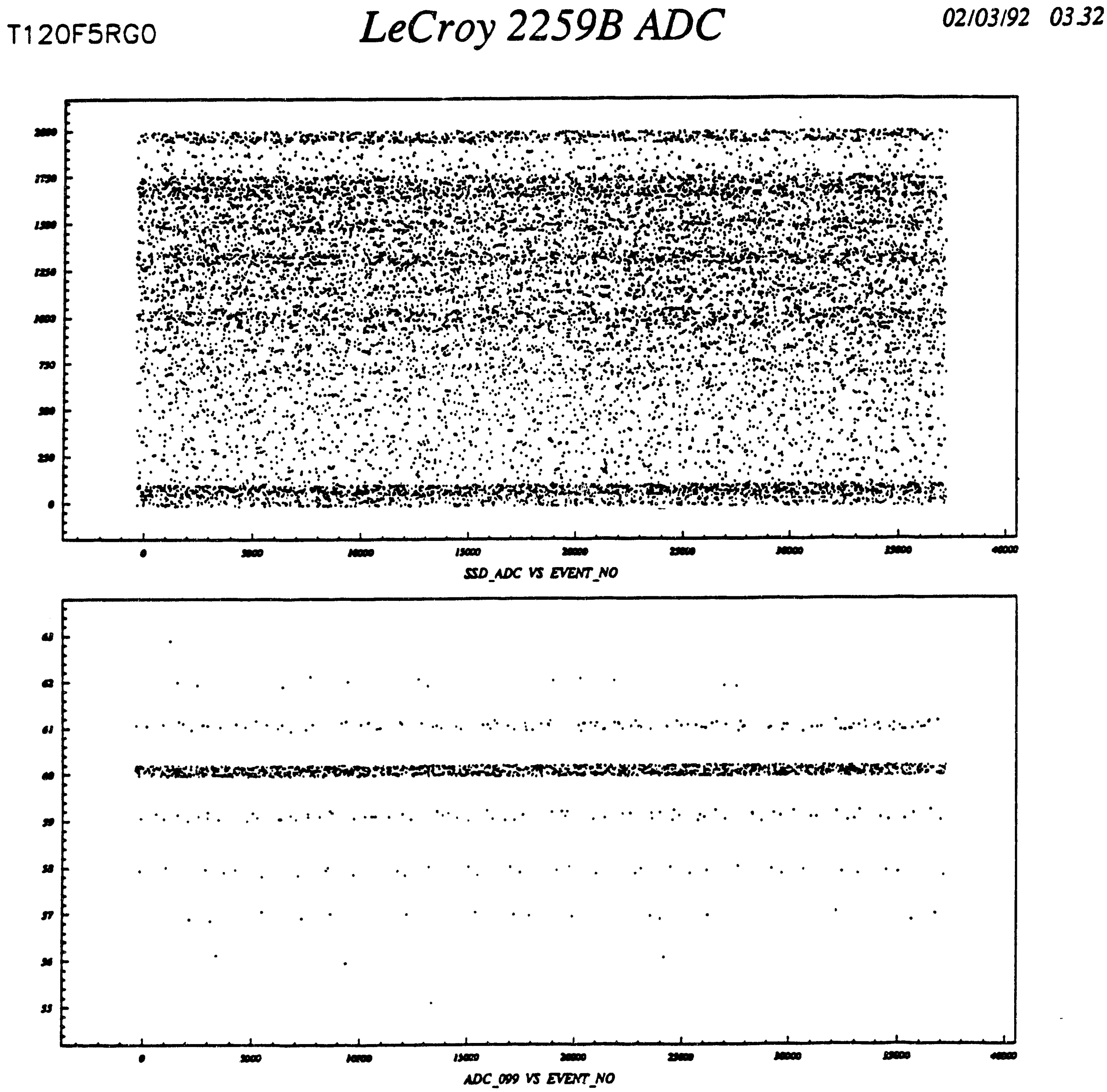

Figure 61. Normal run diagnostic plots for SSD detector ADC monitors.

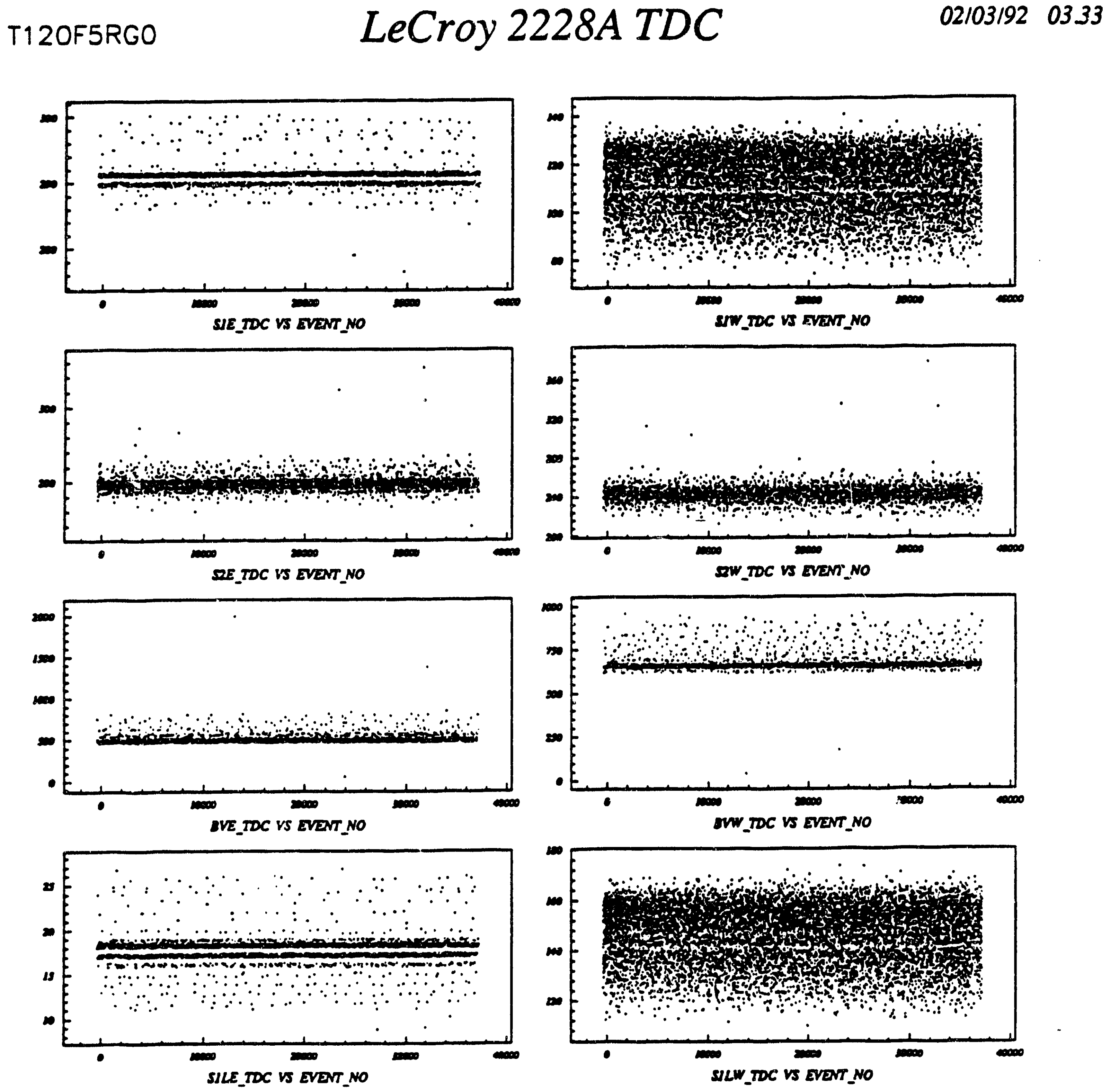

Figure 62. Normal run diagnostic plots for the trigger scintillator TDCs.

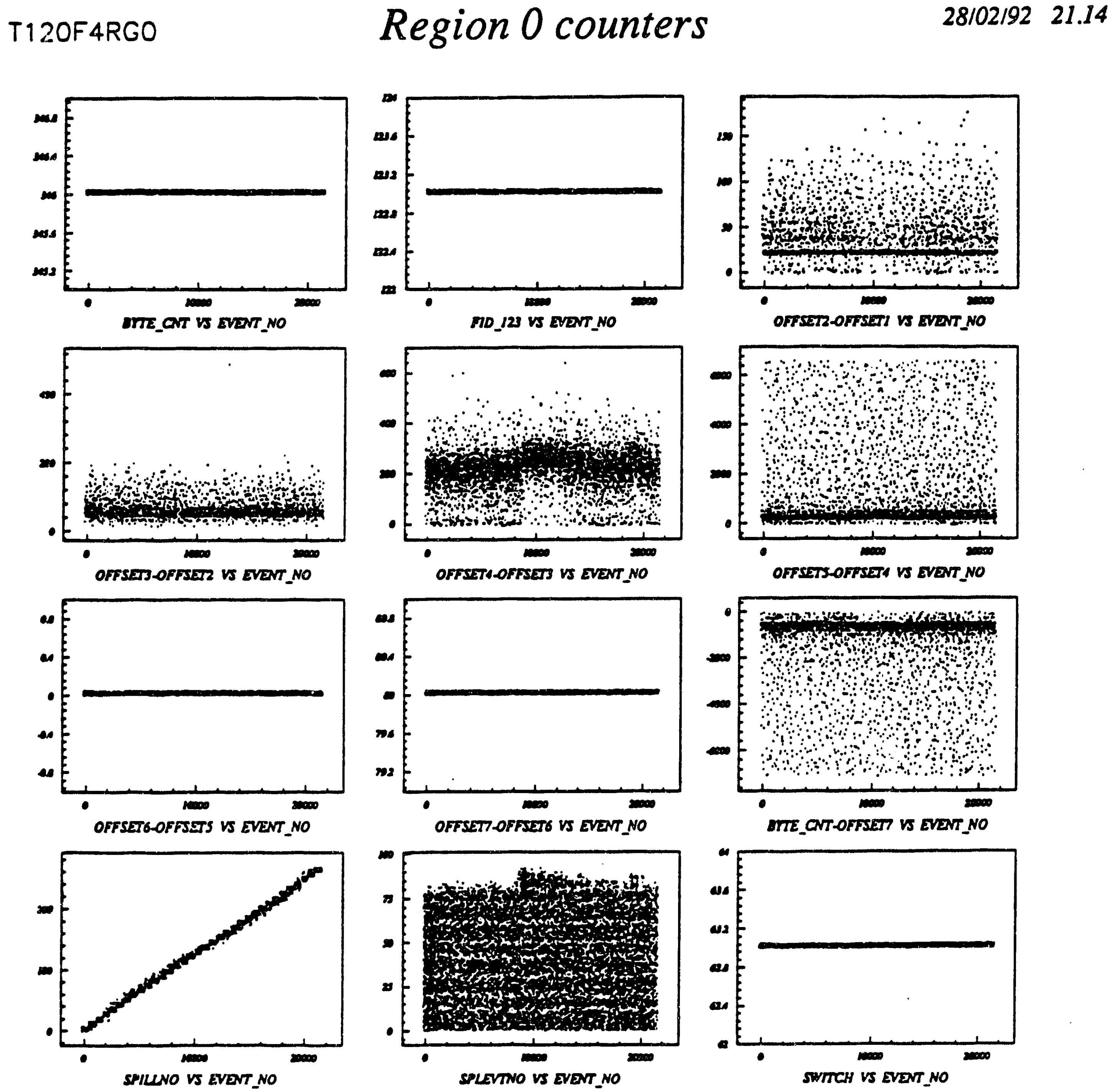

Figure 63. Abnormal run diagnostic plots for data stream monitors.

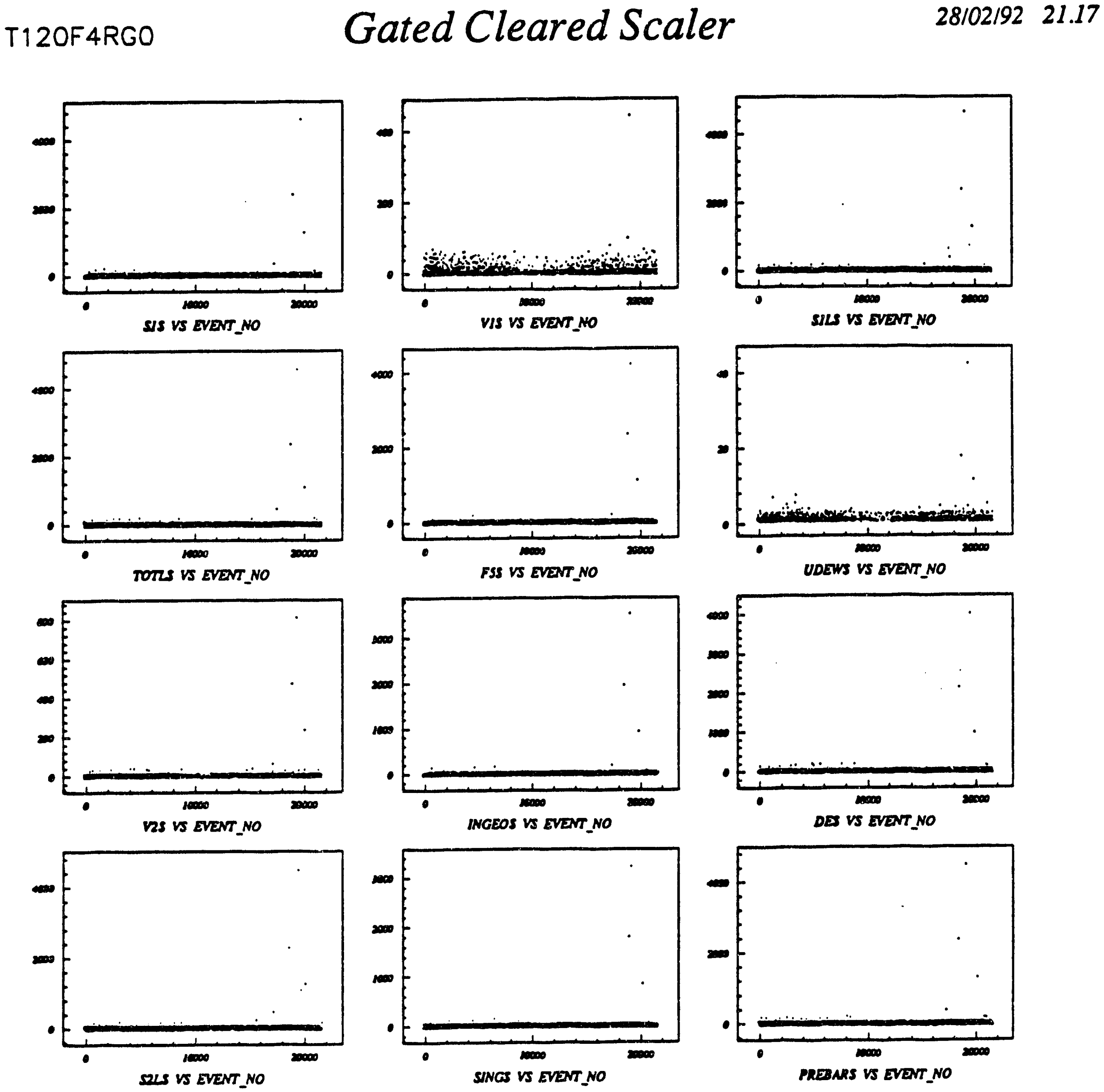

Figure 64. Abnormal run diagnostic plots for trigger scintillator scaler rates.

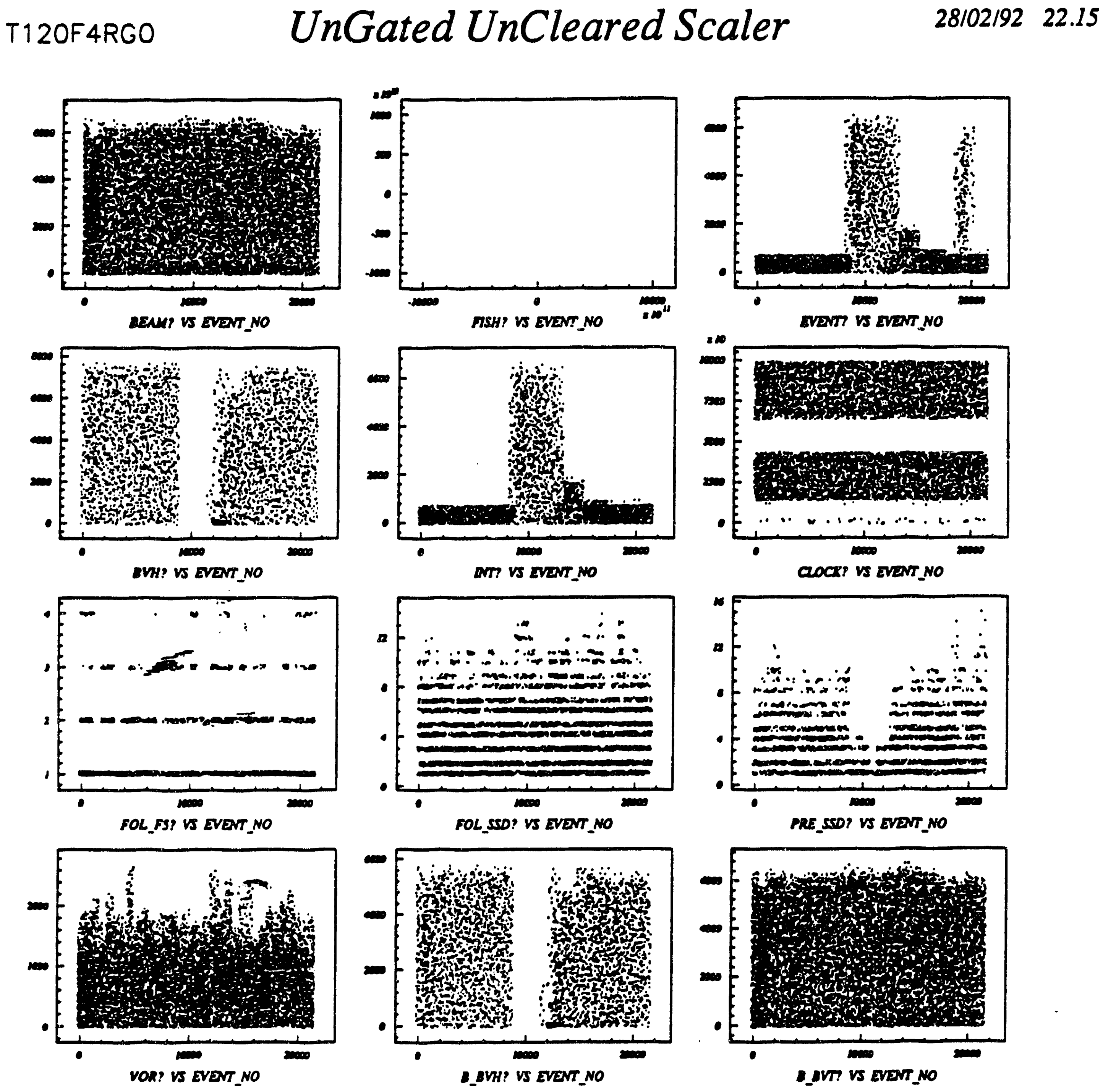

Figure 65. Abnormal run diagnostic plots for trigger logic monitoring rates.

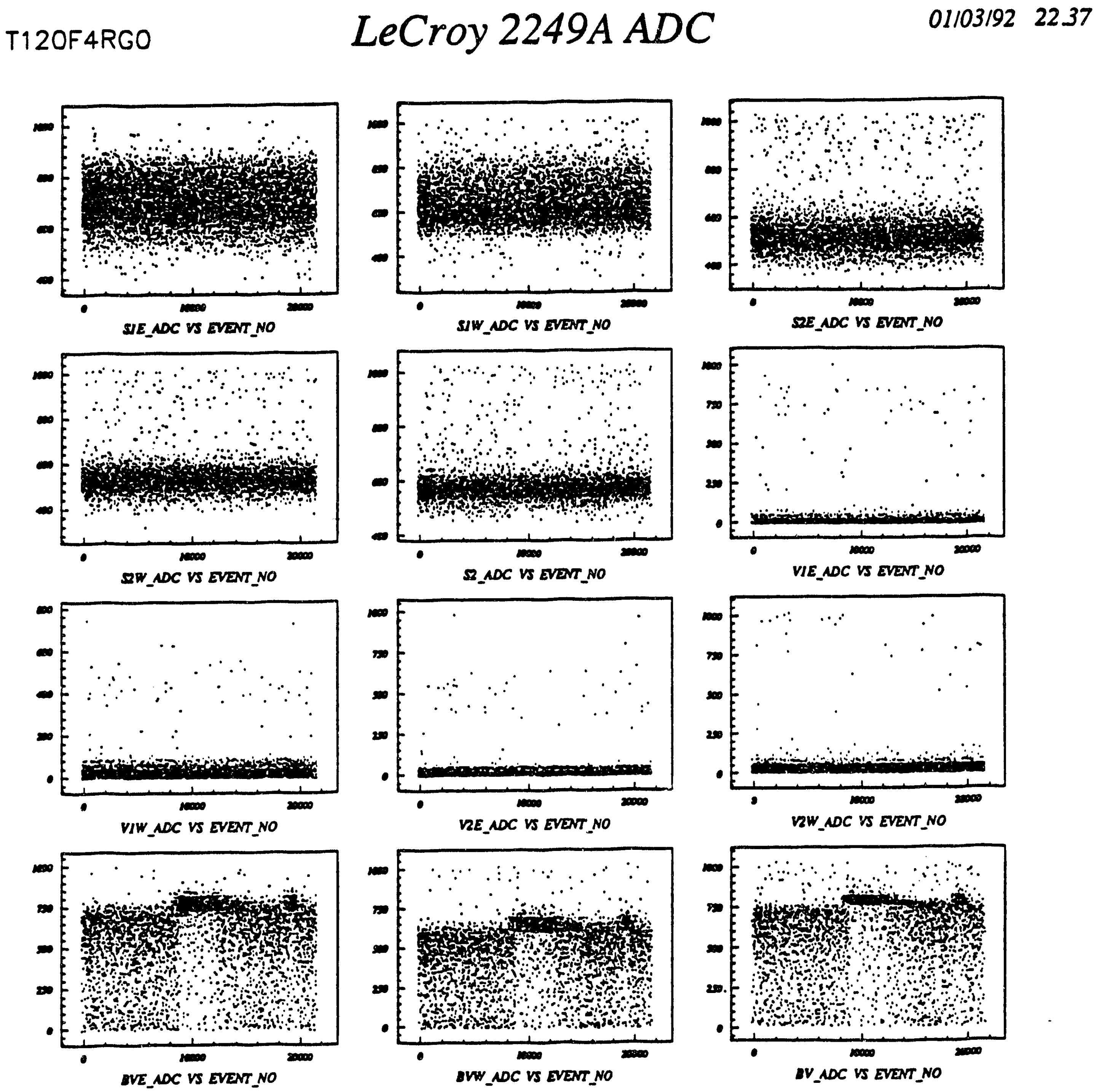

Figure 66. Abnormal run diagnostic plots for trigger scintillator ADCs.

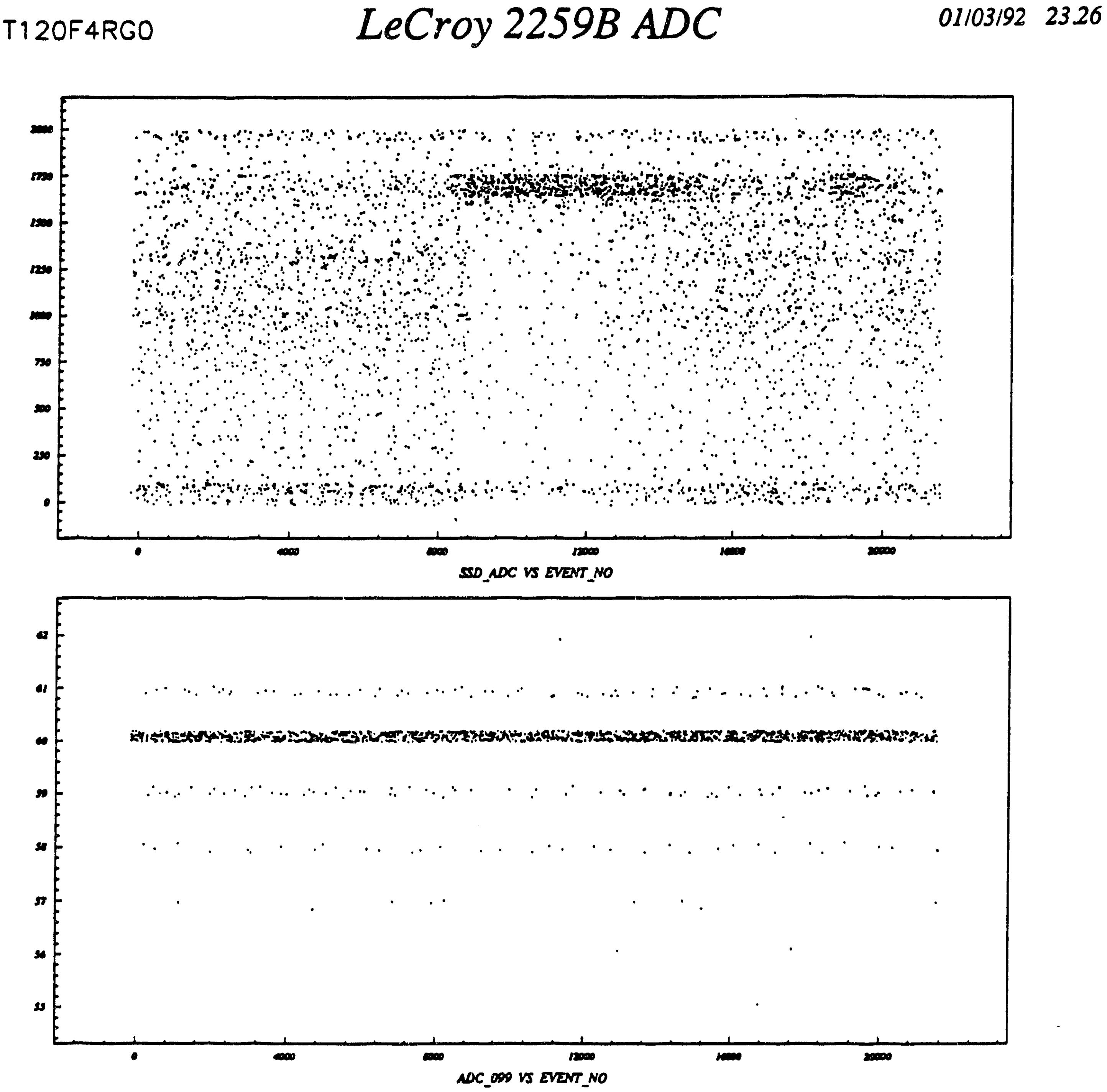

Figure 67. Abnormal run diagnostic plots for SSD detector ADC monitors.

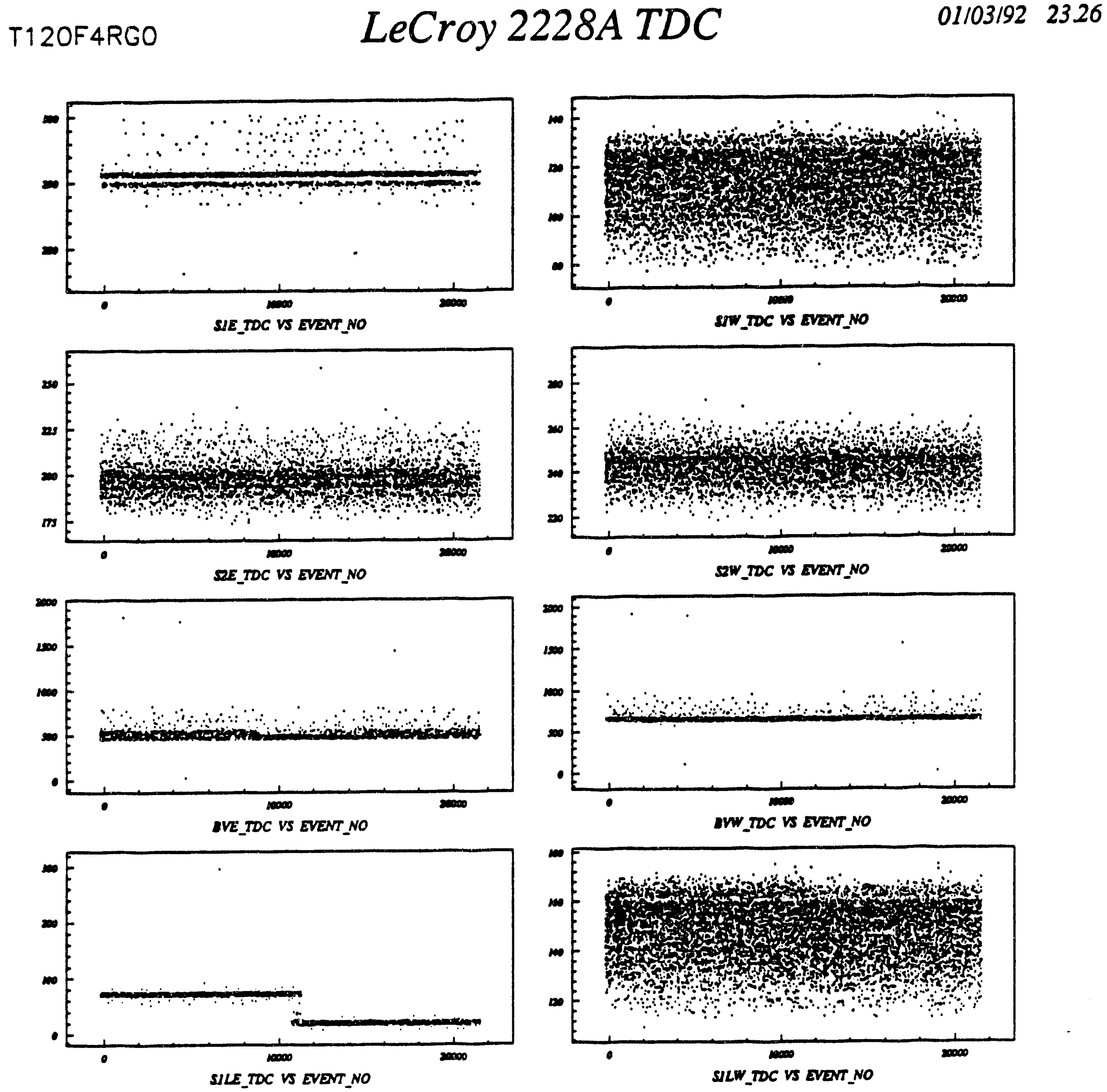

Figure 68. Abnormal run diagnostic plots for the trigger scintillator TDCs.

TABLE 5: Example Beam Definition Parameter File

```
    0.     , 0.       , 0.      , 0.       , !1!GOODFLAG
740.2429   , 52.6263  ,-2.750   , 2.750    , !2!<S1ADC>
11.6866    , 136.7111 ,-2.750   , 2.750    , !3!d(S1ADC)
581.4714   , 47.4012  ,-2.750   , 2.750    , !4!<S2ADC>
-87.985    , 45.9327  ,-2.750   , 2.750    , !5!d(S2ADC)
631.9143   , 53.9415  ,-2.750   , 2.750    , !6!S2E+S2W_ADC
21.7036    , 19.2721  ,-2.750   , 2.750    , !7!<V1ADC>
29.2043    , 31.0777  ,-2.750   , 2.750    , !8!<V2ADC>
0.2037     ,0.5048    ,-2.750   , 2.750    , !9!Mickey1_UP/DOWN
-0.1265    ,0.3259    ,-2.750   , 2.750    , !10!Mickey1_EAST/WEST
0.2635     ,0.3764    ,-2.750   , 2.750    , !11!Mickey2_UP/DOWN
-0.0633    ,0.1742    ,-2.750   , 2.750    , !12!Mickey2_EAST/WEST
189.35     , 5.2268   ,-2.750   , 2.750    , !13!<S1TDC>
185.6857   , 10.8058  ,-2.750   , 2.750    , !14!d(S1TDC)
211.6643   , 6.5163   ,-2.750   , 2.750    , !15!<S2TDC>
-31.9314   , 5.2034   ,-2.750   , 2.750    , !16!d(S2TDC)
    0.     ,-1.       , 1.      , 100000.  , !17!BEAM_Scaler
    0.     ,-1.       , 0.      , 1.       , !18!INT_Scaler
    1.     , 0.       , 1.      , 1.       , !19!EVENT_Scaler
    0.     ,-1.       , 0.      , 1.       , !20!F5/TOTL
    0.     ,-1.       , 0.      , 1.       , !21!BEAM/F5
    0.     ,-1.       , 0.      , 1.       , !22!INT/BEAM
    0.     , 0.       , 0.      , 0.       , !23!Followed F5
    0.     , 0.       , 0.      , 0.       , !24!Followed SSD
    0.     , 0.       , 0.      , 0.       , !25!Preceeded SSD
```

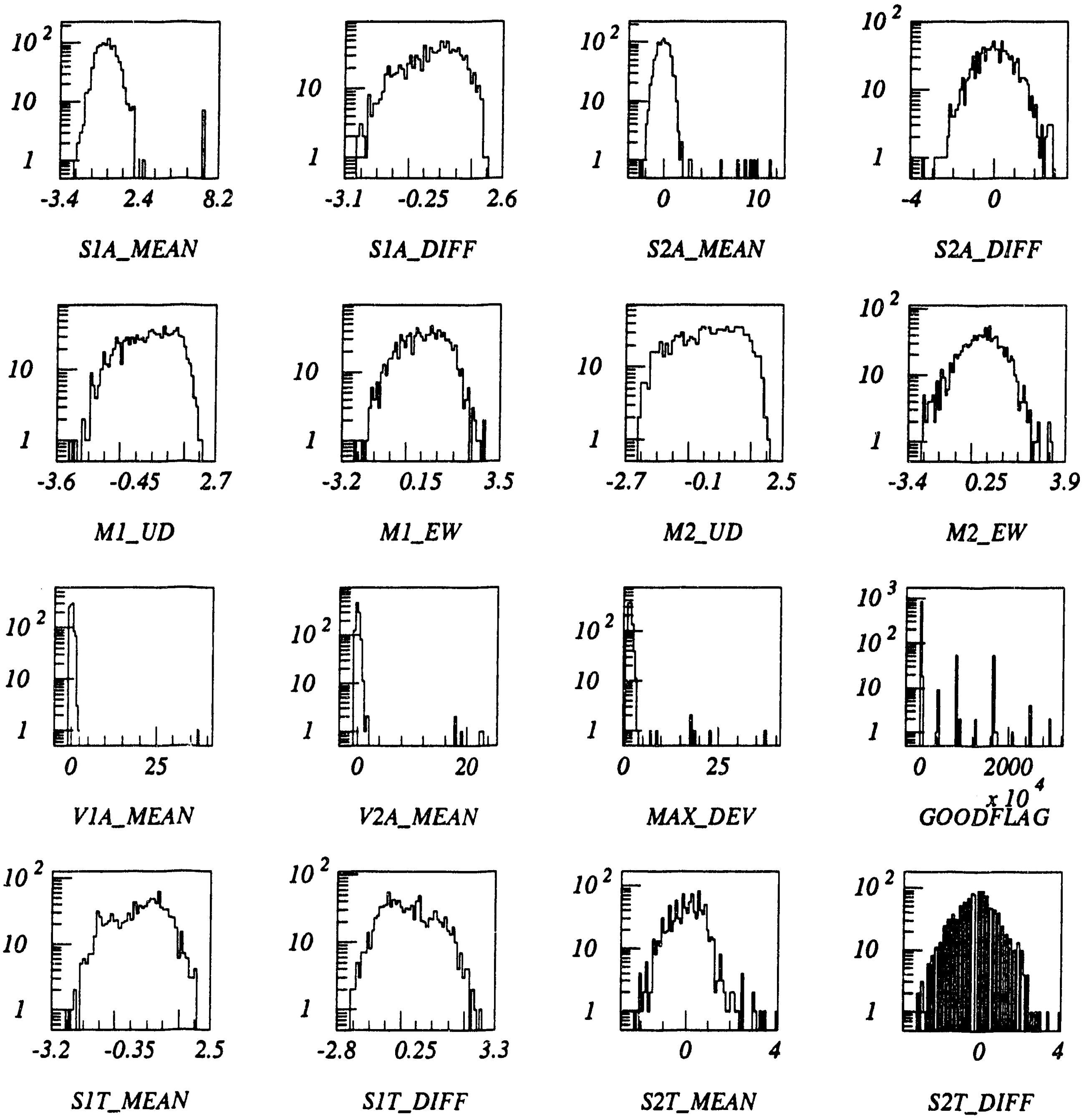

Figure 69. Uncut Beam Definition histograms.

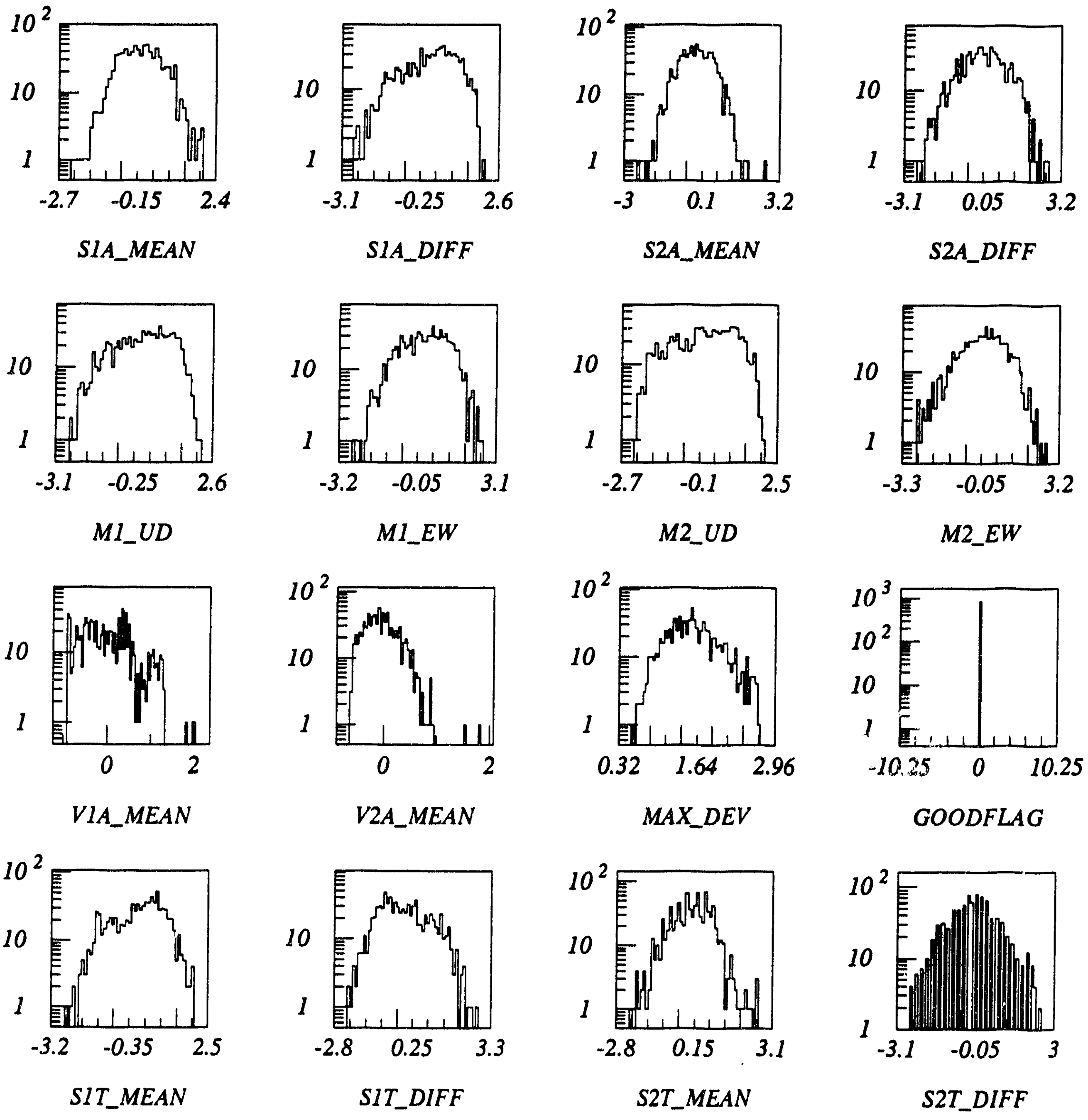

Figure 70. Beam Definition histogram restricted to 2.75 σ

"nominal" value). If the resultant cross section were to show a significant dependence on the cut tightness, we would conclude that there is an effect we are overlooking.

As a final check of the quality of our cross sections results, we check the internal consistency of our various types of cross section measurements. The measurements of total charge changing cross section, elemental production cross sections, and isotopic production cross sections for a particular beam are arrived at by different calculational paths. The sum of all measured elemental production cross sections should show consistency with the total charge changing cross section for each beam. Likewise, the sum of all measured isotopic production cross sections for a particular element should show consistency with the elemental production cross section for that element for each beam.

Although there are many potential problems to which these internal consistency checks are completely insensitive, they do provide a check of the validity of many other steps in the cross section calculations.

4. Current Cross Section Results

In Figure 71 the charge changing total cross sections from the HISS experiment (filled circles) are shown as a function of energy for two neutron rich species, ^{22}Ne (panel A) and ^{26}Mg (panel B), and two neutron balanced ($A/Z = 2$) species, ^{32}S (panel C) and ^{40}Ca (panel D). The statistical counting uncertainties, represented by the heights of the filled symbols, are on the order of 0.5-1%. However, due to the nature of total cross section calculation (large number subtraction), the propagated measurement uncertainty is actually between 10-15% (shown in Figure 3 as the error bars) and is comparable to experiments with similar counting statistics. Also included in the final uncertainties are ~4% systematics such as the uncertainty in the target thickness calculation. Our data can be compared to the measurements of Webber et al.[27] (open circles), and the agreement is quite good. Also shown are semi-empirical predictions by Letaw et al.[28] (dotted line) and the formulation of Garcia-Munoz et al.[11] (solid line) which uses the energy dependence of Karol[29] combined with a fit to a compilation of (p,p) and (p,n) total cross sections. Both formulas actually calculate the $\sigma(\Delta A)$ total cross section, so to compare with the $\sigma(\Delta Z \geq 1)$ measurements the neutron stripping cross sections calculated from Silberberg and Tsao[26] have been subtracted from the predictions. The experimental data agree with calculated cross sections quite well, with the Garcia-Munoz et al. predictions giving a slightly better fit to the 400 MeV/nucleon data. There also appears to be a trend, though with low significance, for the neutron rich beams to be below the predictions while the neutron balanced species have a better fit. In panel D we also include $\sigma(\Delta Z \geq 1)$ for ^{40}Ar at 400 MeV/nucleon (filled triangle) from this experiment (slightly shifted in energy to clarify the plot). It is clear that even though both ^{40}Ca and ^{40}Ar have the same mass, the neutron rich ^{40}Ar shows a smaller charge changing total cross section. These charge changing total cross sections also appear to be organized by $(A_{beam})^{2/3}$, a form implied by the Bradt and Peters model.[73] This is indicated in Figure 72 for the three energies 393-400 MeV/nucleon (open and filled circles), 600 MeV/nucleon (open triangles), and 800-910 MeV/nucleon (filled squares). (Note that the data with identical beam mass have been shifted slightly in order to clarify the figure). The results for similar energy display a linear dependence on $(A_{beam})^{2/3}$. For 400 MeV/nucleon data we also distinguish neutron rich (open circles) from the rest (filled circles), and these appear to form two slightly separated groups, with the neutron rich species showing lower cross sections with respect to the overall fitted line. This implies that charge changing total cross sections depend not only on total mass but also on the neutron/proton ratio of the projectile.

Figure 73 compares the measured charge changing elemental production cross sections with those calculated by Webber et al (left) and Silberberg and Tsao (right). It can be seen that the Webber et al. representation does organize the data in a more consistent manner than Silberberg

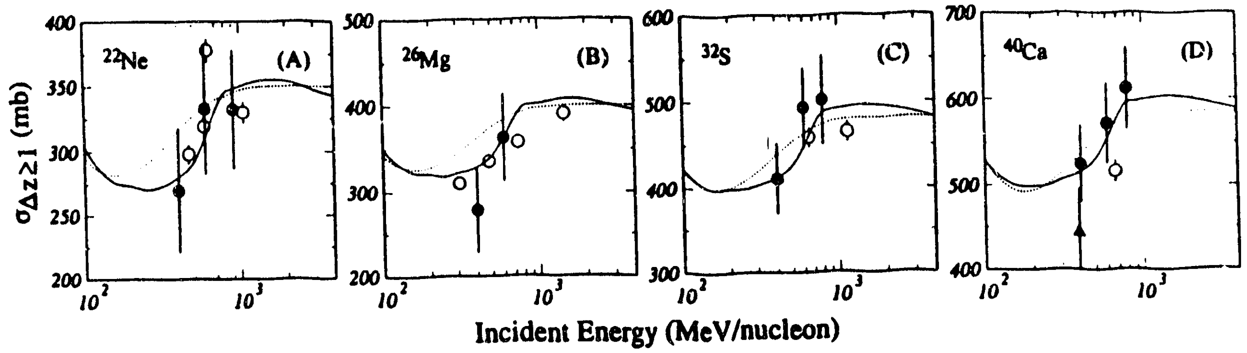

Figure 71. Total charge changing cross sections as a function of energy.

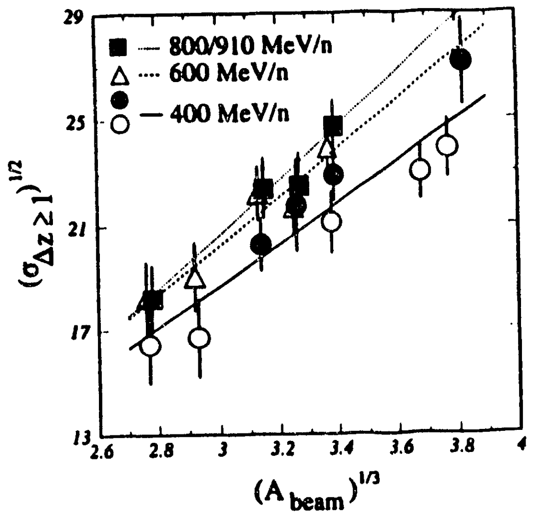

Figure 72. Mass dependence of total charge changing cross sections at different energies

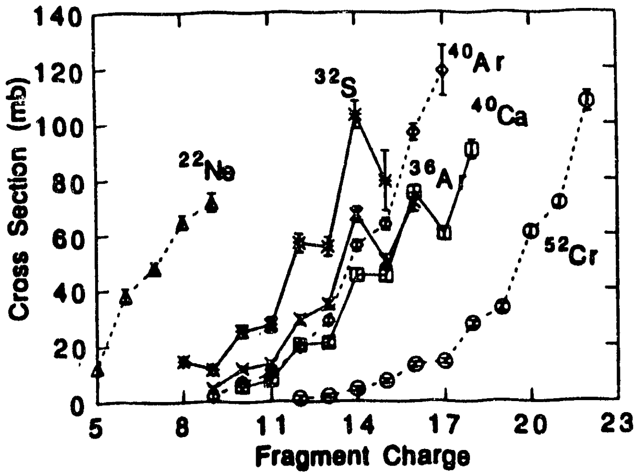

Figure 74. Elemental production cross sections.

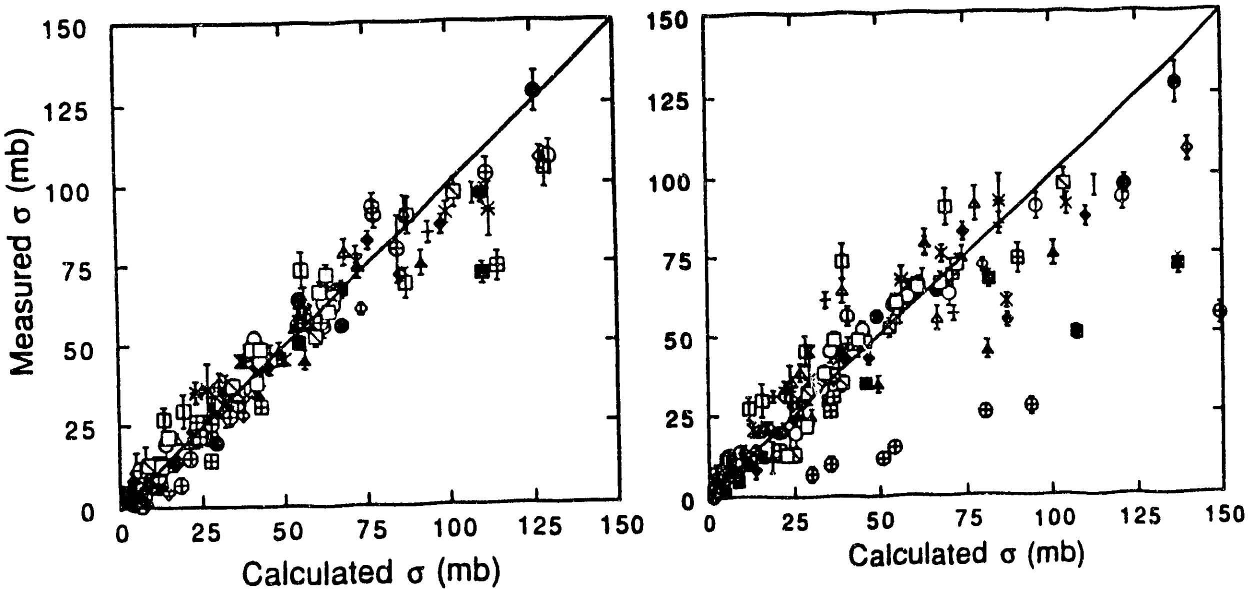

Figure 73. Comparison between measured and calculated elemental cross sections of Webber et. al. (left) and Silberberg and Tsao (right).

and Tsao, even though both representations still show a significant spread between the calculations and the measurements. Figure 74 shows elemental cross sections as a function of the fragment charge for six of the ~400 MeV/nucleon beams: three are neutron balanced (^{32}S, ^{36}Ar, ^{40}Ca) and three are neutron rich (^{22}Ne, ^{40}Ar, ^{52}Cr). The significant feature of this plot is that the neutron balanced beams show strong odd-even variations, whereas neutron rich beams show little or no odd-even effect. The different behavior between neutron rich and neutron balanced species, as seen in charge changing total and elemental cross sections, strongly suggests that the neutron/proton ratio plays a significant role in the fragmentation of these nuclei at these energies. Any model that attempts to predict these cross ections must take this into account. The odd-even effects of elemental cross sections would be enhanced during cosmic ray propagation due to isotope decay, since more of the odd charge isotopes will tend to be unstable.

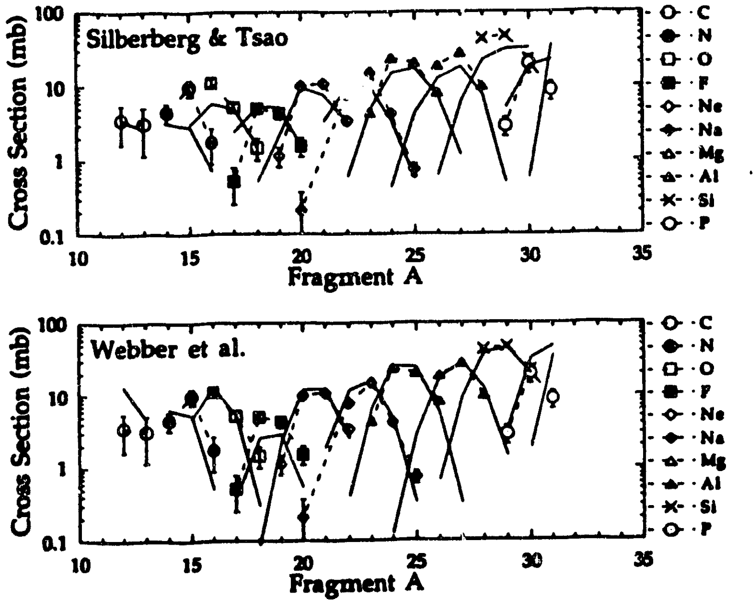

Figure 75. Isotopic production cross sections from experiment (dotted lines and points) and theory (solid lines for 400 MeV/n ^{32}S beam on liquid hydrogen.

The preliminary mass changing cross sections for the 400 MeV/nucleon ^{32}S beam are shown in Figure 75 for fragments from C to P. These cross sections have an uncertainty of 10% - 15% that include errors in determining the effective thickness of the liquid hydrogen target, detector efficiencies, acceptance interactions in the detectors downstream of the HISS magnet, and statistics. Also in Figure 75 are dashed lines grouping the cross section measurements for each element together and solid curves representing the predictions of Silberberg and Tsao (top panel) and those of Webber et al. (bottom panel). While both formulations reproduce the general systematic trends, Webber et al. is in better agreement with our results. In fact, the average variance between the Silberberg and Tsao calculated values and the measurements is 40% while that for the Webber formula is 20%. Currently, we are finalizing the analysis of the isotopic cross sections for 400 and 600 MeV/nucleon ^{32}S beams and are beginning to work on the 800 MeV/nucleon ^{32}S data. As this analysis continues, we will be able to investigate the energy dependence and other systematics of the isotopic cross sections and begin identifying methods for improving cross section prediction formulae.

C. B40 ANALYSIS

The low energy B40 work is significantly different from the HISS analysis. The datasets are still large, but there are fewer of things and the analysis is concentrated at one or two institutes. Thus, we can perform a more traditional analysis since the number of interfaces involved is small.

1. Analysis Flow.

The overall analysis plan for our experiments is outlined in Figure 76. At B40, we measure the angular distribution for each isotope and the energy of each particle (since the events are brought to rest). This provides the longitudinal momentum distribution as a first product once the mass analysis is complete. The transverse momentum is derived from the angular distributions which must be determined before the full isotopic cross sections can be obtained. This total information then allows both nuclear science and astrophysics objectives to be realized. Analyzing an inclusive experiment from B40 involved three major tasks: (a) absolute calibration of the trajectory subsystem, (b) calibration of the energy loss detectors to obtain mass resolution, and (c) beam monitoring and normalization. Following initial data processing to remove spurious data, extra EOF's, scrambled events and other problems introduced by the front end data acquisition system, and tape copying, to provide the full dataset to all members of the collaboration, analysis proceeds on these three areas essentially in parallel.

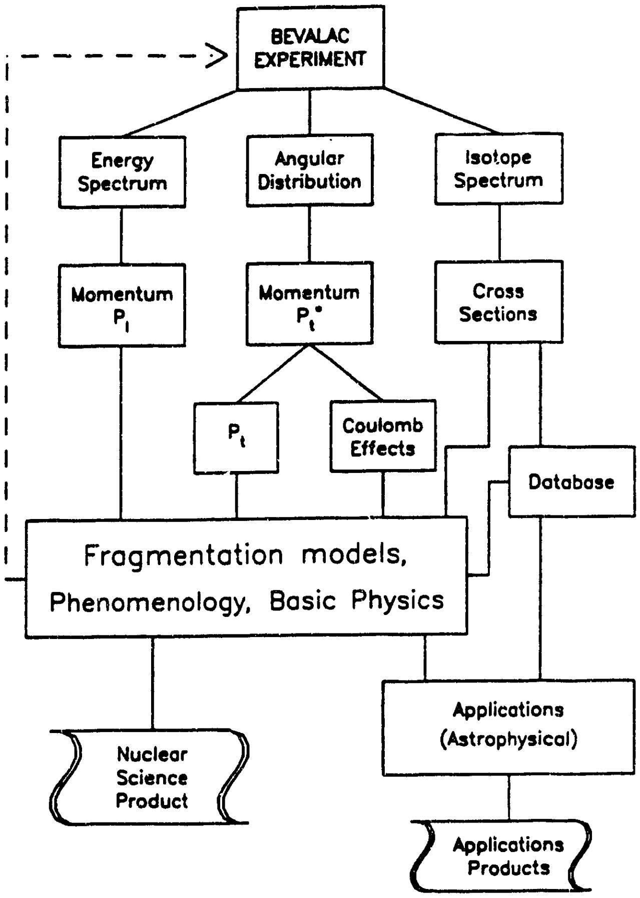

Figure 76. Analysis path for B40 experiments.

2. Detector Calibrations.

The calibration of the solid state detector telescope involves both pulser and fragment data. The goal for the SCOPE detectors is to convert channels into energy deposits and then into charge, mass and energy. There are, typically, 20-30 detectors in the SCOPE, each requiring a calibration to better that a few percent in order to obtain isotope resolution. In addition, this calibration must be redone for every new experiment since the detectors, pre-amps, shaping amps and ADC's (all pool equipment) must returned for every beam-energy point. This calibration has been completed for all of the B40 runs giving, for ^{16}O, excellent resolution down to the Li isotopes and, for ^{28}Si, resolution down to Boron. This is illustrated in Figure 76 which shows the mass histogram from the Mg isotopes for the ^{28}Si dataset

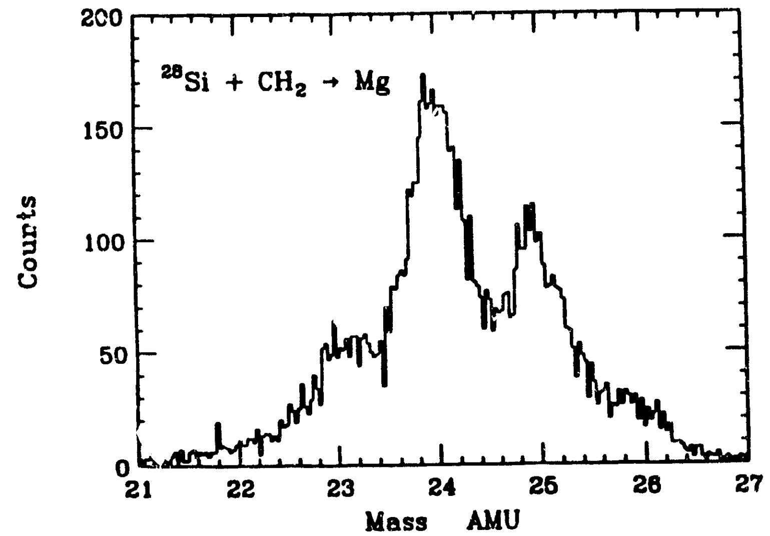

Figure 77. Mass histogram from Mg at 1.5°.

The basic approach here is the energy loss-residual energy technique. Taking the energy in the last detector triggered (the stopping detector) and plotting the previous detector versus the stopping detector yields ΔE-E plots such as is illustrated in Figure 78 for D7 vs D8 for the ^{28}Si run. Note the band of points for three charges that are visible. Within each band, the points separate into several lines which are the individual isotope "tracks". Summing events perpendicular to these tracks gives the mass histograms and the isotopic identifications. Since the difference in signal between two adjacent isotopes is small, the detector calibrations must be as accurate as possible. For the trajectory subsystem, the goal is to calibrate the detector in terms of the actual position relative to

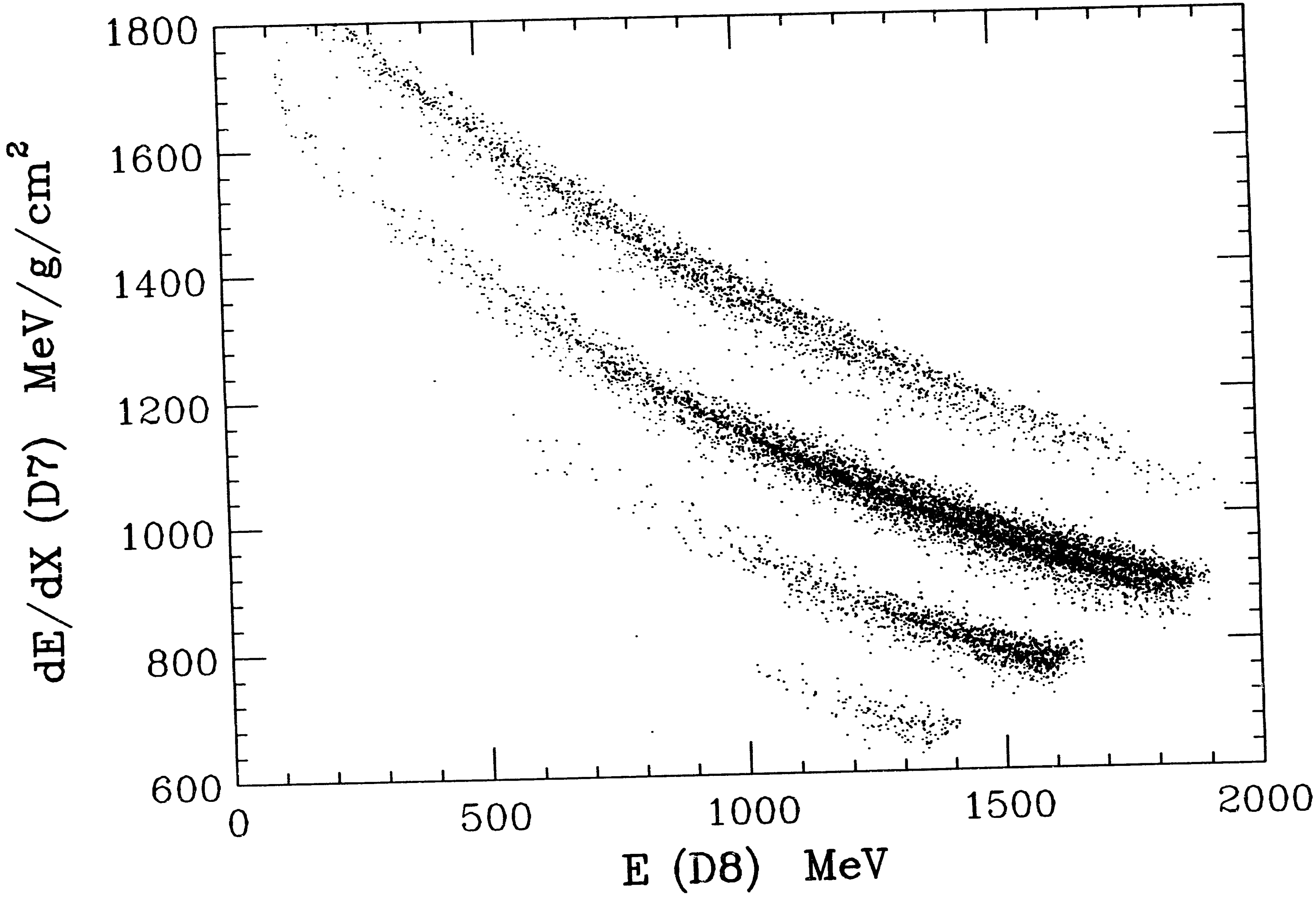

Figure 78. ΔE-E matrix for D7 vs D8 for the ^{28}Si dataset.

he SCOPE centerline. Here more than pulsers and beam events are required, and we developed several absolute calibration devices; a brass plate with precision matching holes, an X-Y grid of matched brass absorbers, and an array of fiber scintillators (precision mounted) that could be used to provide a trigger for the readout system. For the CPSD's a position of <500 μm was obtained while for the drift chamber the position resolution was 200 μm in the x (drift) coordinate and 400 μm in the y (vertical) direction.

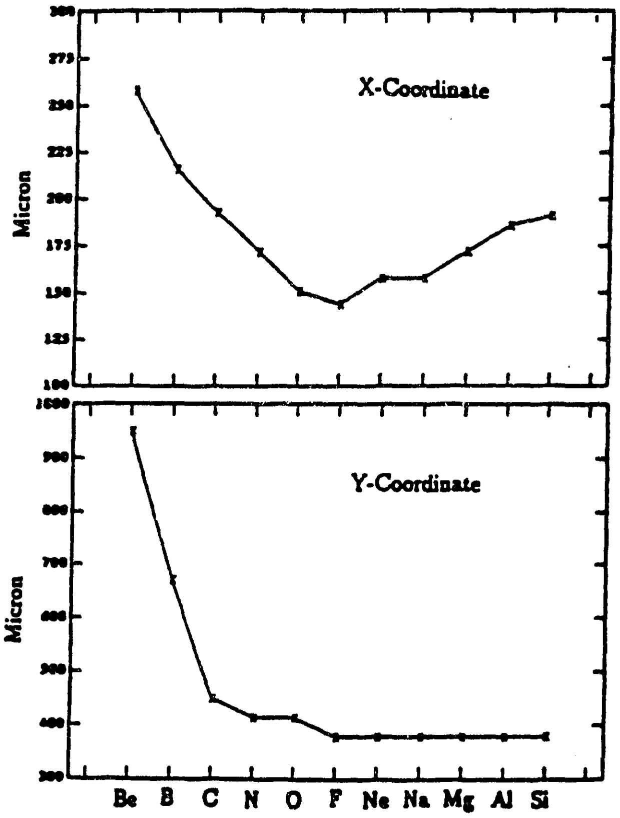

Figure 79. Position resolution versus charge.

Unfortunately, a DC is sensitive to space charge effects, and at high rates, the chamber does not fully clear the space charge before the next particle appears. This leads to a rate dependent correction to the position which must be applied particle-by-particle within the spill since the spill structure for our run showed an order of magnitude change in beam intensity during the ~1 second spill period. With these effects incorporated, the DC resolution as a function of particle charge is shown in Figure 79. Due to the limitations of dynamic range, the DC performance can be optimized for a given signal size and then shows reduced resolution at both larger and smaller signals. For F-Ne we achieved the best coordinate resolution of ~150 μm, with the resolution for all the major fragments remaining below 200 μm.

3. Data Selection and Normalization

The third step in the analysis involves beam effects and normalization. It is necessary to eliminate background, remove periods of bad beam quality or beam stability, eliminate event pile-up, correct rate dependent effects, and restrict the acceptance of the telescope. The remaining events (typically 30-40% of the total) are used to form charge, mass and energy histograms from which the quality of the initial calibrations can be determined. If necessary, the PSD and energy detector calibrations are refined, and the entire process is repeated until the best is obtained.

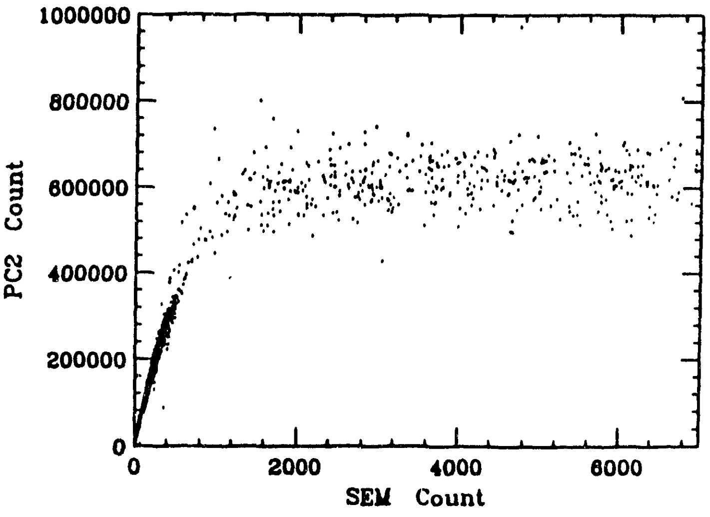

Figure 80. SEM count versus PC2 beam count.

In order to determine the angular distributions and the cross sections, each separate angle measured must be normalized. This involves calibrating the SEM system, understanding the spill structure and scalers recorded (event by event and spill integrated). Correlations of many parameters are examined and, gradually, an understanding of the behavior of the beam during the experiment is developed. This normalization is then used to correct each angle's information appropriately.

An example of the SEM calibration for the ^{28}Si dataset is shown in Figure 80. Referring to the experimental arrangement for B40, the two scintillators PC1 and PC2 are in the cave just behind the rail along the beam line. They are viewed by the Secondary Emission monitors, mounted at an angle to the scintillators, but out of the direct beam. PC1-2 start to saturate at a few times 10^5 counts/second, but larger beam rates were required to obtain the experimental data. Therefore, we fit the linear portion of the curve and use that calibration to determine a "pseudo-PC12" count for SEM rates beyond 400-500. Thus allows the high rate data runs to be normalized to the low rate runs to determine the overall angular distribution.

Next, the number of fragments per beam particle, integrated over the full solid angle, is obtained. An example, for the isotope ^{24}Mg is shown in Figure 81 for the CH_2, C, and target out runs at 10 separate angle positions of the SCOPE along the B40 rail. Integration under these curves, subtraction of the C from the CH_2 and correction for the target out background differences then yields the cross sections for a hydrogen target. Note that the "power" in the distribution is at small angles 0.5-1°, but that the tails at larger angles cannot be neglected if accurate cross sections are to be obtained. For lighter fragments, the "power" shifts to larger angles, making the large angle runs even more important. What determines the experimental limitation is the total fragment statistics and the normalization to the correct number of incident beam particles. The latter provides the largest uncertainty at the large angles where the indirect SEM normalization technique must be used. Fortunately, at low angles, where most of the "power" is located, direct beam counting is employed.

4. Results.

The procedures just described can also be used to determine the elemental cross sections. For the ^{28}Si run at 245 MeV/nucleon, a comparison of the elemental cross section for H and C targets is shown in Figure 82 with the top plot giving the measured values and the lower plot showing the ratio, H/C. There is a pronounced odd-even effect in the elemental cross sections for both nucleon and nucleus targets, but the interesting results is the scaling. The cross section ratio varies from about 0.1 to 0.8 showing that the mass yield curves are different for the two targets at these energies.

Isotopic cross sections have been obtained for 48 fragment nuclides from ^{28}Si interactions in both H and C targets. Most of these have never been measured before. Table 6 gives our measured values and the uncertainty. The errors have been propagated through all steps of the calculation and include statistical errors as well as errors due to fluctuations of beam conditions determined by measuring the same angle and target several times. Systematic errors due to interactions in the SCOPE were also included.

Previous work involved mainly proton irradiation of silicon with radioactive fragment yields determined by β–γ counting techniques. We showed above the comparison of our data to previous work for ^{26}Al production. Figure 83 provides a similar comparison for the production of ^{22}Ne and ^{18}F, in both cases compared to the model predictions.[26,27] The agreement with previous data is good, but the model predictions are , again, not a good representation of the actual measurements. Additional work on the excitation functions is needed.

The isotope ^{22}Ne has been most widely studied as a normalization nuclide for irradiation experiments. Relative to the previous data, our point appear to be high by about two standard deviations. For ^{18}F, however, our result is on the low side compared to the previous work. The ^{22}Ne, in particular, has prompted us to recheck the run by run normalization to see if there is any uncertainty that might lead to an elevated value. This re-evaluation is in progress, and upon its completion we will be in a position to release the values in Table 6 in a manuscript.

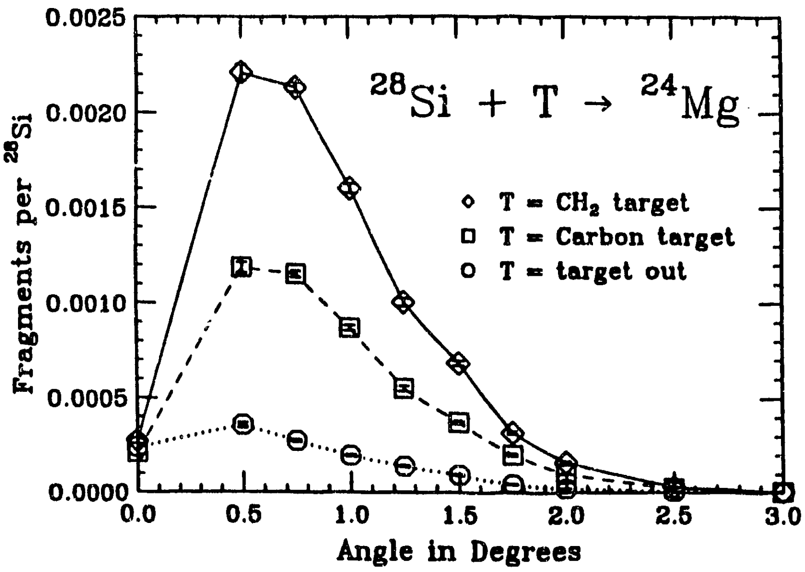

Figure 81. Angular distribution for ^{24}Mg.

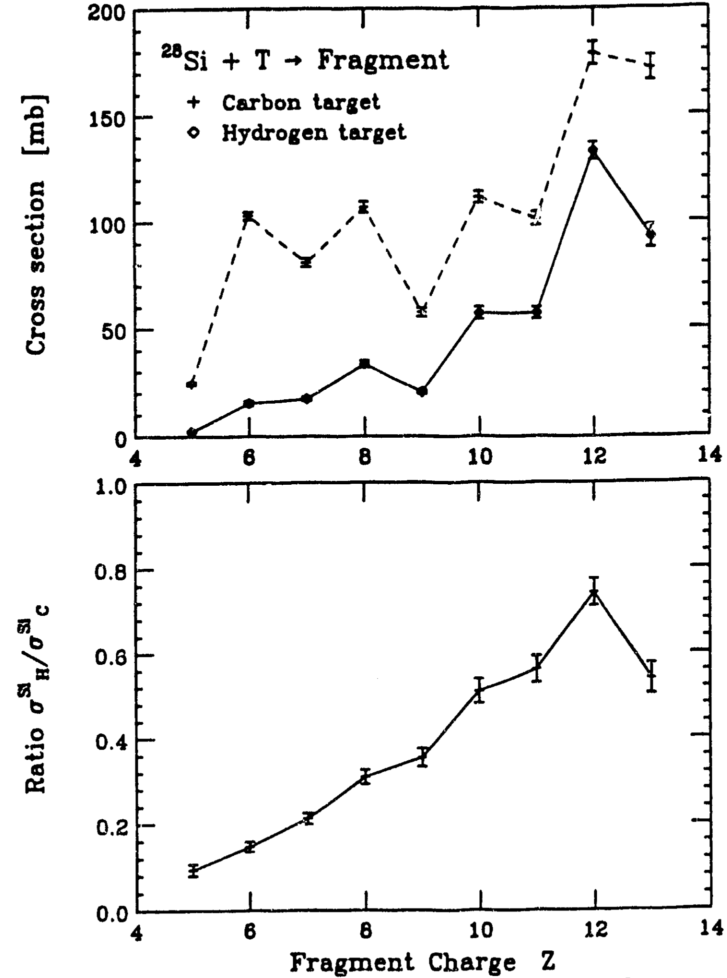

Figure 82. Charge changing cross sections for ^{28}Si on H and C targets (top) and the cross section ratio (bottom).

TABLE 6: Cross sections from ^{28}Si fragmentation at 245 MeV/nucleon

Fragment Isotope	Hydrogen		Carbon	
	Cross Section (mb)	Error (mb)	Cross Section (mb)	Error (mb)
^{28}Al	2.7	0.5	14.8	2.0
^{27}Al	27.6	3.0	54.8	3.0
^{26}Al	38.1	3.5	65.3	3.2
^{25}Al	17.7	3.0	27.3	2.5
^{24}Al	6.7	2.0	9.8	2.0
^{27}Mg	1.7	0.9	4.1	0.9
^{26}Mg	12.8	1.2	18.1	2.0
^{25}Mg	36.5	2.0	51.4	2.8
^{24}Mg	47.7	2.2	59.1	3.0
^{23}Mg	22.4	2.0	27.4	2.2
^{22}Mg	6.3	1.3	9.5	1.2
^{24}Na	6.3	0.9	11.8	1.2
^{23}Na	20.4	1.5	40.3	1.9
^{22}Na	21.2	1.6	35.1	1.8
^{21}Na	8.1	1.2	13.5	1.3
^{23}Ne	1.2	0.4	2.5	0.5
^{22}Ne	6.8	0.9	13.8	1.0
^{21}Ne	16.9	1.3	35.4	1.4
^{20}Ne	21.5	1.8	40.8	1.5
^{19}Ne	7.4	1.2	12.7	1.2
^{18}Ne	2.2	1.0	3.6	0.6
^{20}F	2.1	0.4	5.9	0.7
^{19}F	5.9	0.5	16.1	1.0
^{18}F	8.3	0.6	20.6	1.1
^{17}F	3.6	0.4	9.7	0.9
^{16}F	0.8	0.3	2.1	0.4
^{15}F	0.3	0.1	0.9	0.2
^{19}O	0.3	0.1	1.3	0.2
^{18}O	1.4	0.4	5.7	0.4
^{17}O	5.6	0.6	17.5	0.9
^{16}O	16.7	1.1	45.7	2.1
^{15}O	7.6	0.8	23.3	1.1
^{14}O	1.9	0.5	5.3	0.5

TABLE 6: Cross sections from ^{28}Si fragmentation at 245 MeV/nucleon (continued)

Fragment Isotope	Hydrogen		Carbon	
	Cross Section (mb)	Error (mb)	Cross Section (mb)	Error (mb)
^{17}N	0.4	0.2	1.5	0.2
^{16}N	1.0	0.3	3.5	0.3
^{15}N	7.2	0.6	30.4	1.2
^{14}N	7.2	0.6	30.0	1.2
^{13}N	1.6	0.3	9.7	0.8
^{12}N	0.26	0.12	2.6	0.3
^{15}C	0.2	0.1	1.1	0.2
^{14}C	0.8	0.3	5.7	0.3
^{13}C	4.2	0.5	23.3	0.8
^{12}C	7.7	0.6	45.2	1.3
^{11}C	2.5	0.8	18.5	0.8
^{10}C	0.6	0.3	3.7	0.4
^{12}B	0.1	0.08	1.3	0.2
^{11}B	0.26	0.1	2.9	0.3
^{10}B	2.0	0.3	19.0	0.7
^{8}B	0.19	0.1	2.0	1.0

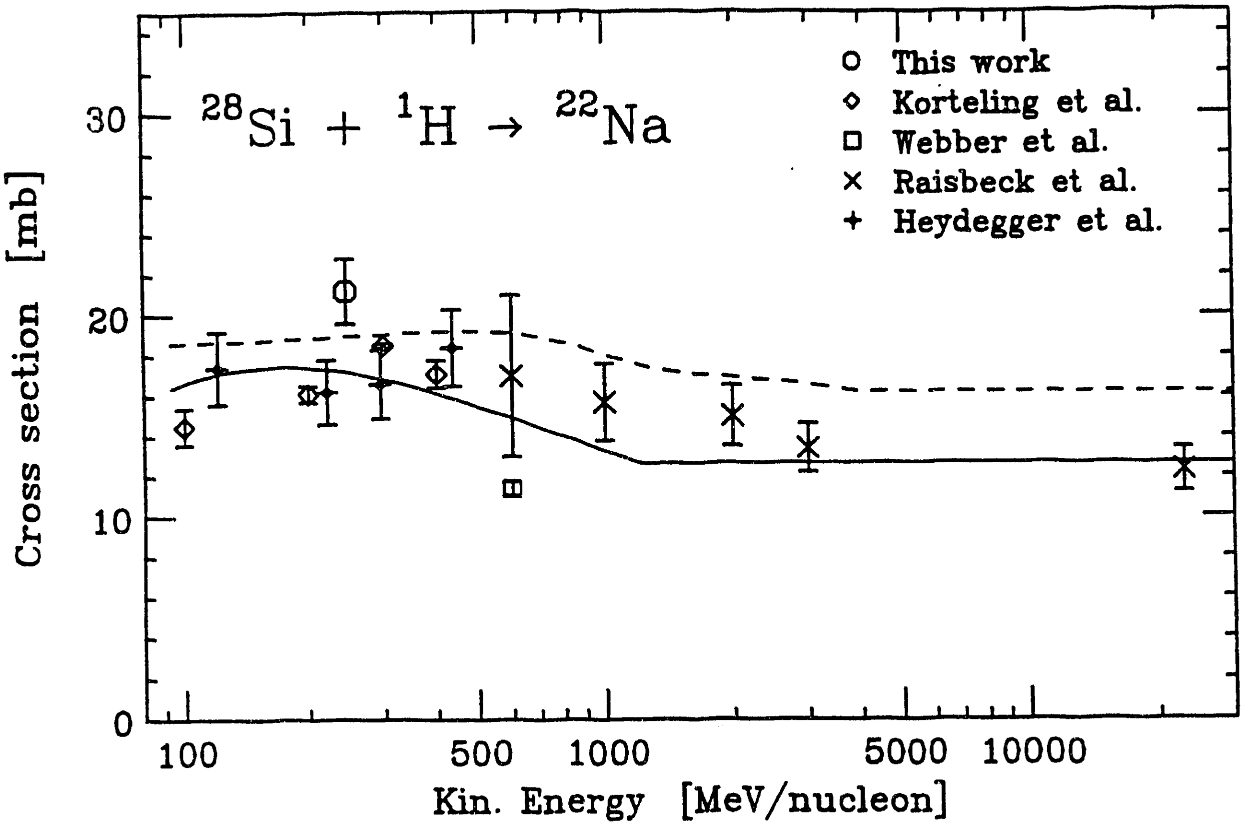

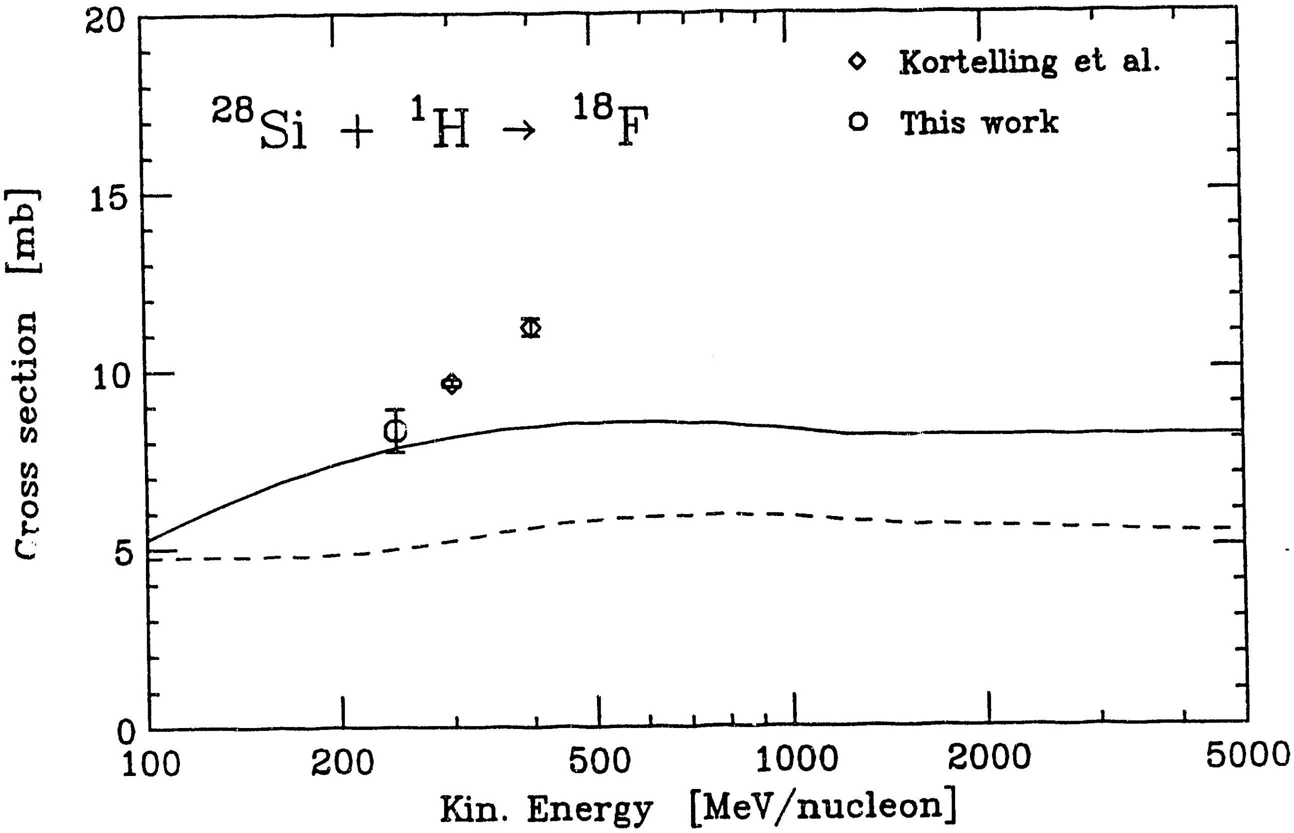

Figure 83. Comparison of results for the production of ^{18}Fe and ^{22}Na from ^{28}Si fragmentation with previous measurements and model predictions.

IV. LITERATURE CITED

1. Guerreau, D., 1985, Nucl. Phys., A447, 37c.
2. Lefort, M. and Ngo, C., 1978, Ann. Phys. (Paris), 3, 5.
3. Schroeder, W. U. and Huizenga, J. R., 1977, Ann. Rev. Nucl. Sci., 27, 465.
4. Heckman, H. H., Greiner, D. E., Lindstrom, P. J. and Bieser, F. S., 1972, Phys. Rev. Letters, 28, 926.
5. Bleszynski, M. and Sander, C., 1979, Nucl. Phys., A326, 525.
6. Friedman, W. A., 1983, Phys. Rev., C27, 569.
7. Goldhaber, A. S., 1974, Phys. Letters, 53B, 306.
8. Goldhaber, A. S. and Heckman, H. H., 1978, Ann. Rev. Nucl. Part. Sci., 28, 161.
9. Feshbach, H. and Zabek, M., 1977, Ann. Phys., 107, 110.
10. Engelage, J., Baumgartner, M., Greiner, D. E., Lindstrom, P. J., Olson, D. L., Wade, R., Crawford, H. J., and Webb, M. L., 1986, Phys. Lett., B173, 34.
11. Garcia-Munoz, M., Simpson, J. A., Guzik, T. G., Wefel, J. P. and Margolis, S. H., 1987, Astrophys. J. Suppl., 64, 269.
12. Greiner, D. E., 1972, Nucl. Instrum. Methods., 103, 291.
13. Lamport, J. E., Mason, G. M., Perkins, M. A. and Tuzzolino, A. J., 1976, Nucl. Instr. and Methods, 134, 71.
14. Kobayashi, T. et al., 1987, Nucl. Inst. and Methods, A254, 281
15. Nagamiya, S., 1981, Proc. 5th H. E. Heavy Ion Study, Berkeley, LBL-12652, p. 141.
16. Nagamiya, S., Randrup, J. and Symons, T.J.M., 1984, Ann. Rev. Nucl. Part. Sci., 34, 155.
17. Scott, D. K., 1981, Nucl. Phys., A354, 375c.
18. Scott, D. K., 1983, Nucl. Phys., A409, 291c.
19. Faessler, A., 1983, Nucl. Phys., A400, 565c.
20. Lindstrom, P. J., Greiner, D. E., Heckman, H. H., Cork, B. and Bieser, F. S., 1975, LBL Report #3650.
21. Olson, D. L., Berman, B. L., Greiner, D. E., Heckman, H. H., Lindstrom, P. J. and Crawford, H. J., 1983, Phys. Rev., C28, 1602.
22. Peng, J. C., DeVries, R. M. and DiGiacomo, N. J., 1981, Physics Letters, 98B, 224.

23. Greiner, D. E., Lindstrom, P. J., Heckman, H. H., Cork, B. and Bieser, F. S., 1975, Phys. Rev. Letters, 35, 152.

24. Mewaldt, R. A., 1989, in Cosmic Abundances of Matter, ed. C. J. Waddington, AIP Conf. Proc. 183, (New York, 1989, American Institute of Physics), p. 124.

25. Harvey, B. G., 1981, Phys. Rev. Lett., 47, 454.

26. Silberberg, R. and Tsao, C. H., 1973, Ap. J. Supplement, 25, 315.

27. Webber, W. R., Kish, J. C. and Schrier, D. A., 1989, Phys. Rev. C.

28. Letaw, J. R., Silberberg, R. and Tsao, C. H., 1983, Ap. J. Suppl., 51, 271.

29. Karol, P. J., 1975, Phys. Rev., C11, 1203.

30. Kirkby, P. and Link, W. T., 1966, Canadian J. Phys., 44, 1847.

31. Westfall, G. D. et al., 1979, Phys. Rev. C., 19, 1309.

32. Perrin, C., Kox, S., Longeguenue, N., Viano, J. B., Buenerd, M., Cherkaoui, R., Cole, A. J., Gamp, A., Menet, J., Ost, R., Bertholet, R., Guet, C. and Pinston, J., 1982, Phys. Rev. Letters, 49, 1905.

33. Cole, A. J., Rae, W.D.M., Brandan, M. E., Decal, A., Harvey, B.G., Legrain, R., Murphy, M. J. and Stokstad, R. G., 1981, Phys. Rev. Letters, 47, 1705.

34. Jaros, J., Wagner, A., Anderson, L., Chamberlain, O., Fuzesy, R. Z., Gallup, J., Gorn, W., Schroeder, L., Shannon, D., Shaprio, G. and Steiner, H., 1978, Phys. Rev., C18, 2273.

35. Heinrich, W., Brechtmann, G., Hirzebruch, S. E., Winkel, E. and Rusch, G., 1990, 21st ICR Conference Papers, (Australia, University of Adelaide), 3, 436.

36. Frazer, W. R., Ingber, L., Mehta, C. H., Poon, C. H., Silverman, D., Stowe, K., Ting, P. D. and Yesian, H. J., 1972, Rev. Mod. Phys., 44 284.

37. Cugnon, J. and Sartor, R., 1980, Phys. Rev., D21, 2342.

38. Hufner, J., Schafer, K. and Schurmann, B., 1975, Phys. Rev., C12, 1888.

39. Morrissey, D. J., Oliveira, L. F., Rasmussen, J. O., Seaborg, G. T., Yariv, Y. and Fraenkel, Z., 1979, Phys. Rev. Lett., 43, 1139.

40. Greiner, D. E., 1983, Nucl. Phys., A400, 325c.

41. Lynen, U., Bock, I., Muller, W. F. J., Goggi, A., Hildenbrand, K. D., Olmi, A., Sann, H., Selzer, H., Pelte, D., Winkler, V., Glasow, R., Kamport, K. H. and Santo, R., 1983, Nucl. Phys., A409, 385c.

42. Beatty, J. J., 1986, unpublished compilation.

43. Anderson, L., Bruckner, W., Moeller, E., Nagamiya, S., Nissen-Meyer, S., Schroeder, L., Shapiro, G., and Steiner, H., 1983, Phys. Rev., C28, 1224.

44. Bertsch. G., 1981, Phys. Rev. Lett., 46, 472.

45. Murphy, M. J., 1984, Phys. Lett., 135, 25.

46. Van Bibber, K., Hendrie, D. L., Scott, D. K., Weiman, H. H., Schroeder, L. S., Geaga, J. V., Cessin, S. A., Treuhaft, R., Grossiord, Y. J., Rasmussen, J. O. and Wong, C. Y., 1979, Phys. Rev. Letters, 43, 840.

47. Feshbach, H. and Huang, K., 1973, Phys. Lett., 47B, 300.

48. Viyogi, V. P., Symons, T.J.M., Doll, P., Greiner, D. E., Heckman, H. H., Hendrie, D. L., Lindstrom, P. J., Mahoney, J., Scott, D. K., Van Bibber, K., Westfall, G. D., Weiman, H., Crawford, H.J., McParland, C. and Gelbke, C. K., 1979, Phys. Rev. Letters, 42, 33.

49. Stokstad, R. G., 1984, Comm. Nucl. Part. Phys., 13, 231.

50. Wong, C. Y. and Van Bibber, K., 1982, Phys. Rev., C25, 2990.

51. Simpson, J. A., 1983, Ann. Rev. Nucl. Part. Sci., 33, 323.

52. Meyer, J. P., in Cosmic Abundances of Matter, ed. C. J. Waddington (New York, 1989, Amer. Inst. of Physics), p. 245.

53. Anders, E., and Ebihara, 1982, M., Geochim. Cosmochim. Acta, 46, 2362.

54. Wefel, J. P., 1991, in Cosmic Rays, Supernovae and the Interstellar Medium, eds. M. M. Shapiro, R. Silberberg and J. P. Wefel, NATO ASI Series C, Vol. 337, (Dordrecht, Kluwer), p. 29.

55. Binns, W. R., et al., 1989, Astrophys. J., 346, 997.

56. Garcia-Munoz, M., Simpson, J. A. and Wefel, J. P., 1979, Ap. J. Letters, 232, L95.

57. Woosley, S. E. and Weaver, T. A., 1981, Ap. J., 243, 561.

58. Prantzos, N., et al., 1984, Proc. 19th Int. Cosmic Ray Conf. (LaJolla), 3, 167.

59. Gibner, P. S., Mewaldt, R. A., Schindler, S. M. and Stone, E. C., 1992, Ap. J. Letters, 391, L89.

60. Garcia-Munoz, M., Pyle, K. R. and Simpson, J. A., 1992, Paper E.7-M presented at COSPAR, The World Space Congress, Washington, DC, September 1992.

61. Cowsik, R., Pal, Y., Tandon, S. N. and Verma, R. P., 1968, Canadian J. Phys., 46, 5646.

62. Gloeckler, G. and Jokipii, J. R., 1969, Phys. Rev. Letters, 22, 1448.

63. Garcia-Munoz, M., Mason, G. M., and Simpson, J. A., 1977, Ap. J., 217, 859.

64. Fichtel, C. E. and Reames, D. V., 1968, Phys. Rev., 175, 1564.

65. Cesarsky, C. J. and Ormes, J. F., 1987, Essays in Space Science, NASA Conf. #2464, p. 191.

66. Jones, F. C., 1979, Ap. J., 229, 747.

67. Parker, E. N., 1976, in The Structure and Content of the Galaxy and Galactic Gamma Rays, (NASA/GSFC Rept. No. X-662-76-154), p. 320.

68. Blandford, R. D. and Ostriker, J. P., 1980, Ap. J. 237, 793.

69. Beatty, J. J. et al., The SMILI Collaboration, 1993, Ap. J., in press.

70. Honda, M. and Lal, D., 1960, Phys. Rev., 118, 1618.

71. Reyss, J. L., Yokoyama, Y. and Guichard, F., 1981, Earth and Planet Sci. Letters, 53, 203.

72. Mahoney, W. A., Ling, J. C., Jacobson, A. S. and Lingenfelter, R., 1982, Ap. J., 262, 742.

73. Bradt, H. C. and Peters, B., 1950, Phys. Rev., 77, 54.

END

DATE FILMED

4 / 28 / 93